

# MASTER THESIS

Signal modelling and imaging of  
low field MRI



S H E R I N E B R A H M A



# Signal Modelling and Imaging for Low Field MRI

by

Sherine Brahma

to obtain the degree of Master of Science  
at the Delft University of Technology,  
to be defended publicly on Friday October 25, 2019 at 2:00 PM.

Student number: 4728564  
Project duration: January 9, 2019 – October 25, 2019  
Thesis committee: Dr. Ir. R. F. Remis, TU Delft, supervisor  
Dr. Ir. Martin van Gijzen, TU Delft  
Prof. Dr. A. G. Webb, LUMC  
Ir. Kirsten Koolstra, LUMC  
Ir. Merel de Leeuw den Bouter, TU Delft



# Abstract

MRI machines are devices that are used to non-invasively obtain images of the internal anatomy and physiological processes of the human body. It is safe to use as the patient is not exposed to any harmful radiation, and there are no known side effects. But such machines that are commercially available are very expensive. Due to this reason, it eludes access to a large portion of the population, particularly in developing countries. This thesis investigates an inexpensive MRI machine that is based on a rotating inhomogeneous magnetic field map. Unlike conventional scanners, because of the rotating field, the signal model of this device has to account for it. The objective of this work is to examine the aforementioned model, and also to implement Krylov subspace-based reconstruction algorithms available in the IRTools package.



# Acknowledgment

There are lots of people I want to acknowledge, but first, I would like to sincerely 'unacknowledge' that person at the info desk who misplaced my submitted graduation form and gave me a heart attack.

Foremost, I would like to extend my gratitude to my supervisor, Dr. Ir. Rob Remis. He was so easily accessible despite his busy schedule. Without him, I think I would have never been introduced to the works of Paul C Lauterbur and Gene H. Golub, whose books have left me profoundly fascinated. I got stuck a few times during the span of my thesis, and Rob supervised me to take a feasible path. The discussion sessions he organized with Kirsten and Merel were extremely helpful in shaping my work. I really appreciate the freedom I got under him.

Kristen and Merel, my other supervisors, were always readily available. When I began working on the codes, it was their code which I started with. I gradually began replacing snippets of it until it was my code. I strongly believe that it is due to their crucial feedbacks that this report is in a much better state than before. I received a number of helpful assistance from them.

I am also grateful to the other Low-field MRI group members, Martin, Tom, Danny, and Patrick. I really enjoyed the discussions as they were very informative. And not to forget the most important part- Thank you Delft Global Lunch.

A big shout-out to my band for helping me keep a balanced mind. Shout-out to all my friends in the office, and outside of the office, for all the precious nonsensical banter for, again, helping me keep a balanced mind.

I express my deep gratitude to my elder sister for being such a good sister. It was very nice of her and my-soon-to-be brother-in-law to occasionally invite me over to their place to spend time with them. They have a genuine concern about my well being, and they have got me through difficult times. I would also like to thank the rest of my family back at home for their support.

Most importantly, for me, I can never thank my father enough because of whom I would have never got this opportunity. I lost him less than a month before I started my thesis. He was an extremely talented surgeon, like his father, and I am sure he would have loved to be in my defense. He has a lion's share in the reason for my motivation and interest in this field. Like him, my mother is also very dear to me, and I am blessed to have her encouragement. I would like to dedicate this work to my father, Dr. Madhu Sudan Brahma, and my mother, Dr. Rupali Deori Brahma.

*Sherine Brahma  
Delft, October 2019*



# Contents

<b>Abstract</b>	<b>iii</b>
<b>Acknowledgment</b>	<b>v</b>
<b>List of Figures</b>	<b>xi</b>
<b>List of Tables</b>	<b>xiii</b>
<b>1 Introduction</b>	<b>1</b>
1.1 Medical Imaging . . . . .	1
1.2 Magnetic Resonance Imaging . . . . .	2
1.3 MRI System. . . . .	2
1.4 Signal Processing in MRI . . . . .	4
1.5 Purpose of the Thesis . . . . .	5
1.6 Organization of the Report. . . . .	5
<b>Part 1: Signal Modeling</b>	<b>7</b>
<b>2 MRI Fundamentals</b>	<b>9</b>
2.1 Nuclear Precession. . . . .	9
2.2 Bulk Magnetization . . . . .	12
2.3 RF Excitation . . . . .	13
2.4 Rotating Frame of Reference . . . . .	13
2.5 The Bloch Equation . . . . .	14
2.6 On-Resonance Excitation . . . . .	16
2.7 Free Precession and Relaxation. . . . .	17
2.8 Detection of Signal . . . . .	18
2.8.1 Detection Modeling. . . . .	18
2.8.2 Induced Voltage . . . . .	19
2.8.3 Reciprocity Theorem . . . . .	21
2.9 Signal Expression . . . . .	22
2.10 Free Induction Decay. . . . .	22
<b>3 Rotating MRI machine</b>	<b>25</b>
3.1 Imaging with Signal Model . . . . .	26
3.2 Linear Gradient Field Imaging . . . . .	27
3.3 Inhomogeneous field Imaging . . . . .	30
3.4 Previous Work . . . . .	32
3.5 This Work. . . . .	33
<b>4 Signal Model for rSEM</b>	<b>35</b>
4.1 Experimental Setup . . . . .	35
4.2 Coordinate System Considerations . . . . .	36
4.3 Reciprocity Theorem . . . . .	36
4.4 Solving the Bloch Equation . . . . .	36
4.5 Plugging into the signal expression . . . . .	37
4.6 Changing to non-rotated frame . . . . .	39
4.7 Expression for Signal Model . . . . .	40
4.8 K-space consideration . . . . .	41

<b>Part 2: Signal Reconstruction</b>	<b>43</b>
<b>5 Problem Description</b>	<b>45</b>
5.1 Problem Formulation . . . . .	45
5.2 Regularization . . . . .	45
5.3 Choosing the Regularization Parameter. . . . .	46
5.3.1 Discrepancy Principle . . . . .	47
5.3.2 Generalized cross validation . . . . .	47
5.4 Choosing the Regularization Matrix . . . . .	48
<b>6 Algorithms</b>	<b>49</b>
6.1 Iterative algorithms . . . . .	50
6.2 Geometric Interpretation of Krylov Subspace Methods. . . . .	50
6.2.1 Steepest Descent. . . . .	51
6.2.2 Conjugate Direction . . . . .	52
6.2.3 Krylov Subspace Connection . . . . .	52
6.3 Lanczos Tridiagonalization. . . . .	53
6.4 Arnoldi's method . . . . .	54
6.5 Golub-Kahan Bidiagonalization . . . . .	54
6.6 IR Tools . . . . .	54
6.7 IRhybrid_Isqr . . . . .	55
6.7.1 Discrepancy Principle in IRhybrid_Isqr . . . . .	55
6.7.2 IRhybrid_Isqr Algorithm . . . . .	56
6.8 IRhtv . . . . .	56
6.9 Regularization matrix handling. . . . .	57
6.9.1 IRhybrid_Isqr . . . . .	57
6.9.2 IRhtv . . . . .	57
<b>Part 3: Results and Analysis</b>	<b>59</b>
<b>7 Simulations</b>	<b>61</b>
7.1 Time Domain Data Size and Dwell Time Investigation . . . . .	62
7.1.1 Varying TD with Fixed DW . . . . .	65
7.1.2 Varying DW with Fixed TD . . . . .	67
7.2 Parameter Selection Strategy Investigation. . . . .	70
7.2.1 Discrepancy Principle . . . . .	70
7.2.1.1 Visual Inspection . . . . .	71
7.2.1.2 Computation Time . . . . .	73
7.2.1.3 Relative Residual Norm Versus Number of Iterations . . . . .	73
7.2.1.4 Relative Error Norm Versus Number of Iterations. . . . .	75
7.2.1.5 Regularization Parameter Versus Number of Iterations . . . . .	76
7.2.2 General Cross Validation. . . . .	77
7.2.2.1 Visual Inspection . . . . .	78
7.2.2.2 Computation Time . . . . .	79
7.2.2.3 Relative Error Norm Versus Number of Iterations. . . . .	79
7.2.2.4 GCV Values Versus Number of Iterations . . . . .	81
7.2.2.5 Regularization Parameter Versus Number of Iterations . . . . .	81
7.3 Signal Model for Rotating MRI Investigation . . . . .	82
7.3.1 Influence of Angle noise and Flip Angles . . . . .	84
7.3.1.1 Relative Error Norm Versus Number of Iterations. . . . .	86
7.3.2 Influence of Wrong Flip Angles . . . . .	87
7.3.2.1 Visual Inspection . . . . .	87
7.3.2.2 Relative Error Norm Versus Number of Iterations. . . . .	88
7.4 Angle Combination Investigation . . . . .	90

---

<b>8</b>	<b>Conclusions and Future Work</b>	<b>97</b>
8.1	Conclusion . . . . .	97
8.2	Future Work. . . . .	98
8.2.1	K-space and Spatial Domain Link . . . . .	98
8.2.2	Receive Field Profile Investigation. . . . .	98
8.2.3	Optimal Angle Combination Selection . . . . .	98
8.2.4	Experimental Work . . . . .	99
	<b>Bibliography</b>	<b>101</b>



# List of Figures

1.1 Tomographic Slices . . . . .	1
1.2 MRI without Gradient System . . . . .	3
1.3 MRI with Gradient System . . . . .	3
1.4 Forward Problem . . . . .	4
1.5 Inverse Problem . . . . .	5
2.1 Spins in Human Body . . . . .	10
2.2 Spin Orientations . . . . .	11
2.3 Cancelling of Transverse Magnetization Components . . . . .	12
2.4 Rotating Frame of Reference . . . . .	13
2.5 Trajectory of Excited Magnetization . . . . .	17
2.6 Relaxation Magnetization Curves . . . . .	18
2.7 Relaxation Magnetization Trajectory . . . . .	18
2.8 Detector Modeling . . . . .	19
2.9 Induced Magnetic Moment . . . . .	19
2.10 Reciprocity Theorem . . . . .	21
2.11 FID Decay Curve . . . . .	24
3.1 Low Field MRI Prototypes . . . . .	25
3.2 Image Discretization . . . . .	26
3.3 Homogeneous Magnetic Field and Shepp Logan Phantom . . . . .	28
3.4 Gradient Field . . . . .	29
3.5 Components of MRI System . . . . .	30
3.6 Inhomogeneous Magnetic Field . . . . .	31
3.7 Stacking Encoding Matrices . . . . .	32
4.1 Prototype of the Rotating MRI machine . . . . .	35
4.2 Schematic of Rotating MRI Machine . . . . .	36
4.3 Measured B0 Profile . . . . .	41
4.4 K-space Trajectories . . . . .	42
5.1 L-curve . . . . .	46
5.2 General Cross Validation . . . . .	47
6.1 Measurement and Reconstruction . . . . .	49
6.2 Problem Illustration . . . . .	51
6.3 Steepest Descent . . . . .	51
6.4 Conjugate Direction Method . . . . .	52
6.5 Important Search Directions . . . . .	53
7.1 Interpolated B0 Map . . . . .	62
7.2 K-space and Spatial Domain Relationship . . . . .	63
7.3 Aliasing Artifact . . . . .	63
7.4 Ground Truth Image . . . . .	65
7.5 Relative Error Norm for Fixed DW . . . . .	66
7.6 Reconstructed Images for Fixed DW . . . . .	67
7.7 Relative Error Norm for Fixed TD . . . . .	68
7.8 Reconstructed Images for Fixed TD . . . . .	69
7.9 Simulated Measured Signal . . . . .	70
7.10 Reconstructed Images for Investigating Discrepancy Principle for IRhybrid_lsqr . . . . .	72

7.11 Reconstructed Images for Investigating Discrepancy Principle for IRhtv . . . . .	73
7.12 Relative Residual Norm for Investigating Discrepancy Principle . . . . .	74
7.13 Relative Error Norm for Investigating Discrepancy Principle . . . . .	76
7.14 Regularization Parameter for Investigating Discrepancy Principle . . . . .	77
7.15 Reconstructed Image for Investigating GCV . . . . .	78
7.16 Reconstructed image using WGCV with different weights, w, using IRhtv. . . . .	79
7.17 Relative Error Norm for Investigating GCV . . . . .	80
7.18 GCV Values for Investigating GCV . . . . .	81
7.19 Regularization Parameter for Investigating GCV . . . . .	82
7.20 Angle Noise Distribution . . . . .	84
7.21 Comparing Angle Noise Histograms . . . . .	85
7.22 Relative Error Norm for Investigating Signal Model . . . . .	87
7.23 Reconstructed Images for Investigating Wrong Flip Angle . . . . .	88
7.24 Relative Error Norm for Investigating Wrong Flip Angle . . . . .	89
7.25 Encoding Matrices for Rotated Field Map . . . . .	90
7.26 Symmetric and Unsymmetric Reconstruction . . . . .	91
7.27 Independent Columns . . . . .	91
7.28 Gram Matrix and Concatenated Gram Matrix . . . . .	92
7.29 Average Angle . . . . .	93
7.30 Relative Error Norm for Investigation of Angle Combinations . . . . .	94
7.31 Relative Error Norm for Investigation of Number Angles Chosen . . . . .	96
8.1 Expressing Gram Matrix Elements . . . . .	98
8.2 Gram Matrix without using $\mathbf{A}_{\theta_2}$ . . . . .	99

# List of Tables

2.1	Properties of some NMR-Active Nuclei [14]	10
7.1	TD and DW investigation parameters	64
7.2	Relative error norm for fixed DW	66
7.3	Relative Error Norm for Fixed TD	69
7.4	Discrepancy principle investigation parameters	70
7.5	Total Computation Time using Discrepancy Principle	73
7.6	Relative Residual Norm for investigation of Dcrepancy Principle	75
7.7	Relative Error Norm for investigation of Dcrepancy Principle	76
7.8	GCV investigation parameters	77
7.9	Total Computation Time using Discrepancy Principle	79
7.10	Relative Error Norm for the investigation of Dcrepancy Principle	81
7.11	Signal model investigation parameters	85
7.12	Relative Error Norm for investigation of signal model	87
7.13	Relative Error Norm for investigation wrong Flip Angle	90



# Introduction

Understanding and solving complicated problems in medicine requires the joint effort of professionals from diverse backgrounds such as doctors, biologists, chemists, physicists, mathematicians, engineers and experts from other disciplines. A considerable portion of such problems pertains to diagnostic purposes. Their main objective is to correctly identify the patient's disease on time so that appropriate actions can be taken swiftly. Imaging constitutes a core element of it that helps doctors to visualize the issues to make proper decisions. Although this work is about Magnetic Resonance Imaging (MRI) technique, popular imaging techniques in use are described briefly in the beginning. It is then followed by a small elaboration on the Magnetic Resonance Imaging (MRI) technique to state its importance. This chapter concludes by outlining the purpose of this thesis and then explaining the structure of this report.

## 1.1. Medical Imaging

Medical imaging is the way of acquiring anatomical or functional information about the body's interior parts. Anatomical information describes the structures of the body parts (e.g. position of the bones, the rupture in a certain organ), whereas the functional information gives us an idea about the functions and relationships of the body parts (e.g. blood flow speed, regional chemical composition). Imaging that is done by sectioning the body, by using some penetrating wave, without actually cutting it open, is called tomography.

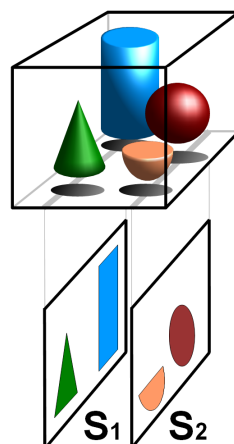


Figure 1.1: The figure shows the basic principles of tomography.  $S_1$  and  $S_2$  are different tomographic slices of the objects which have to be imaged. Picture is adapted from <https://en.wikipedia.org/wiki/Tomography>

Some popular tomographic modalities with small descriptions are discussed below-

- **Computed tomography:** Computed Tomography (CT) is a modality that uses x-rays to image a body from different angles. These are then combined to form a cross-sectional view of it.
- **Single-photon emission computed tomography:** Single-photon emission computed tomography (SPECT) is a tomography used in nuclear medicine. In nuclear medicine, the patients receive radioactive compounds, called radiotracers, either by injection, inhalation or by ingestion. These substances emit gamma rays from the interior of the body, which are then detected by gamma cameras of the SPECT scanner. This is used to form image slices of the human body.
- **Positron emission tomography:** Positron emission tomography (PET) is also used in nuclear medicine for imaging. The main difference of it from SPECT lies in the underlying physics of how the gamma rays are formed, which is based on the kind of radiotracers administered to the patients. PET exploits this specific process of gamma-ray formation and uses it to make images.
- **Magnetic Resonance Imaging:** Magnetic resonance imaging (MRI) is based on the Nuclear magnetic resonance (NMR) phenomenon. It is a complex physical process that will be described more in the following sections and subsequent chapters. Briefly, MRI is a tomographic technique that uses magnetic fields to image the subject by measuring the nuclear magnetic resonance (NMR) signals emitted by the body.

## 1.2. Magnetic Resonance Imaging

MRI is a tomographic imaging method that can produce anatomical as well as functional images of the patient. There are several advantages of the MRI technique, which are listed below. These descriptions are based on [14].

- **No ionizing radiations involved:** Unlike CT, SPECT, and PET, MRI is not associated with any potentially harmful radiations. It works in the radio-frequency range, and there are no known side effects. Thus, it is safe to use.
- **More freedom in choosing tomographic slice orientations:** In CT, PET or SPECT, the orientation of the image slices depends on the direction of the scanner's detector with respect to the patient. Whereas in MRI, the orientation of the tomographic slices depends solely on the way that the external magnetic fields are applied. Thus, complex orientations of the slices can be obtained, and no mechanical adjustments of the detectors are required.
- **Information rich NMR signals:** NMR signals are dependent on many factors like nuclear spin density, spin-lattice relaxation time, spin-spin relaxation time, chemical-shift differences, and so on. It is possible to study the effect of just one specific factor by suppressing the influences of other factors. In this way, the same signal can be used to study many different properties. Thus, NMR signals are rich in information.

To delve deeper into MRI, it is beneficial to have a basic idea of the MRI machine itself, which is discussed next.

## 1.3. MRI System

For now, we are going to look at the MRI system from a high-level view. Note that the image acquisition process with MRI is a complex technique. There are different ways of obtaining different MRI images, that give different information. Many details are left out in the following description.

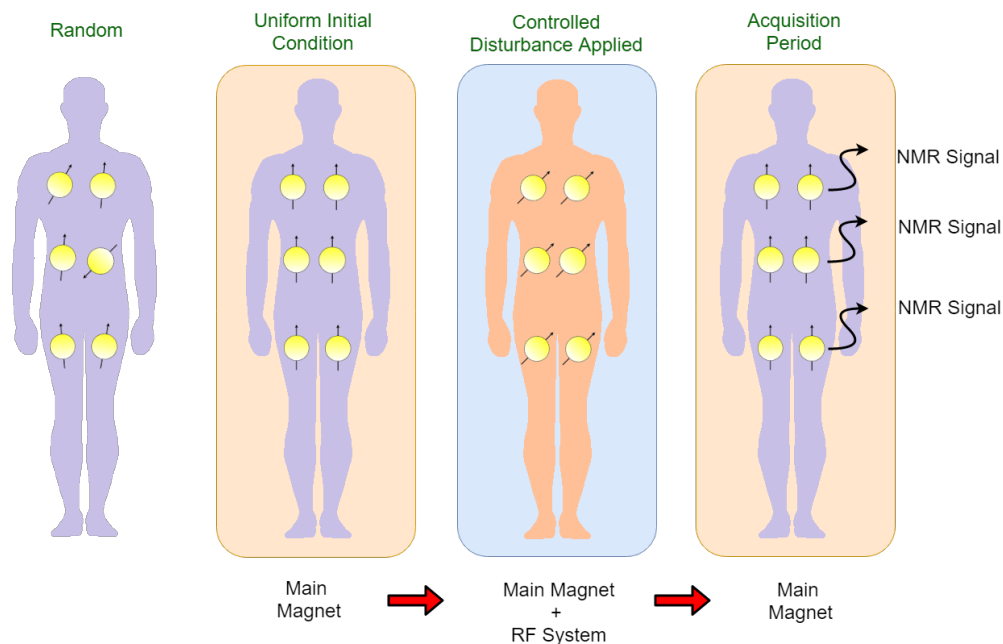


Figure 1.2: Basic MRI technique without the gradient system. The circles represent the nuclei present in the body.

Figure 1.2 and figure 1.3 are general illustrations of the basic principle of MRI imaging. In figure 1.2, a uniform initial condition is first created for the nuclei in the body of the patient. These nuclei are responsible for emitting the NMR signals. After creating this initial environment, controlled 'disturbances', in the form of pulses, are applied so that the spins are perturbed from the initial condition<sup>1</sup>. When these disturbances are removed, the nuclei lose energy in the form of NMR signals and return to the initial condition.

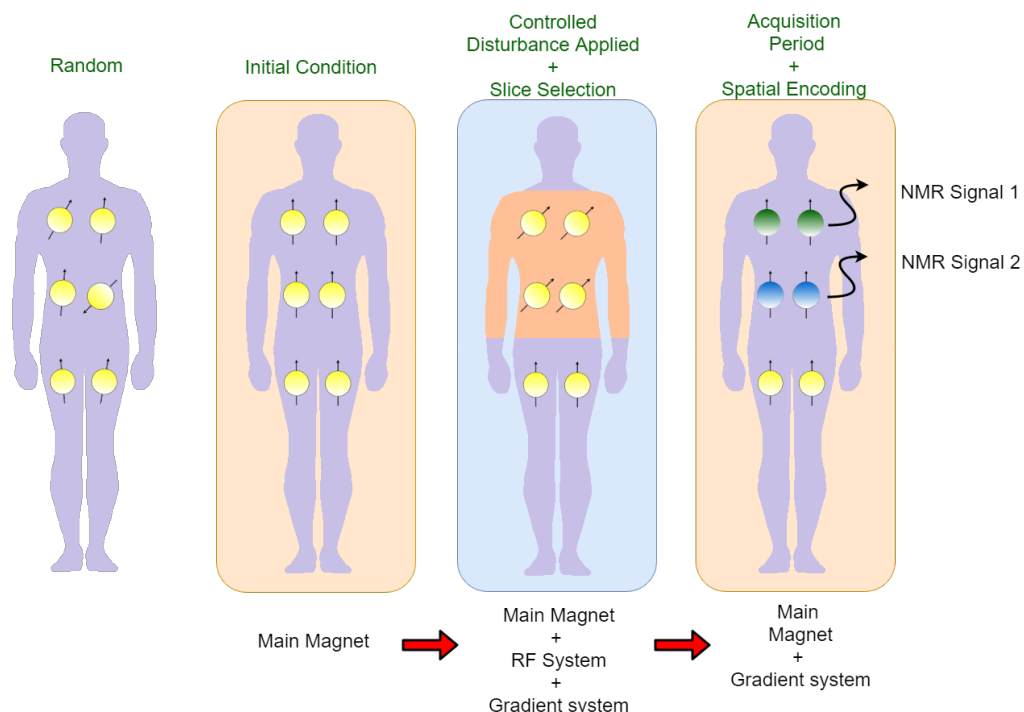


Figure 1.3: Basic MRI technique with the gradient system. The circles represent the nuclei present in the body.

<sup>1</sup>In MRI literature, the term 'disturbance' is not used. The reason it is used here is to mean that the initial condition is disturbed. The technical terms will be discussed in the later chapters.

Now, in (figure 1.2), all nuclei throughout the body experienced the same disturbances. When these are removed, the nuclei at different locations lose their energy in the same way. Due to this, they emit the same NMR signal and where they are coming from, for example, the chest, abdomen or thigh, cannot be identified. We are interested in finding out the position of nuclei that are emitting the NMR signals. This forms the basis of MRI imaging and the process of finding out the locations is called spatial localization.

Figure 1.3 describes a way how spatial localization can be achieved. Here, controlled disturbances are selectively applied to those nuclei which belong to a chosen slice (highlighted in orange) of the body. When these are removed, it is possible to make the nuclei at different locations, within that slice, to lose energy at different rates. As a result, different nuclei emit different signals. This means that we are essentially encoding spatial information in the nuclei at different locations. This principle is used to image a body based on the NMR signals that are received.

The whole MRI system can be decomposed into three main sub-components- main magnet, gradient system, and radio frequency (RF) system. These are described more below. As the last section (section 1.2), this part is also based on [14].

1. **The main magnet:** The function of the main magnet is to generate a strong static magnetic field which is also called the background field. In principle, this field evenly polarizes the nuclear spins<sup>2</sup> and creates a uniform initial condition. This field should be as homogeneous as possible so that the spins are uniformly polarized. Also, it is observed that the signal-to-noise ratio (SNR) of an NMR signal increases as the strength of the main magnet increases. So a stronger main magnet is beneficial in this respect.
2. **The gradient system:** Gradient systems consist of coils which are constructed to produce spatially non-uniform magnetic fields. This component is essential for slice selection and spatial encoding.
3. **The RF system:** The RF system is the component that is responsible for applying the controlled 'disturbances' in the form of pulses. It consists of a transmitter coil that is used to generate magnetic pulses to excite the spins of the object. It also consists of a receiver coil that receives the NMR signal when the pulses are removed.

After obtaining the NMR signal, it is required to perform signal processing techniques on it before an image, that has some practical significance, is obtained. A brief overview of the signal processing aspects is given next.

## 1.4. Signal Processing in MRI

Signal processing in MRI aims to solve two problems. They are described below-

- **Forward Problem:** In the forward problem, we assume that we know the input and the model of the system, and based on it, we try to predict the output. In our case, the input is the applied magnetic fields, and the system model will be derived in a later chapter. Using this input and model, we try to obtain the measured signal (figure 1.4).

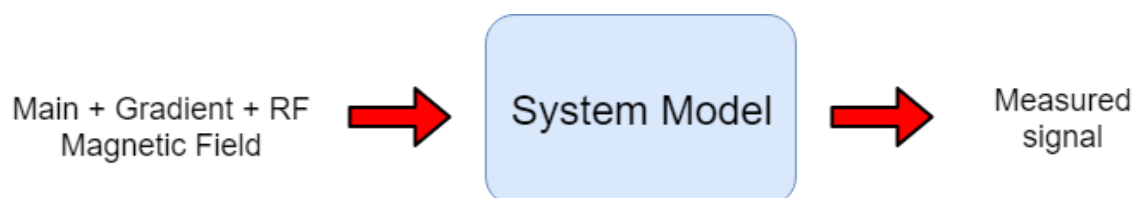


Figure 1.4: Forward Problem.

<sup>2</sup>Only nuclei with odd atomic weights and/or odd atomic numbers are involved in generating NMR signals. These nuclei are called spins[14].

- **Inverse Problem:** In the inverse problem, we assume that we know the measured signal and the model of the system (figure 1.5). We then try to predict the image that is giving this measured signal using appropriate reconstruction algorithms. In this work, we will investigate reconstruction algorithms based on Krylov subspace.

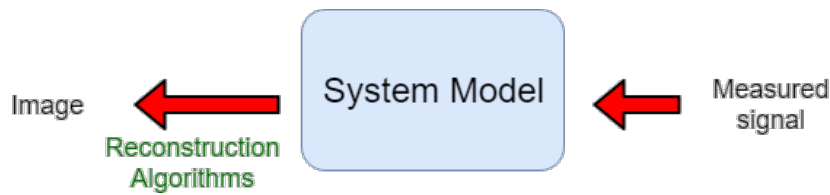


Figure 1.5: Inverse Problem.

Until this point, a basic overview of the MRI technique is given without going too much into the details. This small background in MRI is believed to be sufficient for getting some idea about the purpose of the thesis, which is briefly discussed next.

## 1.5. Purpose of the Thesis

This thesis focuses on the signal processing aspects (the forward and the inverse problem) of an unconventional MRI device, operating in a low magnetic field setting. This device uses an inhomogeneous background field which is also used for spatial encoding. This is unlike conventional MRI machines, which have been discussed so far in this chapter, that use a separate gradient system for spatial encoding with a homogeneous background field. The device used in this thesis is cheaper, less bulky and less complex. This purpose will be further elaborated in chapter 4.

## 1.6. Organization of the Report

This report is divided into three parts-

### 1. Part 1: Signal Modeling

This part is concerned with deriving the signal model of the unconventional MRI device. It also throws light on the purpose of the thesis.

### 2. Part 2: Signal Reconstruction

This part describes the algorithms that are employed to compute the MRI image using the signal model derived in Part 1.

### 3. Part 3: Results and Analysis

In this part, several investigations are done on the performance of the algorithms introduced in Part 2 to reconstruct the images using the signal model derived in Part 1. It ends by concluding the results of this work, and suggesting for possible future work.



# Part 1: Signal Modeling



# 2

## MRI Fundamentals

In this chapter, we will look at the MRI in a more detailed fashion. The motive of this part is to explain the basic mathematical equations that are involved in it. This will make it easy later to relate the MRI scanners in use with the unconventional MRI machine- like how it is different, and what advantages it can provide.

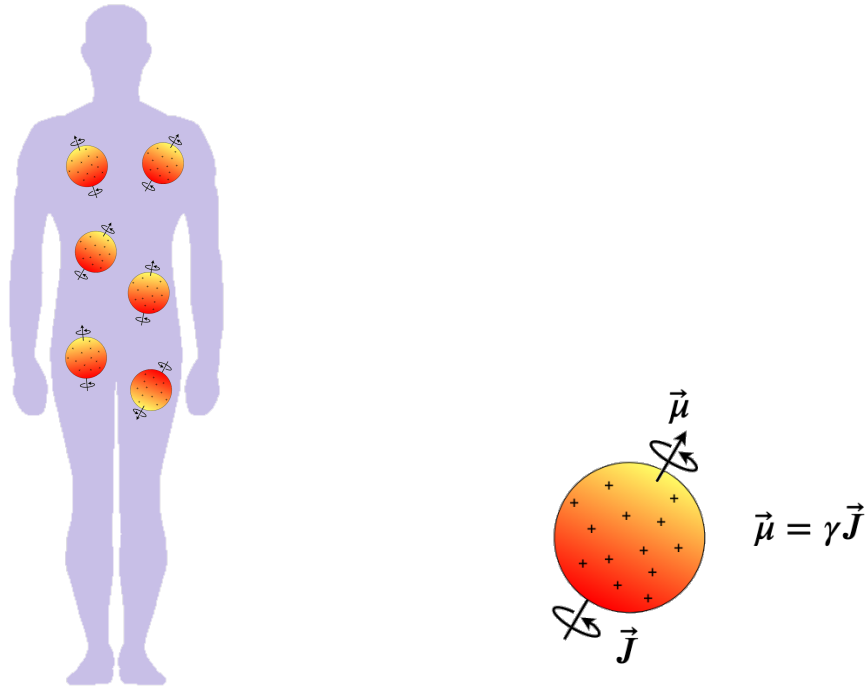
This chapter starts by touching upon some concepts of physics that lead to the magnetic resonance phenomenon, and progressively works towards the development of the Bloch Equation. Bloch Equations are the set of equations that are used to describe the motion of nuclear magnetizations. This equation stays true whatever construction of the machine is used. The Reciprocity theorem is applied to express this magnetization as a voltage signal that can be measured. Towards the end, a basic form of MRI signal, called "Free Induction Decay" (FID), is explained that this work is using.

This chapter outlines the description given in the book "Principles of Magnetic Resonance Imaging" by Zhi-Pei Liang and Paul C. Lauterbur [14], and more insight can be gained by referring to it.

### 2.1. Nuclear Precession

The objective of a clinical MRI machine is to image patients. It is common knowledge that humans, or any other matter, can be successively broken down into more fundamental particles like molecules, then to atoms, and then to the nucleus (figure 2.1a). MRI is a nuclear phenomenon that originates from nuclei spinning about their axis, called spins.

Although nuclear spin is a quantum mechanical property, in classical mechanics, it can be thought of as the nucleus physically rotating with angular momentum,  $\vec{J}$ . The nucleus consists of positive charges, and as the nucleus rotates about its axis, it gives rise to a magnetic field. This field is represented by a vector quantity called magnetic moment,  $\vec{\mu}$  (figure 2.1b).



(a)

(b)

Figure 2.1: a) The Human body is composed of nuclei b) A nucleus, with positive charges on it, rotating counterclockwise with angular momentum  $\vec{J}$ . As a consequence, it creates a magnetic moment  $\vec{\mu}$

A fundamental equation of particle physics relates the magnetic moment of the spin to the angular momentum as-

$$\vec{\mu} = \gamma \vec{J} \quad (2.1)$$

where  $\gamma$  is a constant called the gyromagnetic ratio. The value of the gyromagnetic ratio is intrinsic to the nucleus being considered. Some values are shown in table 2.1. It can be seen that  $^1H$  has the largest gyromagnetic ratio and consequently it has largest magnetization,  $\vec{\mu}$ , for a given angular momentum,  $\vec{J}$  (evident from equation 2.1). As the magnitude of the MRI signal is proportional to the magnitude of magnetization, which we will see, we will get a higher signal in the case of  $^1H$ . We can also observe from table 2.1 that sensitivity of it is large. Moreover, because  $^1H$  are present in abundance in the body, in the form of water or other organic compounds, they are a good candidate for being imaged by MRI.

Table 2.1: Properties of some NMR-Active Nuclei [14]

Nucleus	Gyromagnetic ratio (MHz/T), $\gamma = \frac{\gamma}{2\pi}$	Relative Sensitivity <sup>a</sup>
$^1H$	42.58	1.000
$^{13}C$	10.71	0.016
$^{19}F$	40.05	0.870
$^{31}P$	11.26	0.093

<sup>a</sup>Relative Sensitivity is calculated at a constant field for an equal number of nuclei

Suppose,  $\vec{i}$ ,  $\vec{j}$  and  $\vec{k}$  are the unit vectors along the  $x$ ,  $y$  and  $z$  axis respectively in the laboratory frame. If a strong magnetic field,  $B_0$ , is applied to a  $^1H$  spin along the  $z$ -direction

such that-

$$\vec{B}_0 = B_0 \vec{k}, \quad (2.2)$$

it turns out, through quantum mechanics, the  $^1H$  spin can assume two possible orientations. Either it orients itself making an angle  $\theta = +54^\circ 44'$  with the direction of  $B_0$  (called parallel spin) or an angle  $\theta = -54^\circ 44'$  (called anti-parallel spin) with it.

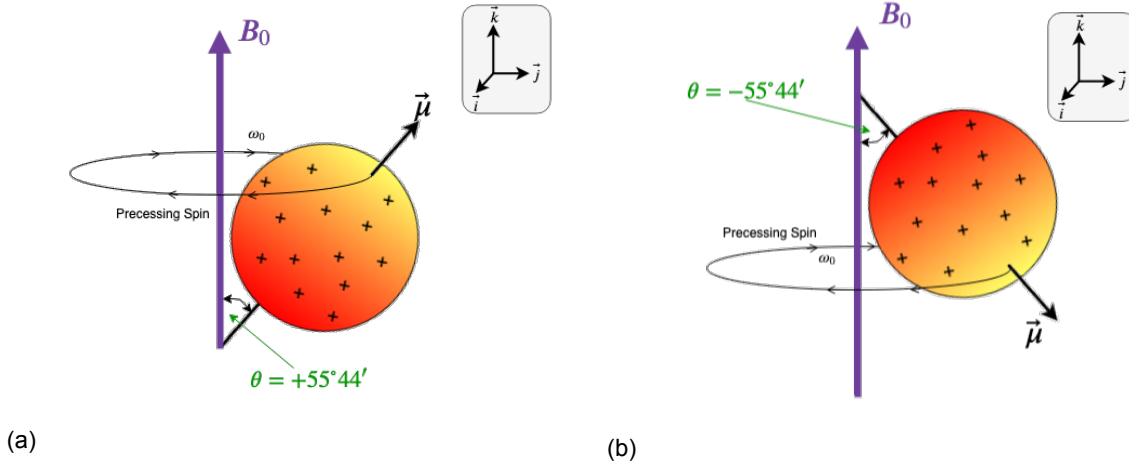


Figure 2.2: After external magnetic field,  $B_0$ , is applied the  $^1H$  spin orients itself either making an angle a)  $\theta = +54^\circ 44'$  with the direction of  $B_0$ , or b)  $\theta = -54^\circ 44'$  with the direction of  $B_0$

Instead of rotating about its axis, as shown in figure 2.1, the magnetic moments actually move in a precessing motion, as shown in figure 2.2. The angular speed,  $\omega_0$ , with which it precesses, can be found out by a classical treatment of the spin. In classical mechanics, we know that the torque,  $\vec{\tau}$ , is given by the cross product  $\vec{\mu} \times B_0 \vec{k}$ . Also, the same torque is equal to the rate of change of angular momentum,  $\frac{d\vec{J}}{dt}$ . Thus we have-

$$\begin{aligned} \vec{\tau} &= \vec{\mu} \times B_0 \vec{k} \\ \Rightarrow \frac{d\vec{J}}{dt} &= \vec{\mu} \times B_0 \vec{k} \\ \Rightarrow \frac{d\vec{\mu}}{dt} &= \gamma \vec{\mu} \times B_0 \vec{k} \quad (\text{Using Equation 2.1}) \end{aligned} \quad (2.3)$$

We can arrange  $\vec{\mu} = \mu_x \vec{i} + \mu_y \vec{j} + \mu_z \vec{k}$  into a transverse component,  $\vec{\mu}_{xy} = \mu_x \vec{i} + \mu_y \vec{j}$ , and a longitudinal component,  $\vec{\mu}_z = \mu_z \vec{k}$ , such that-

$$\vec{\mu} = \vec{\mu}_{xy} + \vec{\mu}_z \quad (2.4)$$

Solving equation 2.3, we obtain the following solution-

$$\begin{aligned} \mu_{xy}(t) &= \mu_{xy}(0) e^{-i\gamma B_0 t} \\ \mu_z(t) &= \mu_z(0) \end{aligned} \quad (2.5)$$

It is evident that the transverse component,  $\mu_{xy}(t)$ , due to the  $e^{-i\gamma B_0 t}$  term, is rotating in the transverse plane. The angular frequency with which it is rotating is given by-

$$\omega_0 = \gamma B_0 \quad (2.6)$$

This angular frequency,  $\omega_0$ , is known as Larmor frequency. It can be expressed as a vector quantity (Equation 2.7). We note that due to the negative sign, the spin precesses in a clockwise direction.

$$\vec{\omega}_0 = -\gamma \vec{B}_0 = -\omega_0 \vec{k} \quad (2.7)$$

## 2.2. Bulk Magnetization

So far, the discussion of precession was limited to the individual spins. We are more interested in the collective behavior of such spins in bulk. Thus, this leads us to formalize bulk magnetization,  $\vec{M}$ , which can be expressed as a collection of individual magnetic moments of individual spins,  $\vec{\mu}$ .

$$\vec{M} = \sum_{n=1}^{N_S} \vec{\mu}_n \quad (2.8)$$

where  $N_S$  is the total number of spins.

We have already seen that a  $^1H$  spin can take one of the two possible orientations. According to the theory of quantum mechanics, it is observed that there is an excess of parallel spins compared to anti-parallel spins by a very small fraction. Turns out, this small fraction of excess parallel nuclei is enough to bring about a collective noticeable magnetization in the direction of the external magnetic field,  $B_0$ , (figure 2.3a).

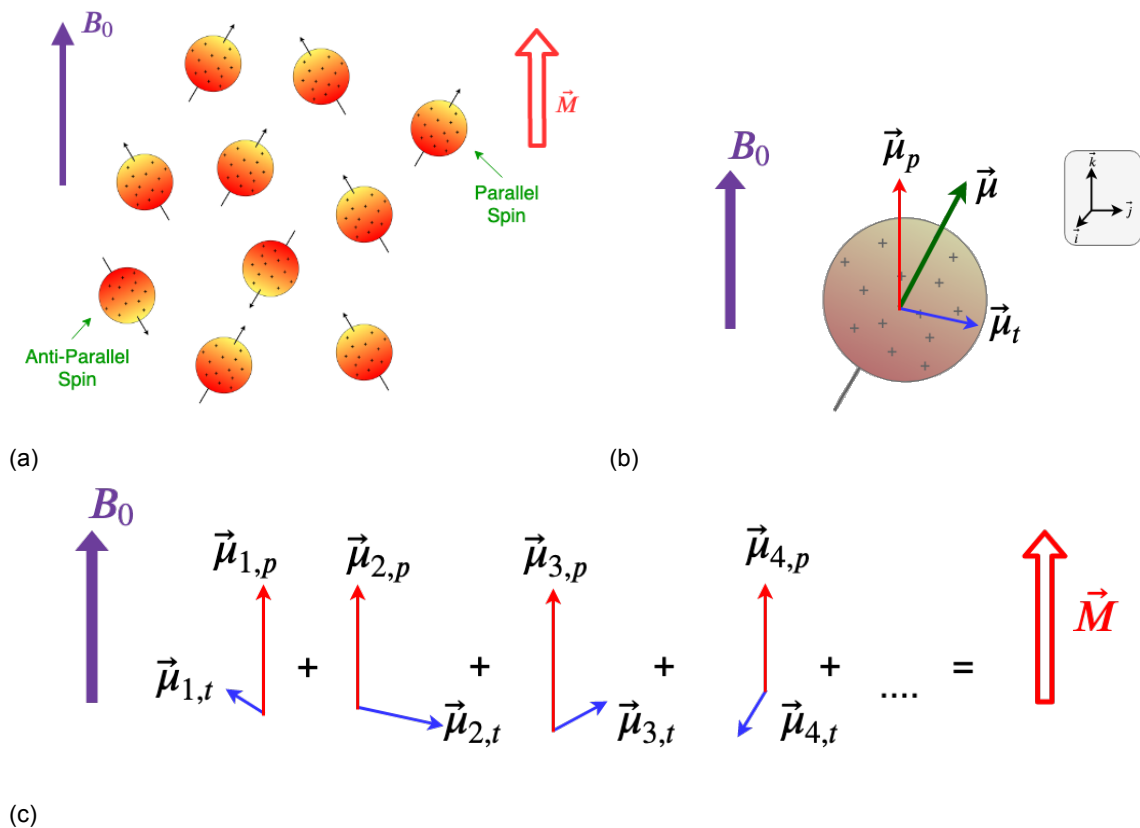


Figure 2.3: a) There is an excess of parallel spin compared to anti-parallel spins. The resultant bulk magnetization,  $\vec{M}$ , points along the direction of the external magnetic field,  $B_0$ . b) The magnetic moments of the parallel spins that are contributing to the net magnetization can be decomposed into two components.  $\vec{\mu}_p$  is the parallel component and  $\vec{\mu}_t$  is the transverse component with respect to  $B_0$ . c) Collectively, the transverse components cancel out.

The magnetic moments of the parallel spins, that are contributing to the net magnetization, can be decomposed into two components- one parallel to  $B_0$  and the other transverse to it (figure 2.3b). The transverse component of the parallel spins perpendicular to the external magnetic field is spread over randomly (figure 2.3c). Subsequently, they cancel each other out. However, all the parallel components point along the direction of the field. As a result, this bulk magnetization points exactly along the external magnetic field.

Its magnitude in equilibrium,  $|\vec{M}_{eq}|$ , is found out to be-

$$|\vec{\mathbf{M}}_{eq}| = \frac{\gamma^2 \hbar^2 B_0 N_S}{4KT_S} \quad (2.9)$$

Where  $\hbar$  is Planck constant,  $h$ , over  $2\pi$ , i.e.  $\hbar = \frac{h}{2\pi}$ .  $K$  is the Boltzmann constant, and  $T_S$  is the temperature of the spin system.

For the choice of our coordinates, if  $\vec{\mathbf{M}}^0 \triangleq M_x^0 \vec{\mathbf{i}} + M_y^0 \vec{\mathbf{j}} + M_z^0 \vec{\mathbf{k}}$  denotes the magnetization at  $t = 0$ , then

$$M_x^0 = 0, \quad M_y^0 = 0, \quad \text{and} \quad M_z^0 = |\vec{\mathbf{M}}_{eq}| \quad (2.10)$$

## 2.3. RF Excitation

In the previous section, we have seen that the perpendicular (transverse) component of the spins cancels each other out, and we have no net bulk magnetization towards the transverse direction. Now, it is possible to create a transverse component of bulk magnetization if we were able to bring about a phase coherence among the spins. When these spins reach a phase coherence, they are said to be in resonance.

In quantum mechanics, such a spin system can be brought to resonance if electromagnetic radiation of frequency,  $\omega_{rf}$ , is used to supply it with energy-

$$\Delta E = \hbar \omega_{rf} = \hbar \omega_0 \quad (2.11)$$

That means for a resonance to occur, the frequency of the electromagnetic radiation,  $\omega_{rf}$ , needs to be equal to the Larmor frequency,  $\omega_0$ .

$$\omega_{rf} = \omega_0 \quad (\text{Resonance condition}) \quad (2.12)$$

In a magnetic system, this energy comes from an external magnetic field,  $B_1$ , which is applied perpendicular to  $B_0$ . We have the following notation for it-

$$\vec{\mathbf{B}}_1(t) = B_1^e(t) \cos(\omega_{rf}t + \varphi) \vec{\mathbf{i}} - B_1^e(t) \sin(\omega_{rf}t + \varphi) \vec{\mathbf{j}} \quad (2.13)$$

where  $B_1^e(t)$  is the envelope function of the pulse,  $\omega_{rf}$  is the excitation frequency and  $\varphi$  is the initial phase angle. In complex notation it can be expressed as-

$$B_1(t) = B_1^e(t) \cos(\omega_{rf}t + \varphi) - i B_1^e(t) \sin(\omega_{rf}t + \varphi) = B_1^e(t) e^{-i(\omega_{rf}t + \varphi)} \quad (2.14)$$

We shall consider  $\varphi = 0$  henceforth to make the mathematics easier.

## 2.4. Rotating Frame of Reference

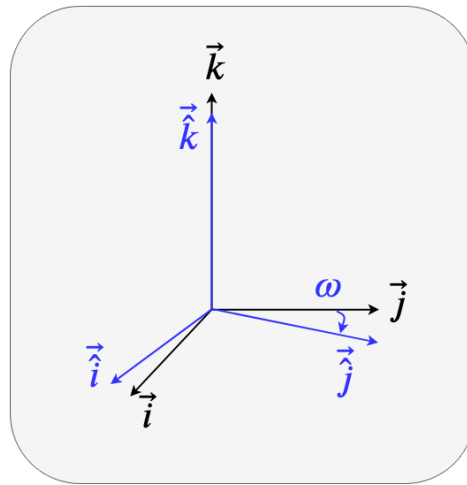


Figure 2.4: Rotating Frame. The system shown in blue represents the rotating frame rotating about z-axis with angular frequency  $\omega$ .

The analysis becomes easier if we consider a rotating frame of reference, rotating with an angular frequency of  $\omega$ , instead of the laboratory frame. To differentiate it from the laboratory frame, the orthogonal axis are denoted as  $\hat{x}$ ,  $\hat{y}$  and  $\hat{z}$ , and their corresponding unit vectors are denoted as  $\vec{\hat{i}}$ ,  $\vec{\hat{j}}$  and  $\vec{\hat{k}}$ . The unit vectors can be transformed between the two reference frames as follows-

$$\begin{bmatrix} \vec{\hat{i}} \\ \vec{\hat{j}} \\ \vec{\hat{k}} \end{bmatrix} = \begin{bmatrix} \cos(\omega t) & -\sin(\omega t) & 0 \\ \sin(\omega t) & \cos(\omega t) & 0 \\ 0 & 0 & 1 \end{bmatrix} \begin{bmatrix} \vec{i} \\ \vec{j} \\ \vec{k} \end{bmatrix} \quad (2.15)$$

so that-

$$\begin{aligned} \vec{\hat{i}} &\triangleq \cos(\omega t)\vec{i} - \sin(\omega t)\vec{j} \\ \vec{\hat{j}} &\triangleq \sin(\omega t)\vec{i} + \cos(\omega t)\vec{j} \\ \vec{\hat{k}} &\triangleq \vec{k} \end{aligned} \quad (2.16)$$

Also, the time derivative of the unit vectors satisfy the relations shown below. We have taken  $\vec{\omega} = -\omega\vec{k}$  here.

$$\frac{d\vec{\hat{i}}}{dt} = \vec{\omega} \times \vec{\hat{i}} \quad \frac{d\vec{\hat{j}}}{dt} = \vec{\omega} \times \vec{\hat{j}} \quad \frac{d\vec{\hat{k}}}{dt} = \vec{\omega} \times \vec{\hat{k}} \quad (2.17)$$

Magnetization in laboratory frame and rotational frame, respectively, can be expressed as follows-

$$\vec{M} \triangleq M_x\vec{i} + M_y\vec{j} + M_z\vec{k} \quad \vec{M}_{rot} \triangleq M_{\hat{x}}\vec{\hat{i}} + M_{\hat{y}}\vec{\hat{j}} + M_{\hat{z}}\vec{\hat{k}} \quad (2.18)$$

And the transformation between them is given by-

$$\begin{bmatrix} M_{\hat{x}} \\ M_{\hat{y}} \\ M_{\hat{z}} \end{bmatrix} = \begin{bmatrix} \cos(\omega t) & -\sin(\omega t) & 0 \\ \sin(\omega t) & \cos(\omega t) & 0 \\ 0 & 0 & 1 \end{bmatrix} \begin{bmatrix} M_x \\ M_y \\ M_z \end{bmatrix} \quad (2.19)$$

By differentiating 2.19 with respect to time using chain rule, and then collecting the terms using 2.17, it can be shown that-

$$\frac{d\vec{M}}{dt} = \frac{\partial \vec{M}_{rot}}{\partial t} + \vec{\omega} \times \vec{M}_{rot} \quad (2.20)$$

This is an important result which we will use later.

Similarly, the  $B_1$  field in the stationary and rotational frame, respectively, can also be expressed as-

$$\vec{B}_1 \triangleq B_{1,x}\vec{i} + B_{1,y}\vec{j} \quad \vec{B}_{1,rot} \triangleq B_{1,\hat{x}}\vec{\hat{i}} + B_{1,\hat{y}}\vec{\hat{j}} \quad (2.21)$$

such that -

$$\begin{bmatrix} B_{1,\hat{x}} \\ B_{1,\hat{y}} \end{bmatrix} = \begin{bmatrix} \cos(\omega t) & -\sin(\omega t) \\ \sin(\omega t) & \cos(\omega t) \end{bmatrix} \begin{bmatrix} B_{1,x} \\ B_{1,y} \end{bmatrix} \quad (2.22)$$

## 2.5. The Bloch Equation

The Bloch equation (equation 2.23) is used to quantitatively describe the time-dependent behavior of  $\vec{M}$ . In addition to the term responsible for precession (first term on the right-hand side), it also includes the terms describing the relaxation process (second and third term) of the spins after they have been disturbed by the RF excitations from the thermal equilibrium magnetization,  $\vec{M}_{eq}$ . The constant  $T_1$  characterizes the time taken by the spin system for

longitudinal relaxation while  $T_2$  characterizes the time taken for transversal relaxation. This relaxation process will be discussed in section 2.7.

$$\boxed{\frac{d\vec{\mathbf{M}}}{dt} = \gamma\vec{\mathbf{M}} \times \vec{\mathbf{B}} - \frac{\vec{\mathbf{M}}_{\perp}}{T_2} - \frac{\vec{\mathbf{M}}_{\parallel} - \vec{\mathbf{M}}_{eq}}{T_1}} \quad (2.23)$$

Where  $\vec{\mathbf{M}}_{\perp}$  is the perpendicular or the transverse component of the magnetization and  $\vec{\mathbf{M}}_{\parallel}$  is the parallel or the longitudinal component of the magnetization.

For our choice of coordinates here, equation 2.23 becomes-

$$\frac{d\vec{\mathbf{M}}}{dt} = \gamma\vec{\mathbf{M}} \times \vec{\mathbf{B}} - \frac{M_x\vec{\mathbf{i}} + M_y\vec{\mathbf{j}}}{T_2} - \frac{(M_z - M_z^0)\vec{\mathbf{k}}}{T_1} \quad (2.24)$$

This equation plays a central part in analyzing the conventional MRI machines as well as the unconventional MRI machine used here.

In the next section, we will see the analysis of the Bloch equation when an RF pulse is applied, which results in an additional  $B_1$  field. The duration of the RF pulse is short as compared to  $T_1$  and  $T_2$ , which makes the first term large. This is why, during a RF excitation, the second and the third term can be dropped. We are then left with the following equation-

$$\frac{d\vec{\mathbf{M}}}{dt} = \gamma\vec{\mathbf{M}} \times \vec{\mathbf{B}} \quad (2.25)$$

We will see that the analysis of the motion of the magnetization becomes simpler if we consider a rotating frame, which has been discussed in section 2.4. In equation 2.25, for rotating frame, the  $\vec{\mathbf{M}}$  and  $\vec{\mathbf{B}}$  on the right hand side are replaced by  $\vec{\mathbf{M}}_{rot}$  and  $\vec{\mathbf{B}}_{rot}$  respectively. For  $\frac{d\vec{\mathbf{M}}}{dt}$  on the left hand side, we have to use equation 2.20. Then we obtain-

$$\begin{aligned} \frac{\partial\vec{\mathbf{M}}_{rot}}{\partial t} &= \gamma\vec{\mathbf{M}}_{rot} \times \vec{\mathbf{B}}_{rot} - \vec{\omega} \times \vec{\mathbf{M}}_{rot} \\ &= \gamma\vec{\mathbf{M}}_{rot} \times \left(\vec{\mathbf{B}}_{rot} + \frac{\vec{\omega}}{\gamma}\right) \\ &= \gamma\vec{\mathbf{M}}_{rot} \times \vec{\mathbf{B}}_{eff} \end{aligned} \quad (2.26)$$

where

$$\vec{\mathbf{B}}_{eff} = \vec{\mathbf{B}}_{rot} + \frac{\vec{\omega}}{\gamma} \quad (2.27)$$

is the effective magnetic field that the magnetization experiences in the rotating frame.

Since the rotating frame is rotating about the z-axis it has no influence on the vector components along this direction. Therefore  $\vec{\mathbf{B}}_{rot} = \vec{\mathbf{B}}_0 = B_0\vec{\mathbf{k}}$ . In this case, the Larmor frequency is  $\vec{\omega} = -\gamma B_0\vec{\mathbf{k}}$ . If we use this in equation 2.27, we get-

$$\vec{\mathbf{B}}_{eff} = \vec{\mathbf{B}}_{rot} + \frac{\vec{\omega}}{\gamma} = B_0\vec{\mathbf{k}} - B_0\vec{\mathbf{k}} = 0 \quad (2.28)$$

It follows from equation 2.26 that  $\frac{\partial\vec{\mathbf{M}}_{rot}}{\partial t} = 0$  and the magnetization appears to be stationary in the rotating frame.

The general Bloch equation in the rotating frame is given by-

$$\frac{\partial\vec{\mathbf{M}}_{rot}}{\partial t} = \gamma\vec{\mathbf{M}}_{rot} \times \vec{\mathbf{B}}_{eff} - \frac{M_x\vec{\mathbf{i}} + M_y\vec{\mathbf{j}}}{T_2} - \frac{(M_z - M_z^0)\vec{\mathbf{k}}}{T_1} \quad (2.29)$$

## 2.6. On-Resonance Excitation

If on top of  $B_0$  field, a RF pulse is applied in the rotating frame such that-

$$\vec{\mathbf{B}}_{1rot} = B_1^e(t)\vec{\mathbf{i}} \quad (2.30)$$

then

$$\begin{aligned} \vec{\mathbf{B}}_{eff} &= B_0\vec{\mathbf{k}} + B_1^e(t)\vec{\mathbf{i}} + \frac{\vec{\omega}_{rf}}{\gamma} \\ &= (B_0 - \frac{\omega_{rf}}{\gamma})\vec{\mathbf{k}} + B_1^e(t)\vec{\mathbf{i}} \end{aligned} \quad (2.31)$$

For the resonance condition to occur, we require  $\omega_{rf} = \omega_0 = \gamma B_0$ . This makes equation 2.31 reduce to -

$$\vec{\mathbf{B}}_{eff} = B_1^e(t)\vec{\mathbf{i}} \quad (2.32)$$

Then the Bloch equation in the rotational frame (equation 2.26) becomes-

$$\begin{aligned} \frac{\partial \vec{\mathbf{M}}_{rot}}{\partial t} &= \gamma \vec{\mathbf{M}}_{rot} \times \vec{\mathbf{B}}_{eff} \\ &= \gamma \vec{\mathbf{M}}_{rot} \times B_1^e(t)\vec{\mathbf{i}} \end{aligned} \quad (2.33)$$

If this  $B_1$  is on for  $\tau_p$  duration, by solving this equation, we get the following solution-

$$\begin{aligned} M_{\hat{x}}(t) &= 0 \\ M_{\hat{y}}(t) &= M_z^0 \int_0^t \sin(\gamma B_1^e(\hat{t}))d\hat{t} \quad 0 \leq t \leq \tau_p \\ M_{\hat{z}}(t) &= M_z^0 \int_0^t \cos(\gamma B_1^e(\hat{t}))d\hat{t} \end{aligned} \quad (2.34)$$

We will assume, henceforth, that the envelope function  $B_1^e$  is a rectangular function,  $\Pi(t)$ . In that case, we have-

$$B_1^e = B_1 \Pi\left(\frac{t - \frac{\tau_p}{2}}{\tau_p}\right), \text{ where } \Pi(t) \triangleq \begin{cases} 1 & |t| < \frac{1}{2} \\ 0 & \text{otherwise} \end{cases} \quad (2.35)$$

Where  $B_1$  is some constant that defines the magnitude of the pulse.

Using 2.35, the solution in equation 2.34 reduces to-

$$\begin{aligned} M_{\hat{x}}(t) &= 0 \\ M_{\hat{y}}(t) &= M_z^0 \sin(\omega_1 t) \quad 0 \leq t \leq \tau_p \\ M_{\hat{z}}(t) &= M_z^0 \cos(\omega_1 t) \end{aligned} \quad (2.36)$$

Where  $\omega_1 = \gamma B_1$ .

In vector form-

$$\vec{\omega}_1 = -\gamma \vec{\mathbf{B}}_1 \quad (2.37)$$

Now we can see that the clockwise precession of  $\vec{\mathbf{M}}$  is about the  $\hat{x}$  axis with angular velocity  $\omega_1$ . This is shown in figure 2.5 a. This precession is called forced precession.

We can also observe that if we turn on  $B_1$  field for  $\tau_p$  duration, such that  $\omega_1 \tau_p = \alpha$ , the magnetization vector is tipped by an  $\alpha$  angle towards the  $\vec{\mathbf{y}}$  axis. This pulse is called  $\alpha$ -pulse.

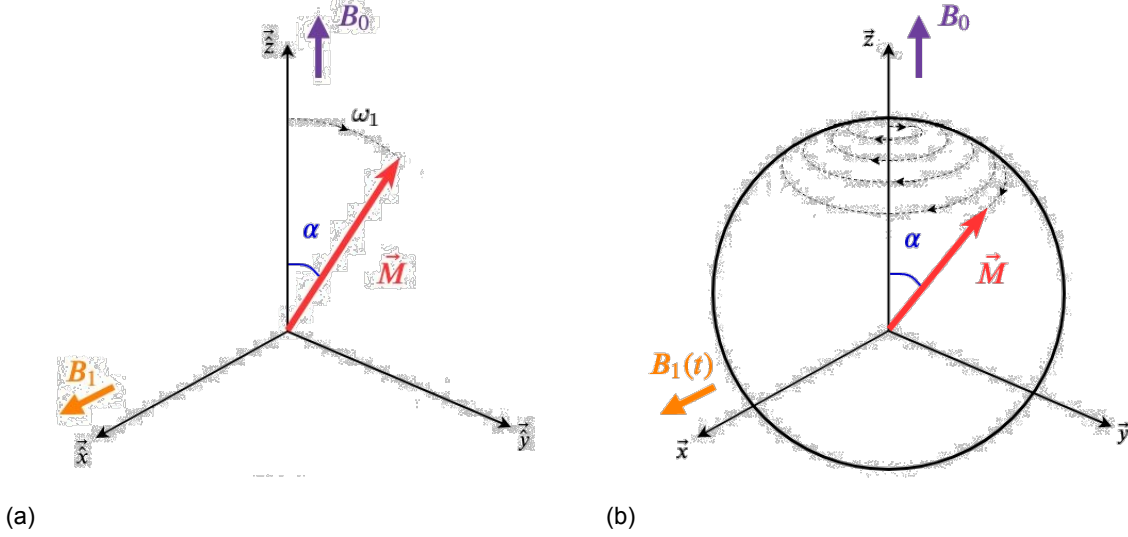


Figure 2.5: The motion of the magnetization  $\vec{M}$  in a) rotating frame or b) laboratory frame. While  $\vec{M}$  appears to spiral down in laboratory frame, in rotating frame, it only appears to precess about the  $\hat{x}$  axis with angular velocity  $\omega_1$ .

## 2.7. Free Precession and Relaxation

So far we have analyzed the Bloch equation under RF excitations. Once this excitation is removed, provided sufficient time is given, the spin system will return to its thermal equilibrium magnetization,  $M_z^0$ . This process takes place by the precession of  $\vec{M}$  about  $B_0$  field which is known as free precession. Here a recovery of the longitudinal magnetization,  $M_z$ , and a destruction of transverse magnetization,  $M_{xy}$ , takes place<sup>1</sup>. These are called longitudinal and transverse relaxation respectively.

We consider the general Bloch equation in the rotating frame (Equation 2.29). If we remove the  $B_1$  field, the first term becomes zero (shown in section 2.5) and we are left with the following-

$$\begin{aligned} \frac{\partial \vec{M}_{rot}}{\partial t} &= \gamma \vec{M}_{rot} \times \vec{B}_{eff} - \frac{M_{\hat{x}} \hat{i} + M_{\hat{y}} \hat{j}}{T_2} - \frac{(M_{\hat{z}} - M_z^0) \hat{k}}{T_1} \\ &= -\frac{M_{\hat{x}} \hat{i} + M_{\hat{y}} \hat{j}}{T_2} - \frac{(M_{\hat{z}} - M_z^0) \hat{k}}{T_1} \end{aligned} \quad (2.38)$$

If we solve the equation 2.38, we get the following solution-

$$\begin{aligned} M_{\hat{x}\hat{y}}(t) &= M_{\hat{x}\hat{y}}(0^+) e^{-\frac{t}{T_2}} \\ M_{\hat{z}}(t) &= M_z^0 (1 - e^{-\frac{t}{T_1}}) + M_{\hat{z}}(0^+) e^{-\frac{t}{T_1}} \end{aligned} \quad (2.39)$$

where  $M_z^0$  is the longitudinal magnetization at thermal equilibrium. The free precession process is preceded by a RF excitation. The instance immediately after the RF pulse have been removed, after it had been applied, is taken as  $t = 0^+$ .  $M_{\hat{x}\hat{y}}(0^+)$  and  $M_{\hat{z}}(0^+)$  are the transverse and longitudinal magnetization at the time instant  $t = 0^+$ .

In laboratory frame, this solutions can be expressed as-

$$\begin{aligned} M_{xy}(t) &= M_{xy}(0^+) e^{-\frac{t}{T_2}} e^{-i\omega_0 t} \\ M_z(t) &= M_z^0 (1 - e^{-\frac{t}{T_1}}) + M_z(0^+) e^{-\frac{t}{T_1}} \end{aligned} \quad (2.40)$$

where

$$M_{xy}(0^+) = M_{\hat{x}\hat{y}}(0^+) e^{-i\omega_0 \tau_p} \quad (2.41)$$

<sup>1</sup>We can arrange  $\vec{M} = M_x \hat{i} + M_y \hat{j} + M_z \hat{k}$  into a transverse component,  $\vec{M}_{xy} = M_x \hat{i} + M_y \hat{j}$ , and a longitudinal component,  $\vec{M}_z = M_z \hat{k}$ , such that-  $\vec{M} = \vec{M}_{xy} + \vec{M}_z$ .

Note that the delay term in equation 2.41 is added to account for the resetting of the time to 0 at the end of the pulse at  $t = \tau_p$ .

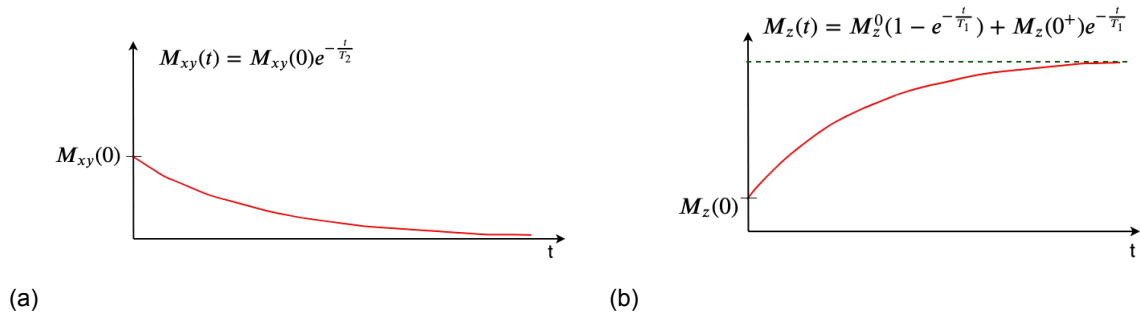


Figure 2.6: Relaxation Curves a) Transversal Relaxation b) Longitudinal Relaxation

Unlike in the RF excitation period, where the magnetization is excited keeping the magnitude same, in the relaxation period, the magnitude of the magnetization is not preserved (illustrated in figure 2.7).

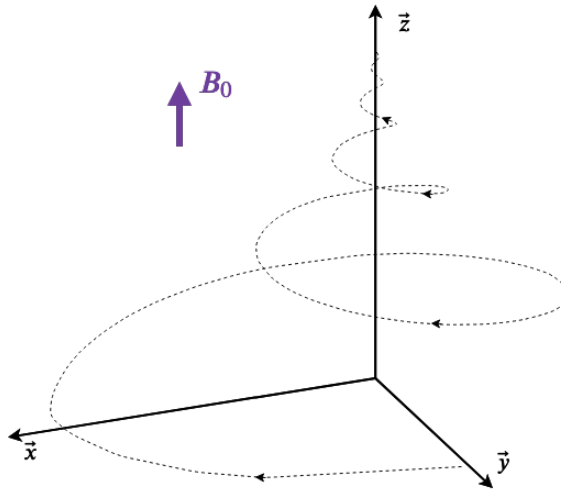


Figure 2.7: The path of the tip of the magnetization vector during free precession in the stationary frame.

## 2.8. Detection of Signal

So far we have discussed the behaviour of magnetization,  $\vec{M}$ , under the influence of external magnetic fields,  $\vec{B}_1$  and  $\vec{B}_0$ . In this part, we will see how this magnetization can be expressed as a voltage signal in the receiving antenna. Not all, but a major part of the discussion to be followed is based on [13].

### 2.8.1. Detection Modeling

We aim to detect the magnetization of the spin, in the patient's body, using a receiver. For this, the receiver and the effect of a spin is modeled as shielded loop antennas<sup>2</sup> (figure 2.8). Loop 1 is considered as the receiver, and loop 2 are the spins in the body. Using this model, we will continue the analysis in the next section.

<sup>2</sup>The configuration of a shielded loop antenna is explained in [13]. It is a loop that creates a magnetic field when current is applied. When it is used as a receiver, it can be used to sense a magnetic field.

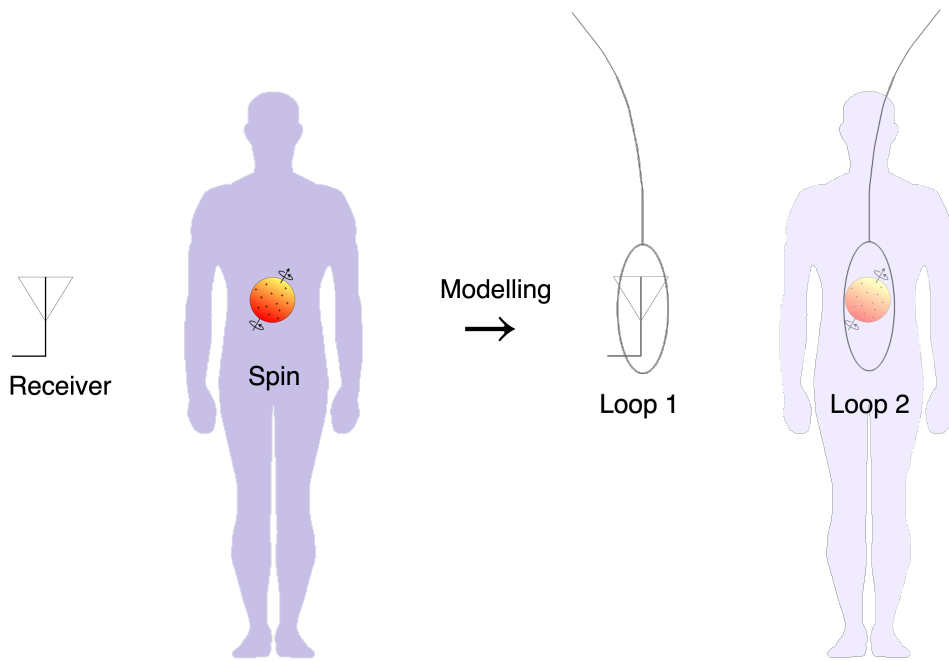


Figure 2.8: The receiver and the effect of a spin is modeled as a conducting shielded loop antenna

### 2.8.2. Induced Voltage

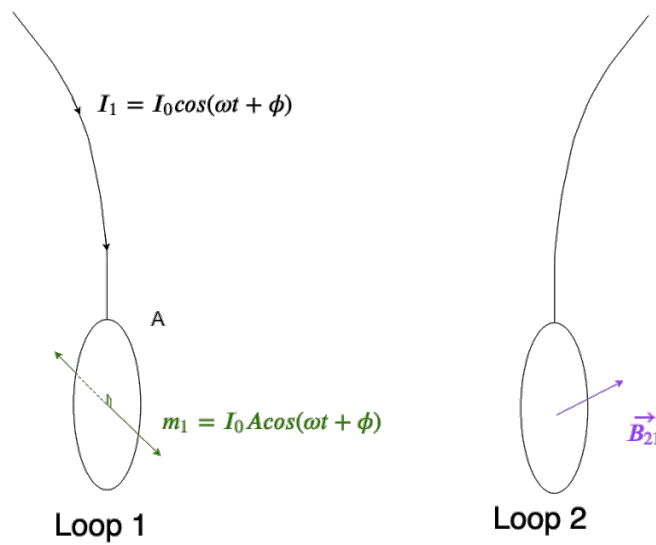


Figure 2.9: Magnetic moment,  $m_1$ , is produced perpendicular to the plane of the shielded loop when current,  $I_1$ , is passed through it.

Let us consider two shielded loop antenna as shown in figure 2.9. When we pass a current  $I_1 = I_0 \cos(\omega t + \phi)$  through Loop 1 we will obtain a magnetic moment,  $m_1 = I_0 A \cos(\omega t + \phi)$ , whose direction is perpendicular to the plane of the loop.  $A$  is the area enclosed by the loop. The current  $I_1$  in Loop 1, will cause a magnetic field,  $\vec{B}_{21}$ , in Loop 2. The straight forward way to calculate  $\vec{B} = \vec{B}_{21}$  is to make use of Maxwell's fourth equation given by-

$$\nabla \times \vec{\mathbf{H}} = \underbrace{\frac{\partial \vec{\mathbf{D}}}{\partial t}}_{\substack{\text{Displacement} \\ \text{Current} \\ \text{Density}}} + \underbrace{\vec{\mathbf{J}}}_{\substack{\text{Conduction} \\ \text{Current} \\ \text{Density}}} + \underbrace{\frac{\partial \vec{\mathbf{P}}}{\partial t}}_{\substack{\text{Polarization} \\ \text{Current} \\ \text{Density}}} + \underbrace{\nabla \times \vec{\mathbf{M}}}_{\substack{\text{Magnetization} \\ \text{Current} \\ \text{Density}}} \quad (2.42)$$

where,

$$\vec{\mathbf{D}} = \epsilon_0 \vec{\mathbf{E}} + \vec{\mathbf{P}} \quad \text{and} \quad \vec{\mathbf{B}} = \mu_0 (\vec{\mathbf{H}} + \vec{\mathbf{M}})$$

The symbols in aforementioned equations mean the following-

$\vec{\mathbf{D}}$ Electric Flux Density	$\vec{\mathbf{B}}$ Magnetic Flux Density
$\vec{\mathbf{E}}$ Electric Field Strength	$\vec{\mathbf{H}}$ Magnetic Field Strength
$\vec{\mathbf{P}}$ Polarization	$\vec{\mathbf{M}}$ Magnetization
$\epsilon_0$ Permittivity of Free Space	$\mu_0$ permeability of Free Space
$\vec{\mathbf{J}}$ Conduction Current Density	

As we can see above, it is very difficult to calculate  $\vec{\mathbf{B}}_{21}$  as it depends on many factors, and knowing only the currents is not enough. But, let us assume that we know this vector, which is  $\vec{\mathbf{B}}_{21}$  at Loop 2.

Maxwell's first equation says-

$$\begin{aligned} \nabla \times \vec{\mathbf{E}} &= \frac{\partial \vec{\mathbf{B}}}{\partial t} \\ \Rightarrow \oint_l \vec{\mathbf{E}} \cdot d\vec{\mathbf{l}} &= \iint_A \frac{\partial \vec{\mathbf{B}}}{\partial t} \cdot d\vec{\mathbf{A}} \quad (\text{Using Stokes Theorem}) \end{aligned} \quad (2.43)$$

The loops considered are taken to be much smaller than the wavelength of the magnetization in the body to be imaged. In other words, a low frequency operation setting is considered. As a result, the voltage in the loop, at any given time can be considered spatially invariant. Using Faraday's Law, and plugging in  $\vec{\mathbf{B}} = \vec{\mathbf{B}}_{21}$ , we can obtain the voltage induced in Loop 2 as-

$$\begin{aligned} \oint_l \vec{\mathbf{E}} \cdot d\vec{\mathbf{l}} &= \iint_A \frac{\partial \vec{\mathbf{B}}_{21}}{\partial t} \cdot d\vec{\mathbf{A}} \\ \Rightarrow V_2 &= -\vec{\mathbf{A}} \cdot \frac{\partial \vec{\mathbf{B}}_{21}}{\partial t} \end{aligned} \quad (2.44)$$

Where  $V_2$  is the voltage induced in Loop 2, and the direction of  $\vec{\mathbf{A}}$  is perpendicular to the plane of the loop.

### 2.8.3. Reciprocity Theorem

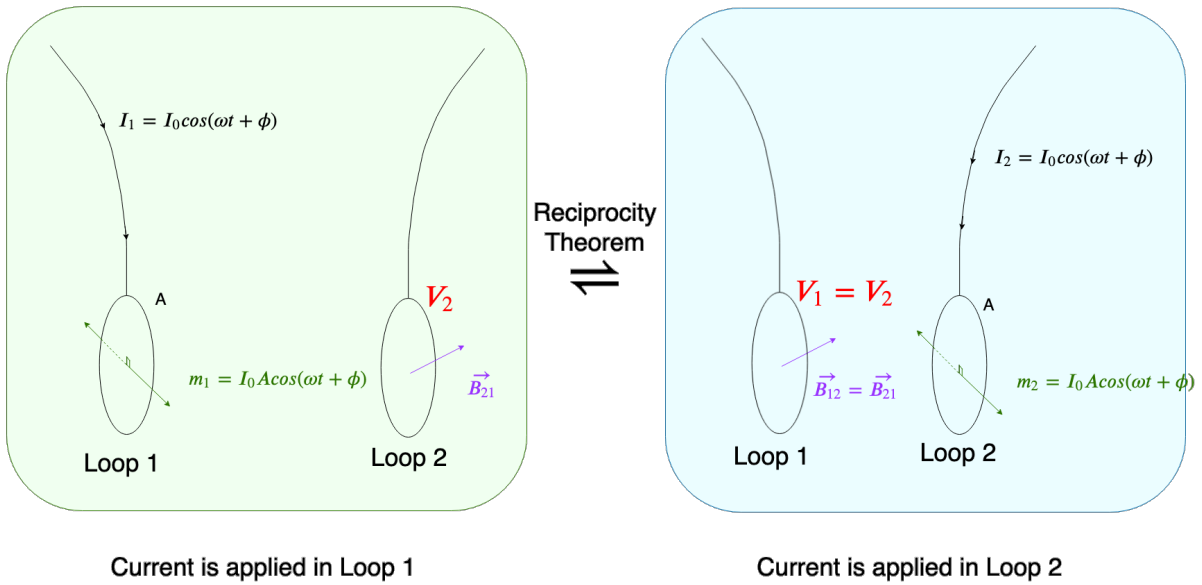


Figure 2.10: Application of the Reciprocity Theorem

According to the Reciprocity Theorem, the response in an observation point of a system to a source does not change when the locations of the source and the observer are interchanged.

In our case (figure 2.10, left), the response is the voltage,  $V_2$ , at the observation point at Loop 2 due to the source current,  $I_1 = I_0 \cos(\omega t + \phi)$ , at Loop 1. Now, if we were to supply the same current in Loop 2,  $I_2 = I_0 \cos(\omega t + \phi)$ , by Reciprocity Theorem, we would get the same response in Loop 1, that is  $V_1 = V_2$  as we had got in Loop 2 in the earlier case.

We consider the following-

1. Suppose, now we apply a different current,  $I_2 = I_1 \cos(\omega t + \phi)$  in loop 2, instead of  $I_2 = I_0 \cos(\omega t + \phi)$ , such that  $\vec{A} I_1 = \vec{M}$ .  $M$  is the magnetic moment at Loop 2 i.e.  $M = m_2$ .
2. We know for  $I_2 = I_0 \cos(\omega t + \phi)$  we get  $V_1 = V_2$ .
3. For  $I_2 = I_1 \cos(\omega t + \phi)$ , using equation 2.44, we get-

$$V_1 = \frac{I_1}{I_0} V_2 = -\vec{A} \frac{I_1}{I_0} \cdot \frac{d\vec{B}_{21}}{dt} = -\vec{A} I_1 \cdot \frac{d}{dt} \left( \frac{\vec{B}_{21}}{I_0} \right) = -\vec{M} \cdot \frac{d}{dt} \vec{B}'_{21}$$

where  $\vec{B}'_{21}$  can be regarded as that magnetic field which would be produced at loop 2 if a unit current in loop 1 is supplied. Thus so far we have-

$$V_1 = -\vec{M} \cdot \frac{d}{dt} \vec{B}'_{21} \quad (2.45)$$

It is to be noted that this derivation assumes a low frequency operation setting. Although it gives some insight, at high frequency settings, this derivation is not adequate (effects of displacement currents cannot be ignored). A more rigorous derivation is given in the paper [13]. For our purpose, for the whole sample, the voltage induced in the receiving coil is given by-

$$V_1(t) = -\frac{d}{dt} \int_{\vec{r} \in \mathbb{D}_{s\text{amp}}} \vec{B}'_{21}(\vec{r}) \cdot \vec{M}(\vec{r}, t) dr \quad \text{for } t \geq 0 \quad (2.46)$$

Where  $\vec{r} = x\vec{i} + y\vec{j} + z\vec{k}$  is a position vector which is in the spatial domain,  $\mathbb{D}_{s\text{amp}}$ , of the sample to be imaged.

To clean up the notation, henceforward,  $V_1(t)$  will be referred as  $V(t)$ , and  $\vec{\mathbf{B}}_{21}$  will be referred as  $\vec{\mathbf{B}}_r$  (where  $r$  implies that it is the receive field).  $\vec{\mathbf{M}}(\mathbf{r}, t)$  is the magnetization in the object. The negative sign will be ignored since it only has an effect of multiplying by  $-1$ , and it does not change the signal. Thus we have-

$$V(t) = \frac{d}{dt} \int_{\vec{\mathbf{r}} \in \mathbb{D}_{samp}} \vec{\mathbf{B}}_r(\vec{\mathbf{r}}) \cdot \vec{\mathbf{M}}(\vec{\mathbf{r}}, t) dr \quad \text{for } t \geq 0 \quad (2.47)$$

## 2.9. Signal Expression

In this section, we are going to see the form a MRI signal takes. We proceed to work on equation 2.47 we saw in the previous section 2.8.

$$\begin{aligned} V(t) &= \frac{d}{dt} \int_{\vec{\mathbf{r}} \in \mathbb{D}_{samp}} \vec{\mathbf{B}}_r(\vec{\mathbf{r}}) \cdot \vec{\mathbf{M}}(\vec{\mathbf{r}}, t) dr \\ &= \frac{d}{dt} \int_{\vec{\mathbf{r}} \in \mathbb{D}_{samp}} [B_{r,x}(\vec{\mathbf{r}})\hat{\mathbf{i}} + B_{r,y}(\vec{\mathbf{r}})\hat{\mathbf{j}} + B_{r,z}(\vec{\mathbf{r}})\hat{\mathbf{k}}] \cdot [M_x(\vec{\mathbf{r}}, t)\hat{\mathbf{i}} + M_y(\vec{\mathbf{r}}, t)\hat{\mathbf{j}} + M_z(\vec{\mathbf{r}}, t)\hat{\mathbf{k}}] dr \\ &= \int_{\vec{\mathbf{r}} \in \mathbb{D}_{samp}} [\hat{B}_{r,x}(\vec{\mathbf{r}})\hat{\mathbf{i}} + \hat{B}_{r,y}(\vec{\mathbf{r}})\hat{\mathbf{j}} + \hat{B}_{r,z}(\vec{\mathbf{r}})\hat{\mathbf{k}}] \cdot \left[ \frac{d}{dt} M_x(\vec{\mathbf{r}}, t)\hat{\mathbf{i}} + \frac{d}{dt} M_y(\vec{\mathbf{r}}, t)\hat{\mathbf{j}} + \frac{d}{dt} M_z(\vec{\mathbf{r}}, t)\hat{\mathbf{k}} \right] dr \end{aligned} \quad (2.48)$$

The last term,  $M_z(\mathbf{r}, t)$ , is slowly varying with respect to time and therefore can be ignored. We are left with-

$$V(t) = \int_{\vec{\mathbf{r}} \in \mathbb{D}_{samp}} [B_{r,x}(\vec{\mathbf{r}}) \frac{d}{dt} M_x(\vec{\mathbf{r}}, t) + B_{r,y}(\vec{\mathbf{r}}) \frac{d}{dt} M_y(\vec{\mathbf{r}}, t)] dr \quad (2.49)$$

From section 2.7, equation 2.40, we use the expression for  $\vec{\mathbf{M}}(\vec{\mathbf{r}}, t)$  to be substituted in equation 2.49. Subsequently low pass filtering it, which is described in [14], we are left with the following signal model-

$$S(t) = \int_{\vec{\mathbf{r}} \in \mathbb{D}_{samp}} B_{r,xy}^*(\vec{\mathbf{r}}) M_{xy}(\vec{\mathbf{r}}, 0^+) e^{-\frac{t}{T_2}} e^{-i\Delta\omega(\vec{\mathbf{r}})t} dr \quad (2.50)$$

where-

$$\begin{aligned} B_{r,xy}^*(\vec{\mathbf{r}}) &= B_{r,x}(\vec{\mathbf{r}}) - iB_{r,y}(\vec{\mathbf{r}}) \\ M_{xy}(\vec{\mathbf{r}}, 0^+) &= M_x(\vec{\mathbf{r}}, 0^+) + iM_y(\vec{\mathbf{r}}, 0^+) \\ \Delta\omega(\vec{\mathbf{r}}) &= \omega_0(\vec{\mathbf{r}}) - \omega_{mod} \Rightarrow \Delta B(\vec{\mathbf{r}}) = B_0(\vec{\mathbf{r}}) - B_{mod} \end{aligned}$$

Here  $\omega_{mod}$  is the modulation frequency that comes from the filtering process of the signal. Thus, we have our signal model as-

$$\boxed{S(t) = \int_{\vec{\mathbf{r}} \in \mathbb{D}_{samp}} B_{r,xy}^*(\vec{\mathbf{r}}) M_{xy}(\vec{\mathbf{r}}, 0^+) e^{-\frac{t}{T_2}} e^{-iy\Delta B(\vec{\mathbf{r}})t} dr} \quad (2.51)$$

## 2.10. Free Induction Decay

Free induction decay (FID) signals are MRI signals that are obtained from the free precessing of the spins. To have more insight, we continue from where we had left in the previous section.

In equation 2.50,  $B_{r,xy}^*$  reflects on the sensitivity of the receiving coil. For the sake of analysis, for now, this term is considered spatially uniform everywhere inside the machine.

Then we can ignore this term as the only effect it would have is to scale the image, since it is now just a constant<sup>3</sup>. Thus we have-

$$S(t) = \int_{\vec{r} \in \mathbb{D}_{\text{samp}}} M_{xy}(\vec{r}, 0^+) e^{-\frac{t}{T_2}} e^{-i\omega t} d\vec{r} \quad (2.52)$$

Where  $\Delta\omega$  is written as  $\omega$  for notational convenience. In this report,  $\Delta\omega$  and  $\omega$  are interchangeably used, and the meaning should be apparent from the context itself.

So far, inherently, an ideal spin system, where all the spins precess with the same angular frequency, has been considered. But in reality, the spin systems are always heterogeneous, meaning that the spins belonging to a system precess with different angular frequencies. To characterize the frequency distribution in a system, the spin spectral density function,  $\rho(\omega)$ , is used which is defined as-

$$\rho(\omega) = \frac{dM(\omega)}{d\omega} \quad (2.53)$$

Where  $dM(\omega)$  are the isochromatic bulk magnetization, meaning that the spins responsible for this magnetization are precessing with the same frequency  $\omega$ . For the whole sample, equation 2.52 can be written as-

$$S(t) = \int_{-\infty}^{\infty} \rho(\omega) e^{-\frac{t}{T_2(\omega)}} e^{-i\omega t} d\omega \quad (2.54)$$

As an example let us consider a case when the sample is placed in an inhomogeneous magnetic field with a Lorentzian distribution[14]. This will illustrate the effect an inhomogeneous magnetic field has on MRI signals. In this case, the spectral spin density is given by-

$$\rho(\omega) = M_z^0 \frac{(\gamma\Delta B)^2}{(\gamma\Delta B)^2 + (\omega - \omega_0)^2} \quad (2.55)$$

For an  $\alpha$ -pulse, the FID signal takes the form

$$S(t) = \sin(\alpha) \int_{-\infty}^{\infty} \rho(\omega) e^{-\frac{t}{T_2(\omega)}} e^{-i\omega t} d\omega \quad (2.56)$$

In an inhomogeneous magnetic field with a Lorentzian distribution, this FID signal becomes-

$$\begin{aligned} S(t) &= \sin(\alpha) \int_{-\infty}^{\infty} M_z^0 \frac{(\gamma\Delta B)^2}{(\gamma\Delta B)^2 + (\omega - \omega_0)^2} e^{-\frac{t}{T_2(\omega)}} e^{-i\omega t} d\omega \\ &= \pi M_z^0 \gamma \Delta B \sin(\alpha) e^{-\gamma \Delta B t} e^{-\frac{t}{T_2}} e^{-i\omega_0 t} \\ &= \pi M_z^0 \gamma \Delta B \sin(\alpha) e^{-\frac{t}{T_2^*}} e^{-i\omega_0 t} \end{aligned} \quad (2.57)$$

where,

$$\frac{1}{T_2^*} = \frac{1}{T_2} + \gamma \Delta B \quad (2.58)$$

Thus, we see that the signal decays faster than that characterized by  $T_2$ . This signal is characterized by  $T_2^*$  which takes into account the inhomogeneous magnetic field with a Lorentzian distribution. Although equation 2.58 is valid for Lorentzian spectral density functions, it is widely used in MRI literature. For other types of distribution, the FID may not be an exponential function. But the general thing to note here is that when the field is inhomogeneous, the signals decay faster than what is characterized by only  $T_2$ .

<sup>3</sup>If the receive field is not constant, we will have to account for this term, which is spatially varying, in the signal model. In [5], they use more than one receiving antennae, with different spatially varying receive field maps, to differentiate between the non-bijective mappings of the inhomogeneous background field and the locations. This will be more clear in the next chapter, and further information can be obtained from [5].

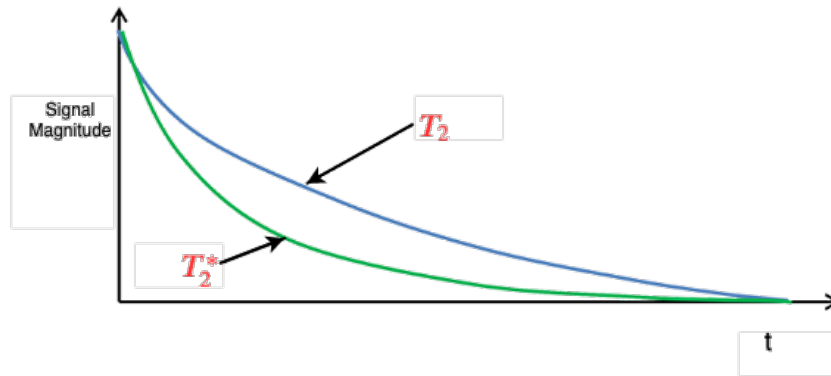


Figure 2.11: The FID signal characterized by  $T_2^*$  decays faster due to an inhomogeneous magnetic field

# 3

## Rotating MRI machine

Traditional clinical MRI scanners use high-cost superconducting wires to create strong homogeneous magnetic fields of the order 1.5 to 3 tesla. It needs cryogenic liquid cooling systems as it generates an enormous amount of heat. This needs high power supplies and expensive electronic circuits. Furthermore, highly trained technicians are required to repair such machines if something breaks down. For developing countries, which are in need of affordable diagnostic devices, but have limited financial resources, this is a problem. A portable low-cost MRI would provide major benefits in such a situation.

The specific medical application of the project, of which this work is a part, aims to improve the diagnosis of Hydrocephalus of infants in Uganda. Hydrocephalus is a condition where a collection of cerebrospinal fluid (CSF) occurs within the brain. The Low-field MRI group is developing two solutions of inexpensive portable low-field MRI scanner to address this problem. These two solutions are different in the way the spatial information is encoded. The first one (shown in figure 3.1a), uses switching gradients, like in traditional MRI, to encode the spatial information when the field inhomogeneities are not too strong. The advantage of this one is that we can use more traditional reconstruction techniques like Fourier transform, which are fast. The implementation details of such systems are fairly well understood, and literature regarding it is widely available. The second solution (shown in figure 3.1b) encodes spatial information by using an inhomogeneous background field. The advantage of this solution is that less electronic hardware is required. However, this is not a mature technology, and much of it remains to be explored. The process of spatial encoding will be discussed more in this chapter.

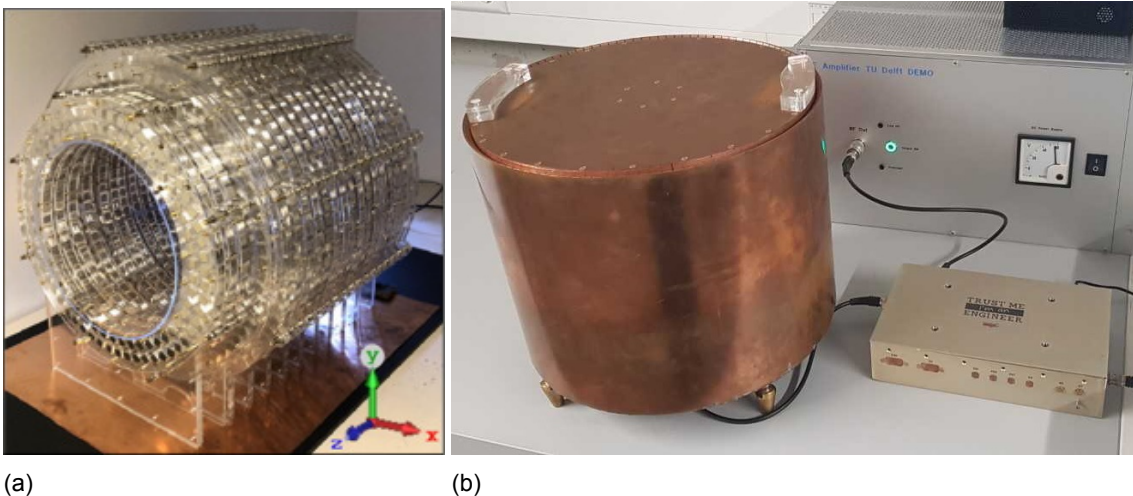


Figure 3.1: a) Prototype of the solution that encodes information using linear gradients. Picture is taken from [17]. b) Prototype of the solution that encodes information using inhomogeneous background field.

The partner institutions involved with this project are - Leiden University Medical Center, Pennsylvania State University, Mbarara University of Science and Technology, CURE Children's Hospital of Uganda, and TU Delft.

The objective of this chapter is to completely explain the purpose of this thesis. It begins with an explanation of using the MRI signal model to image objects with homogeneous and gradient magnetic fields. After that, the motivation for using an inhomogeneous magnetic field is given, followed by a basic description of its implementation. Towards the end, it states what work has already been done by others, in this direction, and what this work has to offer.

### 3.1. Imaging with Signal Model

We have seen in Chapter 2, equation 2.52, the signal model for FID. This is again shown below. For the sake of the simplicity of understanding, the  $B_{r,xy}^*(\vec{r})$  term is considered a constant, and is ignored here.

$$S(t) = \int_{\vec{r} \in \mathbb{D}_{smp}} M_{xy}(\vec{r}, 0^+) e^{-\frac{t}{T_2}} e^{-i\omega t} dr$$

We consider the signal contribution due to an infinitesimal interval  $dr$  at position vector  $\vec{r}$ .

$$dS(t) = M_{xy}(\vec{r}, 0^+) e^{-\frac{t}{T_2}} e^{-i\omega t} dr \quad (3.1)$$

The term  $M_{xy}(\vec{r}, 0^+)$  depends upon the magnetization at equilibrium,  $\vec{M}_{eq}$ , which in turn depends upon the spin density,  $\rho(\vec{r})$ . We can see this in equation 2.9, where spin density is dependent on the number of spins,  $N_s$ , at  $\vec{r}$ . Thus, after regarding the other parameters as constants, and omitting the transverse relaxation effect, we have-

$$dS(t) \propto \rho(\vec{r}) e^{-i\omega t} dr \quad (3.2)$$

Further, ignoring the scaling constants, and considering the signal due to the whole object, we have-

$$S(t) = \int_{\vec{r} \in \mathbb{D}_{smp}} \rho(\vec{r}) e^{-i\omega t} dr \quad (3.3)$$

The discrete version of this equation is-

$$S(k_m) = \sum_n \rho(r_n) e^{-i\gamma \Delta B(r_n) k_m \Delta r} \quad (3.4)$$

where,  $k_m$  is the  $m^{\text{th}}$  discrete time sample,  $r_n$  is the position at  $n^{\text{th}}$  index and  $\Delta r$  is the area of the pixel.

$r_1$	·	·	·	·
$r_2$	·	·	·	·
·	·	$r_n$	·	$r_{N-1}$
·	·	·	·	$r_N$

Figure 3.2: Discretization of the image domain. Indices of the positions increase from top to bottom per column. Once the indices reach the bottom-most element of its column, it continues from the topmost element of the adjacent right column. Area of each pixel is  $\Delta r$ .

Ignoring the area of the pixel because it is a constant, and writing 3.4 in a matrix form, we get-

$$\begin{aligned} \begin{bmatrix} S(k_1) \\ S(k_2) \\ \vdots \\ S(k_M) \end{bmatrix} &= \begin{bmatrix} e^{-i\gamma\Delta B(r_1)k_1} & e^{-i\gamma\Delta B(r_2)k_1} & \dots & e^{-i\gamma\Delta B(r_N)k_1} \\ e^{-i\gamma\Delta B(r_1)k_2} & e^{-i\gamma\Delta B(r_2)k_2} & \dots & e^{-i\gamma\Delta B(r_N)k_2} \\ \vdots & \vdots & \ddots & \vdots \\ e^{-i\gamma\Delta B(r_1)k_M} & e^{-i\gamma\Delta B(r_2)k_M} & \dots & e^{-i\gamma\Delta B(r_N)k_M} \end{bmatrix} \begin{bmatrix} \rho(r_1) \\ \rho(r_2) \\ \vdots \\ \rho(r_N) \end{bmatrix} \\ \Rightarrow \mathbf{S} &= \mathbf{E} \boldsymbol{\rho} \end{aligned} \quad (3.5)$$

where  $M$  is the total number of time samples, and  $N$  is the total position indices.  $\mathbf{S}$  is the signal matrix,  $\mathbf{E}$  is the encoding matrix, and  $\boldsymbol{\rho}$  is the spin density.

We have seen in the previous chapter (Equation 2.50) that

$$\Delta\omega(\mathbf{r}) = \omega_0(\mathbf{r}) - \omega_{mod}$$

$\omega_0$  is the frequency when we apply a homogeneous field  $\vec{\mathbf{B}}_0$ . For a general magnetic field,  $\vec{\mathbf{B}}$ , we would have-

$$\Delta\omega(\mathbf{r}) = \omega(\mathbf{r}) - \omega_{mod} \quad (3.6)$$

In practice,  $\omega_{mod}$ , is chosen to be  $\omega_0$ . A point to be noted is that this  $\omega_{mod}$  is chosen by the user and the external field has no effect on it unlike the first term on the right hand side of equation 3.6. We then have-

$$\begin{aligned} \Delta\omega(\mathbf{r}) &= \omega(\mathbf{r}) - \omega_0 \\ \Rightarrow \Delta B(\mathbf{r}) &= B(\mathbf{r}) - B_0 \end{aligned} \quad (3.7)$$

If we use a homogeneous external field,  $B(\mathbf{r}) = B_0$ , we will get  $\Delta B(\mathbf{r}) = 0$ . This means that the rank of the encoding matrix  $\mathbf{E}$  will become 1, which means that it has only one independent column vector. We will never be able to reconstruct  $\boldsymbol{\rho}$  using this  $\mathbf{E}$  unless  $\mathbf{S}$  lies along that independent vector which is highly unlikely.

To do spatial localization, or in other words, to identify  $\rho(\vec{\mathbf{r}})$  for each location there are two ways to do it - i) Slice Selection and ii) Spatial encoding. Both of these ways require the use of a gradient coil system in the MRI machines that are in use today. The description of these techniques is **not** provided in this report and can be referred from Chapter 5 and Chapter 6 of [14]. Further, there are different ways to encode spatial information in the MRI signal in the signal encoding process. Essentially, there are two- i) frequency encoding, and ii) phase encoding. How to do these encoding processes, and what the measured signal is telling us, depends a lot on the pulse sequences that are applied during the whole process of acquisition. Pulse sequences refer to the order in which the Rf coils and the gradient coils are turned on and off. And based on the acquisition process, the reconstruction process also varies. As mentioned before, more insight can be got from [14].

Assuming that the reader has some idea of what is mentioned above, the subsequent sections attempt to answer briefly why Fourier transform can be used when gradient magnetic fields are used, and why the same cannot be employed when the field is inhomogeneous.

## 3.2. Linear Gradient Field Imaging

In the previous section, we saw that it is usually not possible to reconstruct the image (the spin density  $\boldsymbol{\rho}$ ) if we only use a homogeneous external field (Figure 3.3).

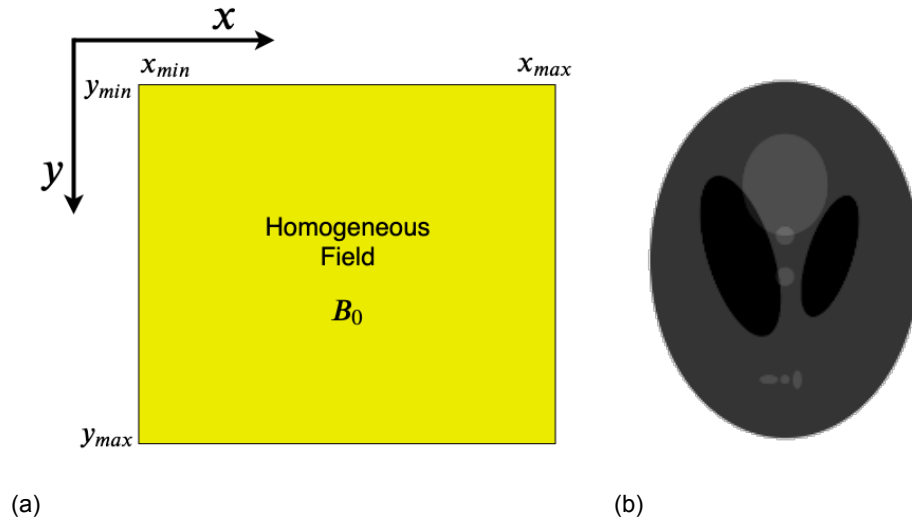


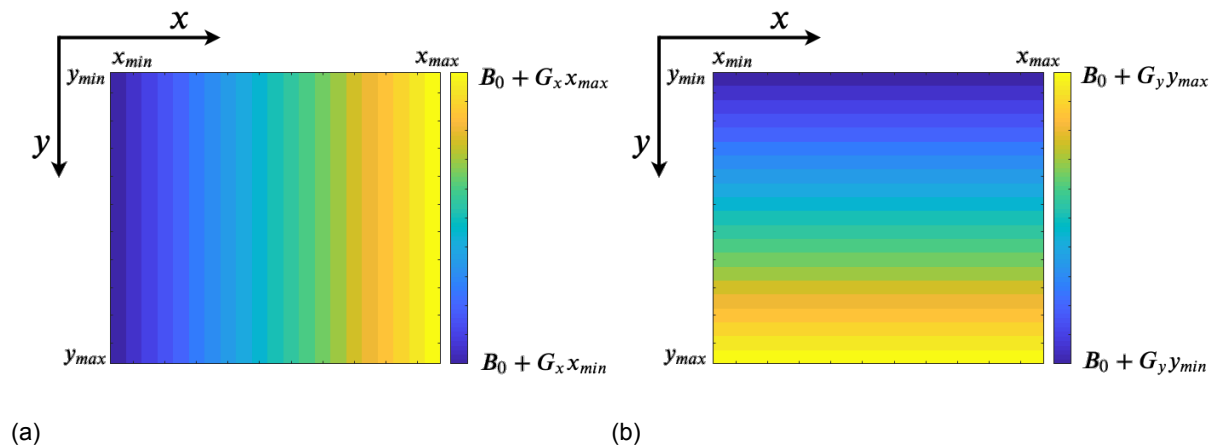
Figure 3.3: a) Homogeneous external field  $B_0$  b) A Shepp Logan phantom that we are trying to image by placing is in the external magnetic field

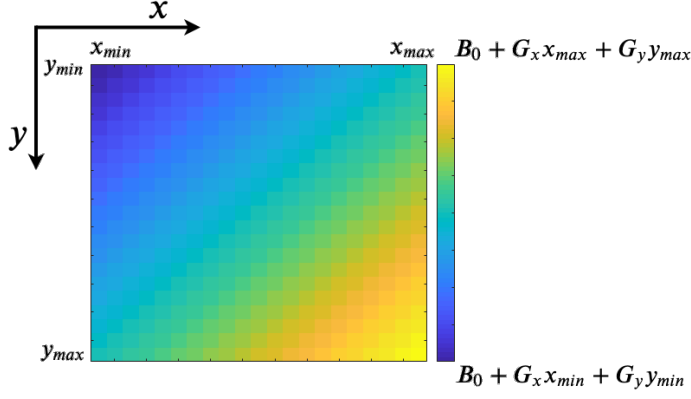
Suppose, now, on top of the homogeneous magnetic field we add a gradient field, which increases in magnitude linearly as we traverse through the x-axis (Figure 3.4 a). Then the total magnetic field becomes  $B(\mathbf{r}) = B_0 + G_x x(\mathbf{r})$ , where  $G_x(\mathbf{r})$  is a constant. As a result, equation 3.7 becomes -

$$\begin{aligned} \Delta B(\mathbf{r}) &= B_0 + G_x x(\mathbf{r}) - B_0 \\ \Rightarrow \Delta B(\mathbf{r}) &= G_x x(\mathbf{r}) \end{aligned} \quad (3.8)$$

Then we will have-

$$\begin{aligned} \begin{bmatrix} S(k_1) \\ S(k_2) \\ \vdots \\ S(k_M) \end{bmatrix} &= \begin{bmatrix} e^{-i\gamma k_1 G_x x(r_1)} & e^{-i\gamma k_1 G_x x(r_2)} & \dots & e^{-i\gamma k_1 G_x x(r_N)} \\ e^{-i\gamma k_2 G_x x(r_1)} & e^{-i\gamma k_2 G_x x(r_2)} & \dots & e^{-i\gamma k_2 G_x x(r_N)} \\ \vdots & \vdots & \ddots & \vdots \\ e^{-i\gamma k_M G_x x(r_1)} & e^{-i\gamma k_M G_x x(r_2)} & \dots & e^{-i\gamma k_M G_x x(r_N)} \end{bmatrix} \begin{bmatrix} \rho(r_1) \\ \rho(r_2) \\ \vdots \\ \rho(r_N) \end{bmatrix} \\ \Rightarrow \mathbf{S} &= \mathbf{E}_{G_x} \boldsymbol{\rho} \end{aligned} \quad (3.9)$$





(c)

Figure 3.4: a) Gradient field along x direction b) Gradient field along y direction c) Gradient field along both x and y direction

We should note that  $\mathbf{E}_{G_x}$  is essentially a 1D Fourier transform matrix. That means we have encoded the spatial information along the x-axis. But we still cannot differentiate between the y positions. In our measurement, using this matrix gives us the projection of the object on the x-axis. One might be tempted to think that in order to distinguish between the y positions, another gradient field,  $G_y y(\mathbf{r})$ , should be added along y direction (3.4b), such that the resulting total magnetic field looks something like figure 3.4c. Subsequently,  $\Delta B(\mathbf{r})$  will become-

$$\begin{aligned} \Delta B(\mathbf{r}) &= B_0 + G_x x(\mathbf{r}) + G_y y(\mathbf{r}) - B_0 \\ \Rightarrow \Delta B(\mathbf{r}) &= G_x x(\mathbf{r}) + G_y y(\mathbf{r}) \end{aligned} \quad (3.10)$$

But this would only encode the projection of the image along the line characterized by  $G_x x(\mathbf{r}) + G_y y(\mathbf{r})$  and will still be a sort of one dimensional imaging of a 2D image slice. Accordingly,

$$\begin{aligned} \begin{bmatrix} S(k_1) \\ S(k_2) \\ \vdots \\ S(k_M) \end{bmatrix} &= \begin{bmatrix} e^{-i\gamma k_1(G_x x(r_1) + G_y y(r_1))} & e^{-i\gamma k_1(G_x x(r_2) + G_y y(r_2))} & \dots & e^{-i\gamma k_1(G_x x(r_N) + G_y y(r_N))} \\ e^{-i\gamma k_2(G_x x(r_1) + G_y y(r_1))} & e^{-i\gamma k_2(G_x x(r_2) + G_y y(r_2))} & \dots & e^{-i\gamma k_2(G_x x(r_N) + G_y y(r_N))} \\ \vdots & \vdots & \ddots & \vdots \\ e^{-i\gamma k_M(G_x x(r_1) + G_y y(r_1))} & e^{-i\gamma k_M(G_x x(r_2) + G_y y(r_2))} & \dots & e^{-i\gamma k_M(G_x x(r_N) + G_y y(r_N))} \end{bmatrix} \begin{bmatrix} \rho(r_1) \\ \rho(r_2) \\ \vdots \\ \rho(r_N) \end{bmatrix} \\ \Rightarrow \mathbf{S} &= \mathbf{E}_{G_{xy}} \boldsymbol{\rho} \end{aligned} \quad (3.11)$$

This encoding matrix,  $\mathbf{E}_{G_{xy}}$ , has the same form as a 2D Fourier transform matrix. That means if we take the inverse fourier transform of  $\mathbf{S}$ , we get back the projection of  $\boldsymbol{\rho}$  on the line, L, characterized by  $G_x x(\mathbf{r}) + G_y y(\mathbf{r})$ .

$$\mathbf{S} \xrightarrow{\mathcal{F}^{-1}} \text{proj}_L \boldsymbol{\rho} \quad (3.12)$$

A true 2D imaging of an object is based on more than one step of the spatial encoding process, mentioned above. Depending upon the type of spatial encoding desired ( frequency or phase encoding[14]), the  $G_x x(\mathbf{r})$  and  $G_y y(\mathbf{r})$  are varied appropriately to obtain the corresponding encoding matrices. These matrices are then stacked to get the total system matrix, which is then used for reconstructing a 2D image. To get an insight into how multi-dimensional (2D and 3D) imaging are done, the reader is referred to chapter 5 of [14].

### 3.3. Inhomogeneous field Imaging

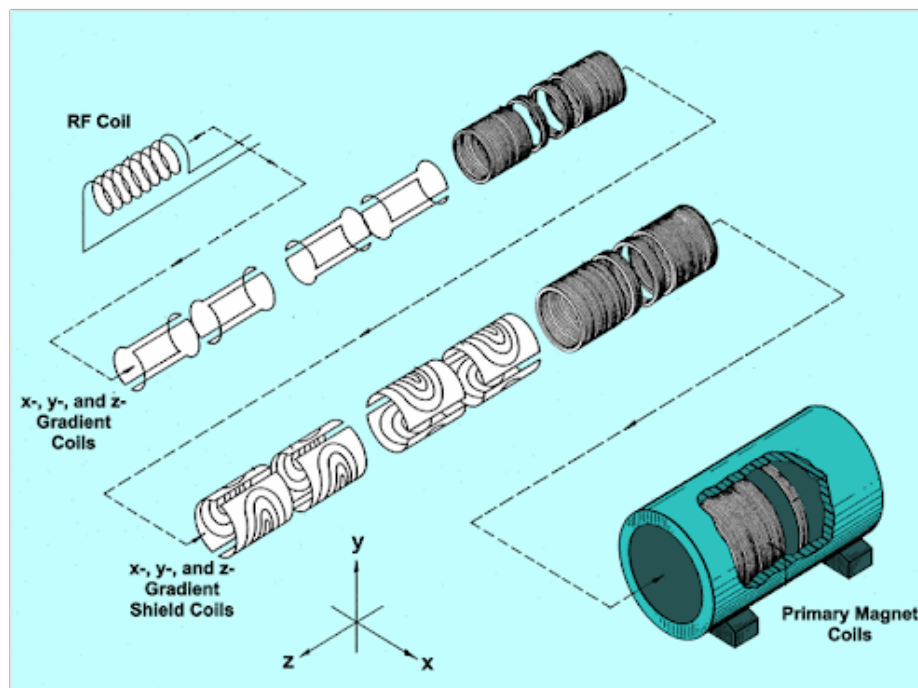


Figure 3.5: Components of MRI system. Source of picture: <http://mriquestions.com/active-shielded-gradients.html>

Conventional MRI scanners image an object using gradient fields in three dimensions. The structure of the signal model for 3D imaging, which they use, looks like this-

$$\begin{aligned}
 S(t) &= \int_{\vec{r} \in \mathbb{D}_{\text{samp}}} \rho(\vec{r}) e^{-i\gamma \Delta B(\vec{r})t} d\vec{r} \\
 \Rightarrow S(t) &= \int_{\vec{r} \in \mathbb{D}_{\text{samp}}} \rho(\vec{r}) e^{-i\gamma((B_0(\vec{r}) + G_x x(\vec{r}) + G_y y(\vec{r}) + G_z z(\vec{r})) - B_{\text{mod}})t} d\vec{r} \quad (\text{Using equation 3.7})
 \end{aligned} \tag{3.13}$$

The  $B_0(\mathbf{r})$  term is supplied by the primary magnet coils, and the gradient terms  $G_x x(\mathbf{r})$ ,  $G_y y(\mathbf{r})$  and  $G_z z(\mathbf{r})$  are supplied by the gradient coils (Figure 3.5). It is to be noted that the field provided by the primary magnet has to be as homogeneous as possible. The strength of it also needs to be very high as the SNR of MRI improves with the strength of the magnet [12]. As for the gradient coils, it has to provide a gradient that is as linear as possible. Complex gradient amplifiers are required to provide well-synchronized gradient pulses. Moreover, gradient coils also adds more weight to the primary magnet, which makes the whole system bulky.

The whole point of the machine used in this work is to address the above challenges. It relaxes the homogeneous magnetic field criteria by using an inhomogeneous magnetic field to do the spatial encoding instead of switching gradients. This system is less bulky and simpler as it does not require gradient coils. To make it portable, superconducting magnets are no longer used. Instead, a cylindrical Halbach Magnet array is used which is a certain arrangement of permanent magnets that increases the magnetic flux on one side while reducing or canceling it on the opposite side [1][15][21]. Although Halbach array tries to maximize field strength, it is not comparable to that of superconducting magnets. A lower field strength implies lower SNR. Therefore, robust reconstruction algorithms have to be employed.

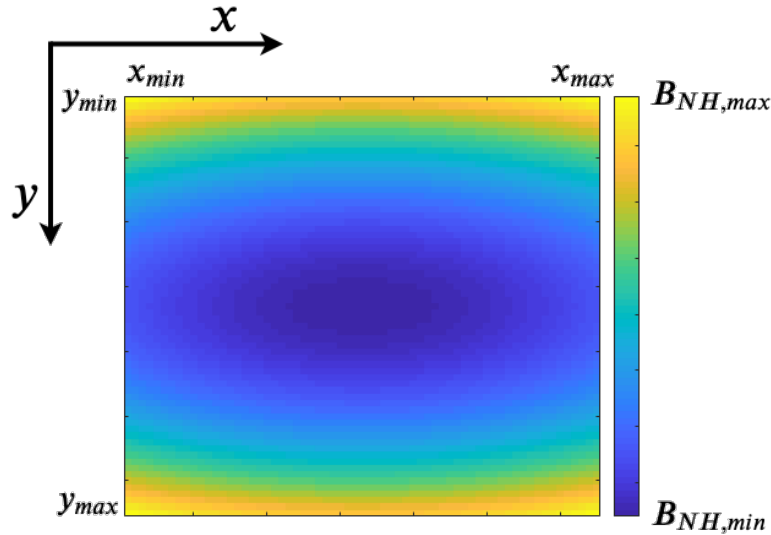
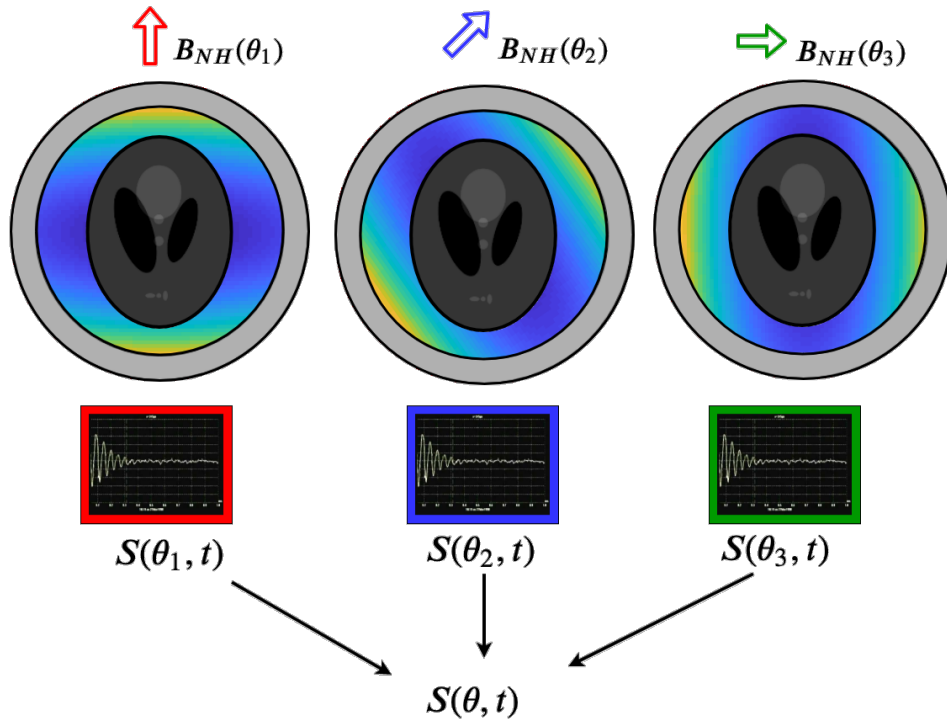


Figure 3.6: Inhomogeneous Magnetic Field

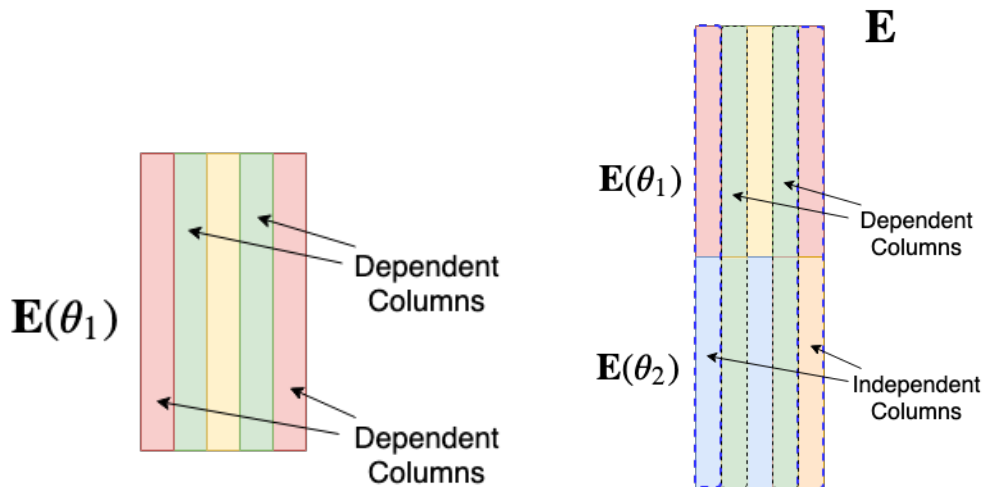
We consider the inhomogeneous magnetic field,  $B_{NH}$ , in figure 3.6. Suppose, as an example, we want to use this field to image the object shown in Figure 3.3b.

Using this inhomogeneous magnetic field, we will get more number of independent columns of the encoding matrix than the homogeneous case (discussed in section 3.1). But this number will be less than the case where gradient fields are used (section 3.2). This is apparent from figure 3.6, where we can see that many pixels have the same magnetic field. Mathematically, this means that there are more non-bijective mapping between the locations and the magnetic field than the gradient field case. We cannot use Fourier transform now because the encoding matrix does not have the same form as the Fourier transform matrix as before. Thus, we should rely on other reconstruction techniques which are described in chapter 6.

To try to increase the number of independent columns, so that the solution is searched over a larger sub-space, the object is imaged by using several rotated version of the inhomogeneous magnetic field,  $B_{NH}$  (shown in figure 3.7a). This also means that it helps in disambiguating the non-bijective mappings. Suppose 3.7b depicts the columns of the encoding matrix,  $\mathbf{E}(\theta_1)$ , when  $B_{NH}$  map makes an angle  $\theta_1$  with some reference axis. We assume that the same colors of the columns mean that they are dependent. Next, we view the object by rotating  $B_{NH}$  such that it makes  $\theta_2$  with the same reference. We stack the encoding matrix,  $\mathbf{E}(\theta_2)$ , of this angle,  $\theta_2$ , under  $\mathbf{E}(\theta_1)$ , in the hope of increasing the number of independent columns of the stacked encoding matrix,  $\mathbf{E}$ . Figure 3.7c depicts this. The columns of  $\mathbf{E}$  will be independent or dependent depending upon the map of the inhomogeneous field map. For example, if the map would have been concentric circles, rotating the field will not give us new information as the same image will be obtained for each angle. In other words, the same columns would be stacked for each angle.



(a)



(b)

(c)

Figure 3.7: a) Imaging with rotating inhomogeneous magnetic field  $B_{NH}$  b) Depiction of encoding matrix at  $\theta_1$  c) Depiction stacked encoding matrix.

### 3.4. Previous Work

We have seen that the traditional MRI machines use high strength linear spatial encoding magnetic fields (SEMs) produced by gradient coils. In this work, the machine that is used uses rotating spatial encoding magnetic fields (rSEM) to encode the position information. The first published work to use the latter scanner, which is meant for clinical application, is given in [5]. They have constructed an MRI scanner based on rSEM and provided conceptual images that they claim could be further improved.

The signal model they used, as given in [5], using their notation, is described next. At a

given rotation,  $r$ , of the scanner, at time sample,  $n$ , the signal acquired by the coil,  $q$ , is given as-

$$s_{q,r}(n) = \sum_{\mathbf{x}} C_{q,r}(\mathbf{x}) e^{-i2\pi k(r,\mathbf{x},n)} m(\mathbf{x})$$

$$\Rightarrow s_{q,r}(n) = \sum_{\mathbf{x}} enc_{q,r}(\mathbf{x},n) m(\mathbf{x}) \quad \begin{array}{l} \text{(Grouping the exponential term} \\ \text{and coil sensitivity together)} \end{array} \quad (3.14)$$

Where,  $m(\mathbf{x})$  is the magnetization at location  $\mathbf{x}$ ,  $C_{q,r}$  is the coil sensitivity for coil  $q$  at rotation  $r$ ,  $k(r, \mathbf{x}, n)$  is the evolved phase from the non-linear gradient at rotation  $r$ .

In matrix notation, if  $\mathbf{S}_{q,r}$  is the measured signal matrix,  $\mathbf{E}_{q,r}$  is the encoding matrix and  $\mathbf{m}$  is the magnetization vector, then-

$$\mathbf{S}_{q,r} = \mathbf{E}_{q,r} \mathbf{m} \quad (3.15)$$

$\mathbf{E}_{q,r}$  is calculated by measuring the field map prior to imaging. The final encoding matrix  $\mathbf{E}$  is obtained by concatenating  $\mathbf{E}_{q,r}$  for each coil and each rotation.

The image is obtained by inverting the encoding matrix  $\mathbf{E}$  using iterative methods. Two methods are mentioned in the paper [5], which are, 1) Conjugate Gradient [19] 2) Algebraic Reconstruction Technique or Kaczmarz's method [22].

### 3.5. This Work

This work is also using an MRI machine that encodes the position information using rSEM. But unlike before, it uses a more complete signal model derived by solving the Bloch equation for the rotating machine. We will see, in the next chapter, that there exists an angular dependence of magnetization term with the stationary image. This is due to the choice of the frame of reference, and the signal model used here accounts for this. This study will investigate the parameters influencing this model with the objective of obtaining a satisfactory result. It will also examine Krylov subspace-based reconstruction algorithms that are available in the IRTools Package.



# 4

## Signal Model for rSEM

The signal model of the MRI machine that uses rSEM will be derived in this chapter.

### 4.1. Experimental Setup



Figure 4.1: a) Prototype of the rotating MRI machine. b) Phantom holder of the Rotating MRI.

Figure 4.1a shows the prototype of the rotating MRI machine along with the considered laboratory frame of reference. We can also see the RF amplifier behind, which is used to generate the RF pulses. On the right, figure 4.1b shows the holder of the phantom which goes inside the machine. Instead of rotating the field map of the machine, which would imply that we are rotating the Halbach cylinder, we are rotating the holder inside to investigate the machine. If we imagine the holder to be stationary, this would have the same effect as rotating the field map around it. This machine is for developing a proof of concept. In practice, the patient will be stationary, and the Halbach cylinder will rotate around the patients' head.

## 4.2. Coordinate System Considerations

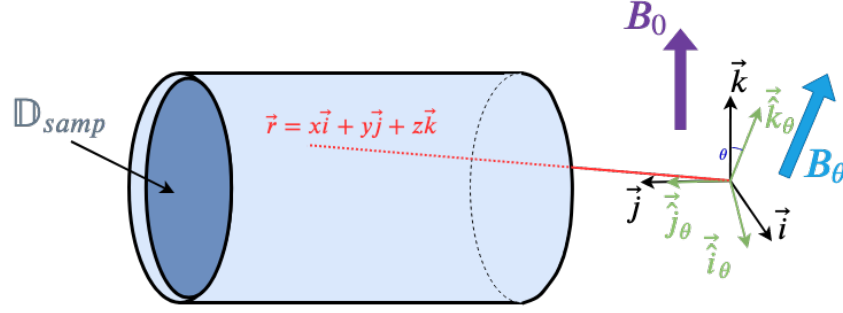


Figure 4.2: Schematic of the rotating MRI machine

Suppose, figure 4.2 represents the rotating MRI machine.  $\vec{i}$ ,  $\vec{j}$  and  $\vec{k}$  are the unit vectors corresponding to  $x$ ,  $y$  and  $z$  direction in the non-rotated frame, and  $\vec{i}_\theta$ ,  $\vec{j}_\theta$  and  $\vec{k}_\theta$  are the unit vectors corresponding to  $x_\theta$ ,  $y_\theta$  and  $z_\theta$  direction in the rotated frame. The rotated frame is making an angle  $\theta$  with the non-rotated frame.  $\vec{B}_0(\vec{r})$  is the external magnetic field along  $\vec{i}$  direction at position vector  $\vec{r} \in \mathbb{D}_{samp}$  when no rotation is applied.  $\vec{B}_\theta(\vec{r})$  is the rotated version of it when the machine is rotated.

There is a difference between the rotated frame considered here, and the rotating frame considered in chapter 2. In the latter, the frame is rotating with an angular frequency,  $\omega$ , while here, the frame is rotated by an angle  $\theta$ , and held stationary there for imaging at that angle.

The frame is rotated about the  $y$  axis. Its unit vectors are related to that of the non-rotated frame's as-

$$\begin{aligned}\vec{i}_\theta &= \cos(\theta)\vec{i} - \sin(\theta)\vec{k} \\ \vec{j}_\theta &= \vec{j} \\ \vec{k}_\theta &= \cos(\theta)\vec{i} + \sin(\theta)\vec{k}\end{aligned}\quad (4.1)$$

If  $B_0$  is the magnitude of the external field, then the rotated magnetic field is given by-

$$\vec{B}_\theta(x_\theta, y_\theta, z_\theta) = B_0[x \cos(\theta) - z \sin(\theta), y, x \cos(\theta) + z \sin(\theta)]\vec{i}_\theta \quad (4.2)$$

## 4.3. Reciprocity Theorem

From Chapter 2, equation 2.47, the voltage signal expression after using reciprocity theorem is-

$$V(t) = \frac{d}{dt} \int_{\vec{r} \in \mathbb{D}_{samp}} \vec{B}_r(\vec{r}) \cdot \vec{M}(\vec{r}, t) dr \quad \text{for } t \geq 0$$

Where  $\vec{B}_r(\vec{r})$  is the receive field and  $\vec{M}(\vec{r}, t)$  is the magnetization at position  $\vec{r}$ . We can obtain  $\vec{B}_r(\vec{r})$  by measuring the field map. Now, if we can calculate  $\vec{M}(\vec{r}, t)$  we can compute the signal  $V(t)$ . The strategy is to solve for it using the Bloch equation and plug it into the signal expression as shown above to get the signal.

## 4.4. Solving the Bloch Equation

From Chapter 2, equation 2.23, the Bloch Equation is given by-

$$\frac{d\vec{M}}{dt} = \gamma \vec{M} \times \vec{B} - \frac{\vec{M}_\perp}{T_2} - \frac{\vec{M}_\parallel - \vec{M}_{eq}}{T_1}$$

To see the functional dependence of the above equation clearly, we rewrite it as follows-

$$\begin{aligned} \frac{d\vec{\mathbf{M}}(\vec{\mathbf{r}}, t)}{dt} &= \gamma \vec{\mathbf{M}}(\vec{\mathbf{r}}, t) \times \vec{\mathbf{B}}(\vec{\mathbf{r}}) - \frac{\vec{\mathbf{M}}_{\perp}(\vec{\mathbf{r}}, t)}{T_2} - \frac{\vec{\mathbf{M}}_{\parallel}(\vec{\mathbf{r}}, t) - \vec{\mathbf{M}}_{eq}(\vec{\mathbf{r}})}{T_1} && \text{(Non-rotated frame)} \\ \frac{d\vec{\mathbf{M}}_{\theta}(\vec{\mathbf{r}}, t; \theta)}{dt} &= \gamma \vec{\mathbf{M}}_{\theta}(\vec{\mathbf{r}}, t; \theta) \times \vec{\mathbf{B}}_{\theta}(\vec{\mathbf{r}}; \theta) - \frac{\vec{\mathbf{M}}_{\perp, \theta}(\vec{\mathbf{r}}, t; \theta)}{T_2} - \frac{\vec{\mathbf{M}}_{\parallel, \theta}(\vec{\mathbf{r}}, t; \theta) - \vec{\mathbf{M}}_{eq, \theta}(\vec{\mathbf{r}}; \theta)}{T_1} && \text{(Rotated frame)} \end{aligned} \quad (4.3)$$

Let us take the magnetization in the non-rotated frame as  $\vec{\mathbf{M}}$  and the rotated frame as  $\vec{\mathbf{M}}_{\theta}$ .  $\vec{\mathbf{M}}_{\theta}$  can be expressed in terms of the unit vectors  $\vec{\mathbf{i}}_{\theta}$ ,  $\vec{\mathbf{j}}_{\theta}$  and  $\vec{\mathbf{k}}_{\theta}$  as-

$$\vec{\mathbf{M}}_{\theta}(\vec{\mathbf{r}}, t; \theta) = M_{\theta, x_{\theta}}(\vec{\mathbf{r}}, t; \theta) \vec{\mathbf{i}}_{\theta} + M_{\theta, y_{\theta}}(\vec{\mathbf{r}}, t; \theta) \vec{\mathbf{j}}_{\theta} + M_{\theta, z_{\theta}}(\vec{\mathbf{r}}, t; \theta) \vec{\mathbf{k}}_{\theta} \quad (4.4)$$

where,  $M_{\theta, x_{\theta}}(\vec{\mathbf{r}}, t; \theta)$ ,  $M_{\theta, y_{\theta}}(\vec{\mathbf{r}}, t; \theta)$  and  $M_{\theta, z_{\theta}}(\vec{\mathbf{r}}, t; \theta)$  are the components of  $\vec{\mathbf{M}}_{\theta}(\vec{\mathbf{r}}, t; \theta)$  along  $x_{\theta}$ ,  $y_{\theta}$  and  $z_{\theta}$  direction respectively.

Henceforth, for notational convenience, the functional dependencies are dropped. If we arrange the components  $M_{\theta, x_{\theta}}$ ,  $M_{\theta, y_{\theta}}$  and  $M_{\theta, z_{\theta}}$  in a  $3 \times 1$  vector,  $\vec{\mathbf{m}}_{\theta}$ , we get-

$$\vec{\mathbf{m}}_{\theta} = \begin{bmatrix} M_{\theta, x_{\theta}} \\ M_{\theta, y_{\theta}} \\ M_{\theta, z_{\theta}} \end{bmatrix} \quad (4.5)$$

We have the perpendicular component,  $\vec{\mathbf{M}}_{\perp, \theta} = M_{\theta, z_{\theta}} \vec{\mathbf{k}}_{\theta}$ , and the transverse component as,  $\vec{\mathbf{M}}_{\perp, \theta} = M_{\theta, x_{\theta}} \vec{\mathbf{i}}_{\theta} + M_{\theta, y_{\theta}} \vec{\mathbf{j}}_{\theta}$ . If we plug these expression into equation 4.3 (rotated frame), we get

$$\begin{aligned} \frac{d\vec{\mathbf{M}}_{\theta}}{dt} &= \gamma \vec{\mathbf{M}}_{\theta} \times \vec{\mathbf{B}}_{\theta} - \frac{\vec{\mathbf{M}}_{\perp, \theta}}{T_2} - \frac{\vec{\mathbf{M}}_{\parallel, \theta} - \vec{\mathbf{M}}_{eq, \theta}}{T_1} \\ \Rightarrow \begin{bmatrix} \frac{dM_{\theta, x_{\theta}}}{dt} \\ \frac{dM_{\theta, y_{\theta}}}{dt} \\ \frac{dM_{\theta, z_{\theta}}}{dt} \end{bmatrix} &= \begin{bmatrix} 0 & \gamma B_0 & 0 \\ -\gamma B_0 & 0 & 0 \\ 0 & 0 & 0 \end{bmatrix} \begin{bmatrix} M_{\theta, x_{\theta}} \\ M_{\theta, y_{\theta}} \\ M_{\theta, z_{\theta}} \end{bmatrix} - \begin{bmatrix} \frac{1}{T_2} & 0 & 0 \\ 0 & \frac{1}{T_2} & 0 \\ 0 & 0 & \frac{1}{T_1} \end{bmatrix} \begin{bmatrix} M_{\theta, x_{\theta}} \\ M_{\theta, y_{\theta}} \\ M_{\theta, z_{\theta}} \end{bmatrix} + \begin{bmatrix} 0 \\ 0 \\ \frac{M_{eq}}{T_1} \end{bmatrix} \\ \Rightarrow \frac{d\vec{\mathbf{m}}_{\theta}}{dt} + \mathbf{B} \vec{\mathbf{m}}_{\theta} &= \frac{M_{eq}}{T_1} \vec{\mathbf{e}}_3 \end{aligned} \quad (4.6)$$

where,

$$\vec{\mathbf{e}}_3 = \begin{bmatrix} 0 \\ 0 \\ 1 \end{bmatrix}, \quad \mathbf{B} = \begin{bmatrix} \frac{1}{T_2} & -\omega_0 & 0 \\ \omega_0 & \frac{1}{T_2} & 0 \\ 0 & 0 & \frac{1}{T_1} \end{bmatrix} \quad \text{and} \quad \omega_0 = \gamma B_0$$

If the initial condition of  $\vec{\mathbf{m}}_{\theta}$  at time  $t = 0^+$  (where '+' indicates the moment immediately after the application of the RF pulse) is  $\vec{\mathbf{m}}_{\theta}^{0+} = [M_{\theta, x_{\theta}}^{0+}, M_{\theta, y_{\theta}}^{0+}, M_{\theta, z_{\theta}}^{0+}]^T$ , then the solution of equation 4.6 is given by-

$$\vec{\mathbf{m}}_{\theta}(\vec{\mathbf{r}}, t; \theta) = M_{eq} [1 - e^{-\frac{t}{T_1}}] \vec{\mathbf{e}}_3 + e^{-\mathbf{B}t} \vec{\mathbf{m}}_{\theta}^{0+} \quad \text{for } t > 0 \quad (4.7)$$

## 4.5. Plugging into the signal expression

We also arrange the components of the receive field,  $\vec{\mathbf{b}}_{r, \theta}$ , in the rotating frame along  $x_{\theta}$ ,  $y_{\theta}$  and  $z_{\theta}$ .

$$\vec{\mathbf{b}}_{r, \theta} = \begin{bmatrix} B_{r, \theta, x_{\theta}} \\ B_{r, \theta, y_{\theta}} \\ B_{r, \theta, z_{\theta}} \end{bmatrix} \quad (4.8)$$

The voltage signal expression can be written as-

$$\begin{aligned}
V(t; \theta) &= \frac{d}{dt} \int_{\vec{r} \in \mathbb{D}_{\text{samp}}} \vec{\mathbf{B}}_{r,\theta}(\vec{r}; \theta) \cdot \vec{\mathbf{M}}_{\theta}(\vec{r}, t; \theta) dr \\
&= \frac{d}{dt} \int_{\vec{r} \in \mathbb{D}_{\text{samp}}} \vec{\mathbf{b}}_{r,\theta}^T \vec{\mathbf{m}}_{\theta} dr \\
&= \int_{\vec{r} \in \mathbb{D}_{\text{samp}}} \vec{\mathbf{b}}_{r,\theta}^T \frac{d\vec{\mathbf{m}}_{\theta}}{dt} dr
\end{aligned} \tag{4.9}$$

The last equality holds because  $\vec{\mathbf{b}}_{r,\theta}$  does not depend on  $t$  due to quasi-static approximation. Using equation 4.7,

$$\vec{\mathbf{b}}_{r,\theta}^T \frac{d\vec{\mathbf{m}}_{\theta}}{dt} = \frac{M_{eq}}{T_1} e^{\frac{-t}{T_1}} B_{r,\theta,z\theta} - \vec{\mathbf{b}}_{r,\theta}^T \mathbf{B} e^{-\mathbf{B}t} \vec{\mathbf{m}}_{\theta}^{0+} \tag{4.10}$$

To further carry out the analysis, we take the eigenvalue decomposition of the Bloch matrix,  $\mathbf{B}$ , as follows-

$$\mathbf{B}\mathbf{U} = \mathbf{U}\mathbf{\Lambda} \tag{4.11}$$

where,

$$\mathbf{\Lambda} = \begin{bmatrix} \lambda_1 & 0 & 0 \\ 0 & \lambda_2 & 0 \\ 0 & 0 & \lambda_3 \end{bmatrix} \quad \lambda_1 = \frac{1}{T_2 + i\omega_0} \quad \lambda_2 = \frac{1}{T_2 - i\omega_0} = \lambda_1^* \quad \text{and} \quad \lambda_3 = \frac{1}{T_1}$$

Also, orthonormalized eigenvector matrix,  $\mathbf{U}$ -

$$\mathbf{U} = [\vec{\mathbf{u}}_1 \quad \vec{\mathbf{u}}_2 \quad \vec{\mathbf{u}}_3] \quad \vec{\mathbf{u}}_1 = \frac{1}{\sqrt{2}} \begin{bmatrix} 1 \\ -i \\ 0 \end{bmatrix} \quad \vec{\mathbf{u}}_2 = \frac{1}{\sqrt{2}} \begin{bmatrix} 1 \\ i \\ 0 \end{bmatrix} = \vec{\mathbf{u}}_1^* \quad \vec{\mathbf{u}}_3 = \begin{bmatrix} 0 \\ 0 \\ 1 \end{bmatrix} = \vec{\mathbf{e}}_3 \tag{4.12}$$

and it satisfies -  $\mathbf{U}^H \mathbf{U} = \mathbf{U} \mathbf{U}^H = \mathbf{I}$ . So that-

$$\mathbf{B} = \mathbf{U}\mathbf{\Lambda}\mathbf{U}^H \tag{4.13}$$

Using equation 4.13, equation 4.10 becomes-

$$\begin{aligned}
\vec{\mathbf{b}}_{r,\theta}^T \frac{d\vec{\mathbf{m}}_{\theta}}{dt} &= \frac{M_{eq}}{T_1} e^{\frac{-t}{T_1}} B_{r,\theta,z\theta} - \vec{\mathbf{b}}_{r,\theta}^T \mathbf{B} e^{-\mathbf{B}t} \vec{\mathbf{m}}_{\theta}^{0+} \\
&= \frac{M_{eq}}{T_1} e^{\frac{-t}{T_1}} B_{r,\theta,z\theta} - \vec{\mathbf{b}}_{r,\theta}^T \mathbf{U}\mathbf{\Lambda}\mathbf{U}^H e^{-\mathbf{U}\mathbf{\Lambda}\mathbf{U}^H t} \vec{\mathbf{m}}_{\theta}^{0+} \\
&= \frac{M_{eq}}{T_1} e^{\frac{-t}{T_1}} B_{r,\theta,z\theta} - \vec{\mathbf{b}}_{r,\theta}^T \vec{\mathbf{u}}_1 \left( \frac{1}{T_2} + i\omega_0 \right) e^{-(\frac{1}{T_2} + i\omega_0)t} \vec{\mathbf{u}}_1^H \vec{\mathbf{m}}_{\theta}^{0+} \\
&\quad - \vec{\mathbf{b}}_{r,\theta}^T \vec{\mathbf{u}}_2 \left( \frac{1}{T_2} - i\omega_0 \right) e^{-(\frac{1}{T_2} - i\omega_0)t} \vec{\mathbf{u}}_2^H \vec{\mathbf{m}}_{\theta}^{0+} - \vec{\mathbf{b}}_{r,\theta}^T \vec{\mathbf{u}}_3 \frac{1}{T_1} e^{-\frac{t}{T_1}} \vec{\mathbf{u}}_3^H \vec{\mathbf{m}}_{\theta}^{0+} \\
&= \frac{1}{T_1} e^{\frac{-t}{T_1}} (M_{eq} - M_{\theta,z\theta}^{0+}) B_{r,\theta,z\theta} - \vec{\mathbf{b}}_{r,\theta}^T \vec{\mathbf{u}}_1 \left( \frac{1}{T_2} + i\omega_0 \right) e^{-\frac{t}{T_2}} e^{-i\omega_0 t} \vec{\mathbf{u}}_1^H \vec{\mathbf{m}}_{\theta}^{0+} \\
&\quad - \vec{\mathbf{b}}_{r,\theta}^T \vec{\mathbf{u}}_2 \left( \frac{1}{T_2} - i\omega_0 \right) e^{-\frac{t}{T_2}} e^{i\omega_0 t} \vec{\mathbf{u}}_2^H \vec{\mathbf{m}}_{\theta}^{0+}
\end{aligned} \tag{4.14}$$

We can ignore the first term of the right hand side of equation 4.14 because  $T_2(\vec{r}) < T_1(\vec{r})$ . Also, typically,  $\omega_0(\vec{r}; \theta) \gg \frac{1}{T_2(\vec{r})}$  for  $\vec{r} \in \mathbb{D}_{\text{samp}}$  and  $\theta \in [0, 2\pi)$ . Then, to a very good approximation, we have-

$$\vec{\mathbf{b}}_{r,\theta}^T \frac{d\vec{\mathbf{m}}_\theta}{dt} \approx i\vec{\mathbf{b}}_{r,\theta}^T \vec{\mathbf{u}}_2 \omega_0 e^{-\frac{t}{T_2}} e^{i\omega_0 t} \vec{\mathbf{u}}_2^H \vec{\mathbf{m}}_\theta^{0+} - i\vec{\mathbf{b}}_{r,\theta}^T \vec{\mathbf{u}}_1 \omega_0 e^{-\frac{t}{T_2}} e^{-i\omega_0 t} \vec{\mathbf{u}}_1^H \vec{\mathbf{m}}_\theta^{0+} \quad (4.15)$$

In order to make data processing convenient, the voltage signal,  $V(t; \theta)$ , is first modulated and then low-pass filtered. If the modulation frequency is  $\omega_{mod}$ , then the modulated signal,  $g(t; \theta)$ , is-

$$\begin{aligned} g(t; \theta) &= 2e^{i\omega_{mod}t} V(t; \theta) \\ &= \int_{\vec{\mathbf{r}} \in \mathbb{D}_{samp}} 2e^{i\omega_{mod}t} \vec{\mathbf{b}}_{r,\theta}^T \frac{d\vec{\mathbf{m}}_\theta}{dt} dr \\ &\approx \int_{\vec{\mathbf{r}} \in \mathbb{D}_{samp}} [2i\vec{\mathbf{b}}_{r,\theta}^T \vec{\mathbf{u}}_2 \omega_0 e^{-\frac{t}{T_2}} e^{i(\omega_0 + \omega_{mod})t} \vec{\mathbf{u}}_2^H \vec{\mathbf{m}}_\theta^{0+} - 2i\vec{\mathbf{b}}_{r,\theta}^T \vec{\mathbf{u}}_1 \omega_0 e^{-\frac{t}{T_2}} e^{-i(\omega_0 - \omega_{mod})t} \vec{\mathbf{u}}_1^H \vec{\mathbf{m}}_\theta^{0+}] dr \end{aligned} \quad (4.16)$$

We now low pass filter the modulated signal,  $g(t; \theta)$ , to filter out the frequency  $\omega_0 + \omega_{mod}$ . If we take  $\Delta\omega_0 = \omega_0 - \omega_{mod}$ , then we have-

$$d(t; \theta) = -2i \int_{\vec{\mathbf{r}} \in \mathbb{D}_{samp}} \vec{\mathbf{b}}_{r,\theta}^T \vec{\mathbf{u}}_1 \omega_0 e^{-\frac{t}{T_2}} e^{-i\Delta\omega_0 t} \vec{\mathbf{u}}_1^H \vec{\mathbf{m}}_\theta^{0+} dr \quad (4.17)$$

Using equation 4.12, we have-

$$\vec{\mathbf{b}}_{r,\theta}^T \vec{\mathbf{u}}_1 = \frac{1}{\sqrt{2}} B_{r,\theta-} \quad \text{and} \quad \vec{\mathbf{u}}_1^H \vec{\mathbf{m}}_\theta^{0+} = \frac{1}{\sqrt{2}} M_{\theta+}^{0+}$$

Where we have used the following complex notation for notational convenience

$$B_{r,\theta-} = B_{r,\theta,x_\theta} - iB_{r,\theta,y_\theta} \quad \text{and} \quad M_{\theta+}^{0+} = M_{\theta,x_\theta}^{0+} + iM_{\theta,y_\theta}^{0+}$$

Substituting the above expressions, equation 4.17 becomes-

$$d(t; \theta) = -i \int_{\vec{\mathbf{r}} \in \mathbb{D}_{samp}} M_{\theta+}(\vec{\mathbf{r}}; \theta) B_{r,\theta-}(\vec{\mathbf{r}}; \theta) \omega_0(\vec{\mathbf{r}}; \theta) e^{-\frac{t}{T_2}} e^{-i\Delta\omega_0(\vec{\mathbf{r}}; \theta)t} dr \quad (4.18)$$

## 4.6. Changing to non-rotated frame

In the non-rotated frame, the receive field and magnetization at  $t = 0$  respectively are given by-

$$\vec{\mathbf{B}}_r = B_{r,x} \vec{\mathbf{i}} + B_{r,y} \vec{\mathbf{j}} + B_{r,z} \vec{\mathbf{k}} \quad \text{and} \quad \vec{\mathbf{M}}^{0+} = M_x^{0+} \vec{\mathbf{i}} + M_y^{0+} \vec{\mathbf{j}} + M_z^{0+} \vec{\mathbf{k}}$$

Using 4.1,

$$\begin{aligned} B_{r,\theta,x_\theta} &= \vec{\mathbf{B}}_r \cdot \vec{\mathbf{i}}_\theta \\ &= (B_{r,x} \vec{\mathbf{i}} + B_{r,y} \vec{\mathbf{j}} + B_{r,z} \vec{\mathbf{k}}) \cdot \vec{\mathbf{i}}_\theta \\ &= \cos(\theta) B_{r,x} - \sin(\theta) B_{r,z} \end{aligned}$$

In the same way,

$$B_{r,\theta,y_\theta} = B_{r,y} \quad \text{and} \quad B_{r,\theta,z_\theta} = \sin(\theta) B_{r,x} + \cos(\theta) B_{r,z}$$

If we do the same thing with the initial magnetization,

$$M_{\theta,x_\theta}^{0+} = \cos(\theta) M_x^{0+} - \sin(\theta) M_z^{0+} \quad , \quad M_{\theta,y_\theta}^{0+} = M_y^{0+} \quad \text{and} \quad M_{\theta,z_\theta}^{0+} = \sin(\theta) M_x^{0+} + \cos(\theta) M_z^{0+}$$

Thus,

$$B_{r,\theta-} = B_{r,\theta,x_\theta} - iB_{r,\theta,y_\theta} = \cos(\theta) B_{r,x}(\vec{\mathbf{r}}) - \sin(\theta) B_{r,z}(\vec{\mathbf{r}}) - iB_{r,y}(\vec{\mathbf{r}}) = \mathcal{B}_-(\vec{\mathbf{r}}; \theta) \quad (4.19)$$

and,

$$M_{\theta+}^{0+} = M_{\theta,x\theta}^{0+} + iM_{\theta,y\theta}^{0+} = \cos(\theta)M_x^{0+} - \sin(\theta)M_z^{0+} + iM_y^{0+} \quad (4.20)$$

However, we would like the right hand side of equation 4.20 to be expressed in the form of  $\vec{\mathbf{M}}_{eq}$ . In chapter 2, equation 2.9, we have seen that the magnitude of the equilibrium magnetization,  $\vec{\mathbf{M}}_{eq}$ , is-

$$|\vec{\mathbf{M}}_{eq}| = \frac{\gamma^2 \hbar^2 B_0(\vec{\mathbf{r}}) N_S}{4KT_S}$$

The above is the magnitude of  $\vec{\mathbf{M}}_{eq}$  when the whole volume is considered. For a unit volume, we will use the local spin density,  $\rho(\vec{\mathbf{r}})$ . Then the magnitude becomes as follows-

$$|\vec{\mathbf{M}}_{eq}| = M_{eq} = \rho(\vec{\mathbf{r}}) \frac{\gamma^2 \hbar^2 B_0(\vec{\mathbf{r}})}{4KT_S}$$

If the external magnetic field  $\vec{\mathbf{B}}_0(\vec{\mathbf{r}})$  is applied along some unit vector  $\vec{\mathbf{s}}(\vec{\mathbf{r}})$  such that-

$$\vec{\mathbf{B}}_0(\vec{\mathbf{r}}) = B_0(\vec{\mathbf{r}}) \vec{\mathbf{s}}(\vec{\mathbf{r}})$$

Then  $\vec{\mathbf{M}}_{eq}$  is given by-

$$\vec{\mathbf{M}}_{eq} = \rho(\vec{\mathbf{r}}) \frac{\gamma^2 \hbar^2 B_0(\vec{\mathbf{r}})}{4KT_S} \vec{\mathbf{s}}(\vec{\mathbf{r}}) \quad (4.21)$$

We would like to image the spin density,  $\rho(\vec{\mathbf{r}})$ . To do this, an RF excitation is applied to flip the magnetization out of its equilibrium, as discussed in chapter 2 and then removed. The instant the excitation is removed is considered as time,  $t = 0^+$ . Magnetization at this instant is taken as-

$$\vec{\mathbf{M}}(\vec{\mathbf{r}}, 0^+) = \vec{\mathbf{M}}^{0+}(\vec{\mathbf{r}}) \quad \text{for} \quad \rho(\vec{\mathbf{r}}) \in \mathbb{D}_{samp} \quad (4.22)$$

This initial magnetization is proportional to the magnitude of the equilibrium magnetization. If we take the vector function  $\vec{\mathcal{M}}$ , independent of  $M_{eq}$ , as the constant of proportionality, we have-

$$\vec{\mathbf{M}}^{0+}(\vec{\mathbf{r}}) = \vec{\mathcal{M}}(\vec{\mathbf{r}}) M_{eq}(\vec{\mathbf{r}}) \quad \text{for} \quad \rho(\vec{\mathbf{r}}) \in \mathbb{D}_{samp} \quad (4.23)$$

Using the above expression, 4.24 becomes-

$$M_{\theta+}^{0+} = M_{eq}(\cos(\theta)\mathcal{M}_x^{0+}(\vec{\mathbf{r}}) - \sin(\theta)\mathcal{M}_z^{0+}(\vec{\mathbf{r}}) + i\mathcal{M}_y^{0+}(\vec{\mathbf{r}})) = \mathcal{M}_+^{0+}(\vec{\mathbf{r}}; \theta) \quad (4.24)$$

## 4.7. Expression for Signal Model

Using equation and 4.24, equation 4.18 becomes -

$$d(t; \theta) = \int_{\mathbf{r} \in \mathbb{D}_{samp}} \rho(\vec{\mathbf{r}}) \mathcal{K}(\vec{\mathbf{r}}; \theta) e^{-p(\vec{\mathbf{r}}; \theta)t} d\mathbf{r} \quad (4.25)$$

where,

$$\mathcal{K}(\vec{\mathbf{r}}; \theta) = -i \frac{\gamma \hbar^2}{4KT_S} \mathcal{M}_+^{0+}(\vec{\mathbf{r}}; \theta) \mathcal{B}_-(\vec{\mathbf{r}}; \theta) \omega_0^2 \quad \text{and} \quad p(\vec{\mathbf{r}}; \theta) = \frac{1}{T_2} + i\Delta\omega_0 \quad (4.26)$$

This is the signal model this work will be using. Similar to the approach in chapter 3, after taking the discrete version of the above equation, we arrive at the following equation-

$$d(k_m, \theta_r) = \sum_n \rho(r_n) \mathcal{K}(r_n; \theta_r) e^{-p(r_n; \theta_r) k_m \Delta r} \quad (4.27)$$

Writing this equation as a matrix by stacking different  $\theta_r$ , we have-

$$\begin{aligned} \begin{bmatrix} d(k_1, \theta_1) \\ d(k_2, \theta_1) \\ \vdots \\ d(k_M, \theta_1) \\ d(k_1, \theta_2) \\ \vdots \\ d(k_M, \theta_2) \\ \vdots \\ d(k_M, \theta_R) \end{bmatrix} &= \begin{bmatrix} \mathcal{K}(r_1; \theta_1)e^{-p(r_2; \theta_1)k_1} & \mathcal{K}(r_2; \theta_1)e^{-p(r_2; \theta_1)k_1} & \dots & \mathcal{K}(r_N; \theta_1)e^{-p(r_N; \theta_1)k_1} \\ \mathcal{K}(r_1; \theta_1)e^{-p(r_2; \theta_1)k_2} & \mathcal{K}(r_2; \theta_1)e^{-p(r_2; \theta_1)k_2} & \dots & \mathcal{K}(r_N; \theta_1)e^{-p(r_N; \theta_1)k_2} \\ \vdots & \vdots & \dots & \vdots \\ \mathcal{K}(r_1; \theta_1)e^{-p(r_2; \theta_1)k_M} & \mathcal{K}(r_2; \theta_1)e^{-p(r_2; \theta_1)k_M} & \dots & \mathcal{K}(r_N; \theta_1)e^{-p(r_N; \theta_1)k_M} \\ \mathcal{K}(r_1; \theta_2)e^{-p(r_2; \theta_2)k_1} & \mathcal{K}(r_2; \theta_2)e^{-p(r_2; \theta_2)k_1} & \dots & \mathcal{K}(r_N; \theta_2)e^{-p(r_N; \theta_2)k_1} \\ \vdots & \vdots & \dots & \vdots \\ \mathcal{K}(r_1; \theta_2)e^{-p(r_2; \theta_2)k_M} & \mathcal{K}(r_2; \theta_2)e^{-p(r_2; \theta_2)k_M} & \dots & \mathcal{K}(r_N; \theta_2)e^{-p(r_N; \theta_2)k_M} \\ \vdots & \vdots & \dots & \vdots \\ \mathcal{K}(r_1; \theta_R)e^{-p(r_2; \theta_R)k_M} & \mathcal{K}(r_2; \theta_R)e^{-p(r_2; \theta_R)k_M} & \dots & \mathcal{K}(r_N; \theta_R)e^{-p(r_N; \theta_R)k_M} \end{bmatrix} \begin{bmatrix} \rho(r_1) \\ \rho(r_2) \\ \vdots \\ \rho(r_N) \end{bmatrix} \\ \Rightarrow \mathbf{d} &= \mathbf{E} \boldsymbol{\rho} \end{aligned} \quad (4.28)$$

where  $\mathbf{E} \in \mathbb{C}^{MR \times N}$ ,  $\mathbf{d} \in \mathbb{C}^{MR \times 1}$  and  $\boldsymbol{\rho} \in \mathbb{C}^{N \times 1}$ .  $\Delta r$  is ignored because it is a scalar.

This chapter is wrapped up in the next section, which discusses the k-space considerations of the signal model thus derived.

## 4.8. K-space consideration

The profile of the measured z-component of the magnetic field density, in the  $y = 0$  plane of the Halbach setup, is illustrated in figure 4.3

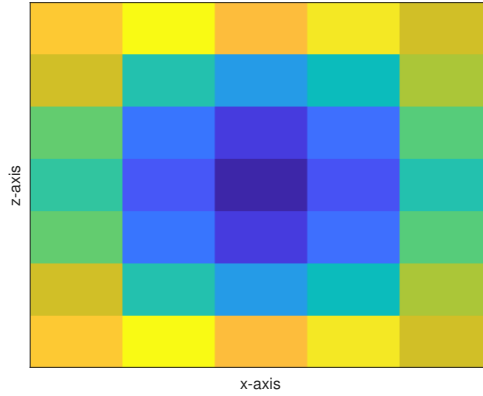


Figure 4.3: Measured z-component of B0 Profile of the Halbach setup. The colour scale is in Tesla.

The profile roughly looks like a quadratic field profile and can be given the form-

$$B_0(x, z) = B_0^c + g_x x^2 + g_z z^2 \quad (4.29)$$

where,  $B_0^c$  is the field value at the centre of the cylinder, and  $g_x$  and  $g_z$  are constants. But this work will assume the profile to be to linear (equation 4.30) to make the analysis easier, and to establish a link between the spatial and frequency space (k-space) for this MRI machine. More rigorous analysis of a quadratic  $B_0$  profile [6][18] can be done in a future work. So we have-

$$B_0(x, 0, z) = B_0^c + G_x x + G_z z \quad , \text{ where } G_x \text{ and } G_z \text{ are some constants.} \quad (4.30)$$

For our rotating setup, if we rotate this field, we get-

$$B_0(x, 0, z) = B_0^c + G_x [x \cos(\theta) - z \sin(\theta)] + G_z [x \sin(\theta) + z \cos(\theta)] \quad (4.31)$$

Taking,  $\omega_{mod} = \gamma B_0^c$ , equation 4.34 becomes-

$$\begin{aligned}\Delta\omega_0 t &= \gamma[G_x \cos(\theta) + G_z \sin(\theta)]t x + \gamma[-G_x \sin(\theta) + G_z \cos(\theta)]t z \\ &= k'_x x + k'_z z\end{aligned}\quad (4.32)$$

where we have substituted  $k'_x = \gamma[G_x \cos(\theta) + G_z \sin(\theta)]t$  and  $k'_z = \gamma[-G_x \sin(\theta) + G_z \cos(\theta)]t$ <sup>1</sup>. Now,

$$e^{-i\Delta\omega_0 t} = e^{-ik'_x x - ik'_z z} \quad (4.33)$$

which is the exponent part of a 2D Fourier transform. We can also observe that-

$$k'_x(t; \theta)^2 + k'_z(t; \theta)^2 = (\gamma t)^2 (G_x^2 + G_z^2) \quad (4.34)$$

is an equation of a circle centered at the origin, and it has a radius of  $\gamma t \sqrt{G_x^2 + G_z^2}$ . There are two points we have to note-

1. If  $t$  is fixed and  $\theta$  is varied from  $0$  to  $2\pi$ , the vector  $\vec{k}'(t; \theta) = k'_x(t; \theta)\vec{i}_\theta + k'_z(t; \theta)\vec{j}_\theta$  traces out a circle with radius  $\gamma t \sqrt{G_x^2 + G_z^2}$ .
2. If  $\theta$  is fixed and  $t$  is varied from  $t = 0$  to  $t = T_{max}$ ,  $\vec{k}'$  traces out a line starting from the origin and ending at  $\vec{k}'(T_{max}; \theta)$ .

These cases are illustrated in figure 4.4-

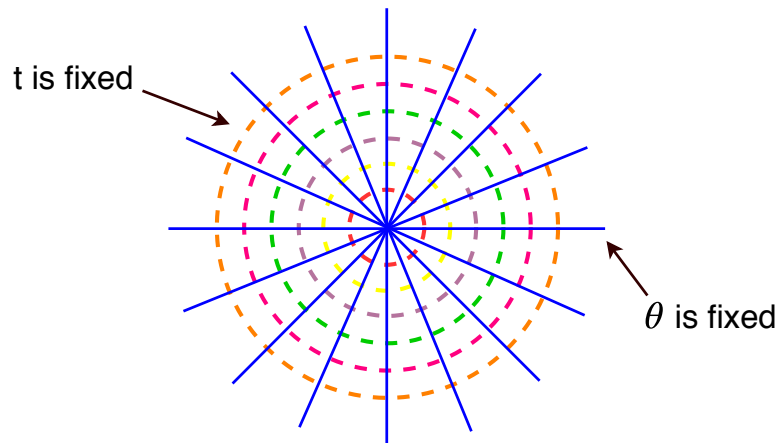


Figure 4.4: K space trajectories for 1) fixed  $t$  and  $\theta$  varying 2) fixed  $\theta$  and  $t$  varying.

<sup>1</sup> $k'$  (k prime) is used to indicate k-space frequencies to differentiate it from  $k_m$  which is a discrete time instant

## Part 2: Signal Reconstruction



# 5

## Problem Description

The signal model of the MRI machine that uses rSEM was obtained in the previous chapter (chapter 4). This model is used to formulate a mathematical problem that is intended to be solved by reconstruction algorithms.

This chapter begins by expressing the process of image reconstruction as a mathematical problem. After that, regularization is described, where additional information is provided by including an extra term to the original formulation. This is done so that a better solution is obtained. This chapter explains the techniques adopted by this work to choose this term.

### 5.1. Problem Formulation

We recall equation 4.28. Here, we have changed the notation and replaced  $\mathbf{d}$  as  $\mathbf{b}$ ,  $\mathbf{E}$  as  $\mathbf{A}$ , and  $\boldsymbol{\rho}$  as  $\mathbf{x}$ . Thus we have the following system of linear equations-

$$\mathbf{b} = \mathbf{A}\mathbf{x} \quad (5.1)$$

But unlike in equation 4.28, for simplicity, we consider  $\mathbf{A} \in \mathbb{C}^{m \times n}$ ,  $\mathbf{b} \in \mathbb{C}^{m \times 1}$  and  $\mathbf{x} \in \mathbb{C}^{n \times 1}$ . To reconstruct  $\mathbf{x}$ , we just solve the above system. But in our case,  $\mathbf{A}$  is a tall matrix and we have an overdertermined system. Usually, a unique solution for overdertermined system does not exist and we instead find the best approximate  $\mathbf{x}$  in a 2-norm sense by solving the following optimization problem-

$$\underset{\mathbf{x}}{\text{minimize}} \quad \|\mathbf{A}\mathbf{x} - \mathbf{b}\|_2^2 \quad (5.2)$$

### 5.2. Regularization

The problem formulation of equation 5.2 satisfies the existence and uniqueness requirements of Hadamard's conditions[11]. But this formulation is not immune to noise. If matrix  $\mathbf{A}$  is ill-conditioned, a small perturbation in  $\mathbf{A}$  or  $\mathbf{b}$  may lead to a large perturbation of the solution. To stabilize or regularize it, we reformulate the problem as-

$$\underset{\mathbf{x}}{\text{minimize}} \quad \|\mathbf{A}\mathbf{x} - \mathbf{b}\|_2^2 + \lambda \|\mathbf{L}\mathbf{x}\|_p^p \quad (5.3)$$

where  $\lambda$  is a scalar called regularization parameter, and  $\mathbf{L}$  is the called the regularization matrix.  $\lambda$  and  $\mathbf{L}$  will be described more in the subsequent sections. The p-norm on the regularization term indicates that it is a p-norm regularized problem.

If the problem is a 2-norm regularized problem it is widely known as the Tikhonov problem.

$$\underset{\mathbf{x}}{\text{minimize}} \quad \|\mathbf{A}\mathbf{x} - \mathbf{b}\|_2^2 + \lambda \|\mathbf{L}\mathbf{x}\|_2^2 \quad (5.4)$$

One advantage of this Tikhonov formulation is that it can be easily written in a more compact least squares form as follows-

$$\underset{\mathbf{x}}{\text{minimize}} \quad \left\| \begin{pmatrix} \mathbf{A} \\ \sqrt{\lambda} \mathbf{L} \end{pmatrix} \mathbf{x} - \begin{pmatrix} \mathbf{b} \\ 0 \end{pmatrix} \right\|_2^2 \quad (5.5)$$

This form is easier to be solved by the reconstruction algorithms.

### 5.3. Choosing the Regularization Parameter

To get an insight on how to choose the regularization parameter,  $\lambda$ , we consider the Tikhonov problem in equation 5.4. (The description given in this section is based on the text given in [11])

$$\underset{\mathbf{x}}{\text{argmin}} \quad \|\mathbf{Ax} - \mathbf{b}\|_2^2 + \lambda \|\mathbf{Lx}\|_2^2 = \mathbf{x}_\lambda$$

Let us say, after solving this problem, we get our solution to be  $\mathbf{x}_\lambda$ . There are two norms that are of interest to us-

1. **Solution Norm:** It tells us about the size of the solution and is given by  $\|\mathbf{x}\|_2$
2. **Residual Norm:** It tells us about the size of the error between the measured value,  $\mathbf{b}$ , and the computed value,  $\mathbf{Ax}_\lambda$ , and is given by  $\|\mathbf{Ax}_\lambda - \mathbf{b}\|_2$

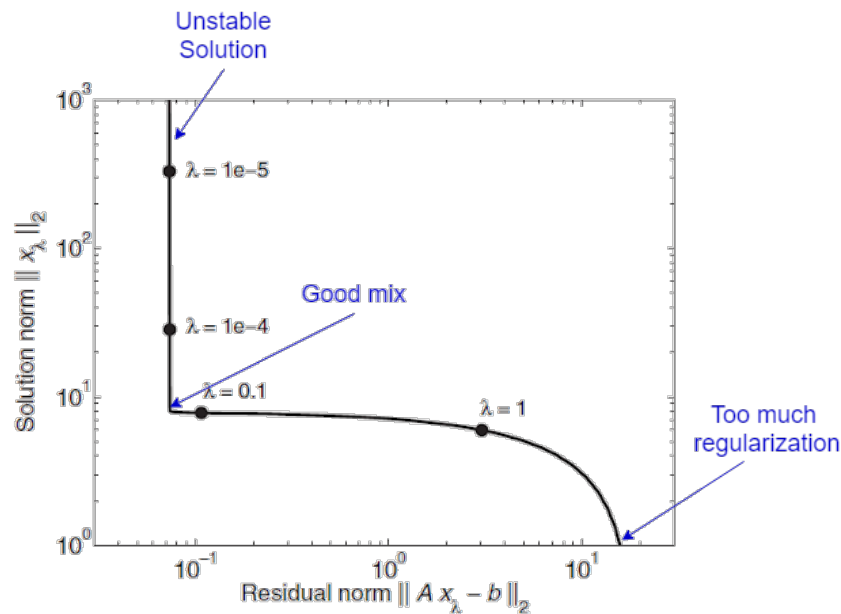


Figure 5.1: L-curve of  $\mathbf{x}_\lambda$ . Figure is adapted from [11].

Suppose, figure 5.1 illustrates the graph between  $\|\mathbf{x}\|_2$  and  $\|\mathbf{Ax}_\lambda - \mathbf{b}\|_2$  as a function of  $\lambda$ . This graph is called L-curve. If we choose a low value of  $\lambda$ , the residual norm,  $\|\mathbf{Ax}_\lambda - \mathbf{b}\|_2$ , is seen to decrease but the solution norm,  $\|\mathbf{x}\|_2$ , blows up, which means that the solution is unstable. This is not desired. On the other hand, if we choose a very high value of  $\lambda$  then  $\|\mathbf{Ax}_\lambda - \mathbf{b}\|_2$  increases and  $\|\mathbf{x}\|_2$  approaches 0. A solution having  $\|\mathbf{x}\|_2 = 0$  is meaningless and is again not desired. What is desired is both  $\|\mathbf{x}\|_2$  and  $\|\mathbf{Ax}_\lambda - \mathbf{b}\|_2$  are simultaneously as small as possible. And this happens at the elbow of the curve shown above, which is considered as having a good mix of  $\|\mathbf{x}\|_2$  and  $\|\mathbf{Ax}_\lambda - \mathbf{b}\|_2$ . So,  $\lambda$  in that respect, tells us how much weight is given to the regularization term.

An important part of this work is to investigate algorithms that choose the  $\lambda$  parameter in an automated fashion. There are different algorithms to do this, but so far, a general-purpose efficient parameter-choice algorithm is yet to be found[11].

This work uses a MATLAB toolbox called "IR Tools" which contains a package of iterative regularization methods. More will be discussed about it in the next chapter. Two approaches to choose  $\lambda$  parameter, which is implemented in this toolbox are-

1. Discrepancy principle
2. Generalized cross validation

### 5.3.1. Discrepancy Principle

An iterative solver finds a solution,  $\mathbf{x}^{(k)}$ , in an iterative manner and updates it at every iteration,  $k$ , with an objective to find the best one. As the solution updates, the residual,  $\mathbf{Ax}^{(k)} - \mathbf{b}$ , also updates. The idea behind discrepancy principle is to ask the user for an error estimate,  $\epsilon$ , and the moment the residual norm becomes smaller than this estimate, the iteration of the solving algorithm is stopped. Thus discrepancy principle can be described as-

$$\text{Choose } \lambda \text{ such that } \|\mathbf{Ax}_\lambda^{(k)} - \mathbf{b}\|_2 \geq \eta\epsilon \quad (5.6)$$

where,  $\mathbf{x}_\lambda^{(k)}$  is the  $k^{\text{th}}$  iterand corresponding to the chosen  $\lambda$ .  $\eta$  is called the safety factor. It is there to ensure that the solution norm does not blow up. The default value of  $\eta$  in IR tools is 1.01. The implementation of discrepancy principle will be discussed more in the next chapter.

### 5.3.2. Generalized cross validation

Generalized cross validation (GCV) is a statistical approach to compute the appropriate  $\lambda$  parameter automatically. To get an idea about it we consider the following-

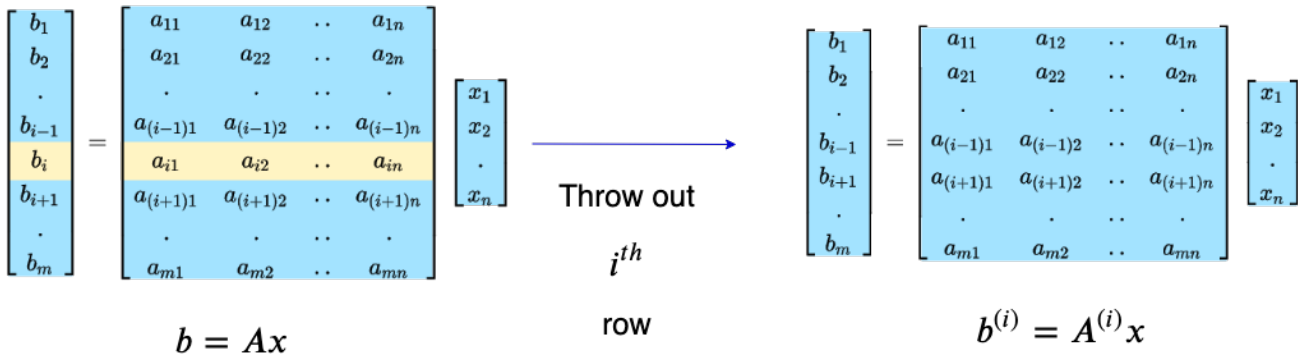


Figure 5.2: Generalized cross validation

Suppose, we obtain the system of equation " $\mathbf{b}^{(i)} = \mathbf{A}^{(i)}\mathbf{x}$ " by throwing out the  $i^{\text{th}}$  row from the system of equations " $\mathbf{b} = \mathbf{Ax}$ " (figure 5.2). The Tikhonov problem solution for the former system is given by-

$$\mathbf{x}_\lambda^{(i)} = ((\mathbf{A}^{(i)})^T \mathbf{A}^{(i)} + \lambda \mathbf{I}_{n-1})^{-1} (\mathbf{A}^{(i)})^T \mathbf{b}^{(i)} \quad (5.7)$$

Now, according to GCV,  $\mathbf{A}(i, :)\mathbf{x}_\lambda$  should be equal to  $\mathbf{b}^{(i)}$ . Here,  $\mathbf{A}(i, :)$  and  $\mathbf{b}^{(i)}$  are the  $i^{\text{th}}$  row of  $\mathbf{A}$  and  $\mathbf{b}$ , respectively, that was thrown away. For each row of  $\mathbf{A}$ , this boils down to solving the following optimization problem-

$$\text{minimize}_\lambda \frac{1}{m} \sum_{i=1}^m (\mathbf{A}(i, :)\mathbf{x}_\lambda - \mathbf{b}^{(i)})^2 \quad (5.8)$$

The above optimization problem is equivalent to solving  $m$  Tikhonov problems. This becomes computationally intensive if the size of matrix  $\mathbf{A}$  is very large. There is an alternative formulation of this problem which is comparatively more tractable[11].

$$\underset{\lambda}{\text{minimize}} \quad GCV(\lambda) = \underset{\lambda}{\text{minimize}} \quad \frac{n\|(\mathbf{I} - \mathbf{A}\mathbf{A}_\lambda^\dagger)\mathbf{b}\|_2^2}{(\text{trace}(\mathbf{I} - \mathbf{A}\mathbf{A}_\lambda^\dagger))^2} \quad (5.9)$$

where  $\mathbf{A}_\lambda = (\mathbf{A}^T\mathbf{A} + \lambda\mathbf{I})^{-1}\mathbf{A}^T$ , and  $\mathbf{A}_\lambda^\dagger$  is the Moore Penrose inverse of  $\mathbf{A}_\lambda$ . Here, SVD of  $\mathbf{A}_\lambda$  is used to compute the solution. But, this problem is still time consuming to solve as computing the SVD of very large matrices can take prohibitively long time. Some time can be saved if we decompose  $\mathbf{A}_\lambda$  into a much smaller bi-diagonal matrix,  $\mathbf{B}_{\lambda,k}$ , and use it in place of  $\mathbf{A}_\lambda$  to compute the solution. More about this decomposition process is discussed in the next chapter. Further, in addition to GCV, the IR Tools also implements Weighted-GCV (WGCV). Here, apart from completely leaving out the  $i^{th}$  row of  $\mathbf{A}$  and  $\mathbf{b}$ , the idea is carry forward to partially leaving out the  $i^{th}$  row which is indicated by a weight parameter  $\omega$ . The value of this  $\omega$  varies from 0 to 1. 1 means that the  $i^{th}$  row is completely left out and the algorithm is equivalent to GCV. 0 means that the  $i^{th}$  row is not removed. The weights can also be chosen in an adaptive manner[4]. In WGCV, the following optimization problem is solved[4].

$$\underset{\lambda}{\text{minimize}} \quad WGCV(\lambda) = \underset{\lambda}{\text{minimize}} \quad \frac{n\|(\mathbf{I} - \omega\mathbf{A}\mathbf{A}_\lambda^\dagger)\mathbf{b}\|_2^2}{(\text{trace}(\mathbf{I} - \omega\mathbf{A}\mathbf{A}_\lambda^\dagger))^2} \quad (5.10)$$

## 5.4. Choosing the Regularization Matrix

The regularization matrix,  $\mathbf{L}$ , tells how the regularization term depends on  $\mathbf{x}$ . It adds more information to the problem so that a better solution is obtained. In image reconstruction, it is desired that the values of adjacent pixels do not change much, except at the edges and interfaces. So in our case, one of the ways to minimize the jumps of the pixel values is by choosing  $\mathbf{L}$  to be the Laplacian matrix. More description of the choice of this  $\mathbf{L}$  will be provided in the next chapter.

# 6

## Algorithms

At this point, it is believed to be beneficial to have a clear picture of what we are doing. Figure 6.1 attempts to describe this.

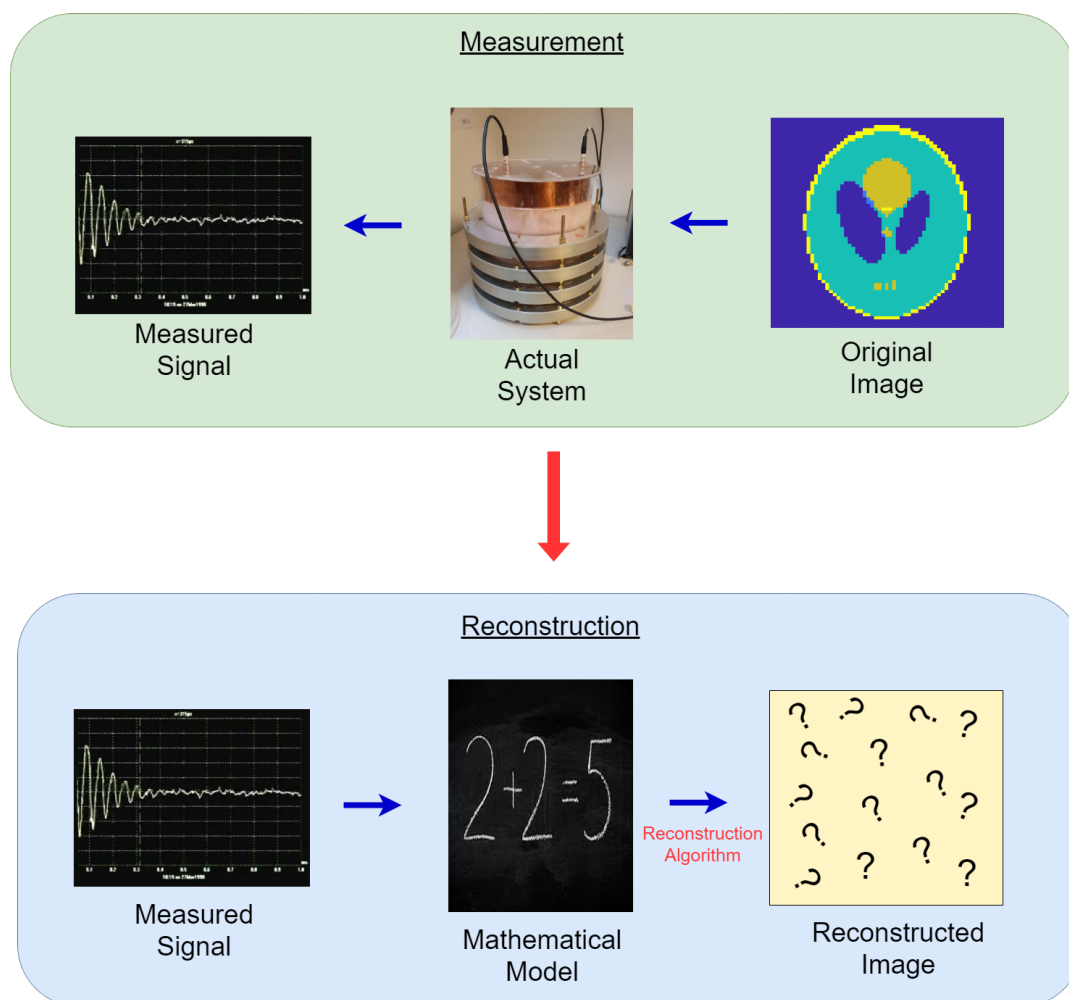


Figure 6.1: Measurement and reconstruction

We start with the original object that we want to image (shown on the top part of the figure 6.1). In a realistic setting, this is the functional or anatomical information in a patient that we want to image non-invasively. We use the rotating MRI machine, which is our actual system,

to image it and obtain the measured signals. Next, now that we have the measured signal, we would want to use it to reconstruct back the image of the object (shown on the bottom part of the figure 6.1). For the computation of this, we swap an equivalent mathematical model with the actual system and use appropriate reconstruction algorithms.

This chapter first aspires to give some mathematical background before delving into the algorithms used. More notably it attempts to give some degree of idea pertaining to Krylov subspace methods. After this brief background, this chapter describes the algorithms used in this work.

## 6.1. Iterative algorithms

Let us revisit the the Tikhonov's regularization problem (equation 5.5) from the previous chapter-

$$\underset{\mathbf{x}}{\text{minimize}} \quad \left\| \begin{pmatrix} \mathbf{A} \\ \sqrt{\lambda} \mathbf{L} \end{pmatrix} \mathbf{x} - \begin{pmatrix} \mathbf{b} \\ 0 \end{pmatrix} \right\|_2^2$$

For convenience, let us consider  $\begin{pmatrix} \mathbf{A} \\ \sqrt{\lambda} \mathbf{L} \end{pmatrix}$  as  $\tilde{\mathbf{A}}$  and  $\begin{pmatrix} \mathbf{b} \\ 0 \end{pmatrix}$  as  $\tilde{\mathbf{b}}$  in this section. Thus we have-

$$\underset{\mathbf{x}}{\text{minimize}} \quad \|\tilde{\mathbf{A}}\mathbf{x} - \tilde{\mathbf{b}}\|_2^2 \quad (6.1)$$

In the above problem formulation, our objective function is  $f(\mathbf{x}) = \|\tilde{\mathbf{A}}\mathbf{x} - \tilde{\mathbf{b}}\|_2^2$ . If  $\tilde{\mathbf{A}}$  is positive definite, one can find its minimum solution,  $\mathbf{x}_{min}$ , by setting the gradient of the objection function,  $f'(\mathbf{x})$ , to 0. Then we get-

$$\begin{aligned} f'(\mathbf{x}_{min}) &= 0 \\ \Rightarrow 2\tilde{\mathbf{A}}^T \tilde{\mathbf{A}}\mathbf{x}_{min} - 2\tilde{\mathbf{A}}^T \tilde{\mathbf{b}} &= 0 \\ \Rightarrow \mathbf{x}_{min} &= (\tilde{\mathbf{A}}^T \tilde{\mathbf{A}})^{-1} \tilde{\mathbf{A}}^T \tilde{\mathbf{b}} \end{aligned} \quad (6.2)$$

If the size of  $\tilde{\mathbf{A}}$  is very large, then the computation of  $\mathbf{x}_{min}$  becomes prohibitively expensive. In this situation, iterative algorithms are useful. These kind of algorithms generate a sequence of approximate solutions where the  $k^{th}$  estimate is derived from the  $(k-1)^{th}$  estimate. The objective of these algorithms is to produce progressively better approximations of the solution that converges to the true solution with a desired precision as the iterations goes by. Mathematically[24], sequence of iterands are denoted as-

$$\{\mathbf{x}^{(k)}\}_{k \geq 0}, \text{ where } \mathbf{x}^{(k)} \rightarrow \mathbf{x}_{min} \text{ for } k \rightarrow \infty \quad (6.3)$$

The general equation defining how new updates are obtained is given by-

$$\mathbf{x}^{(k+1)} = \mathbf{x}^{(k)} + \alpha^{(k)} \mathbf{d}^{(k)} \quad (6.4)$$

Where  $\mathbf{d}^{(k)}$  is the search vector in the  $k^{th}$  iteration.  $\alpha^{(k)}$  is a scalar called step size. It tells how big a step should be taken in the direction of  $\mathbf{d}^{(k)}$ . A way to obtain  $\alpha^{(k)}$  is by doing a line search[20].

## 6.2. Geometric Interpretation of Krylov Subspace Methods

The problem which we wish to solve is-

$$\underset{\mathbf{x}}{\text{minimize}} \quad \|\mathbf{A}\mathbf{x} - \mathbf{b}\|_2^2 = \underset{\mathbf{x}}{\text{minimize}} \quad f(\mathbf{x}) \quad (6.5)$$

To visualize  $f(\mathbf{x})$ , we consider the 2D case where  $\mathbf{x} = \begin{bmatrix} x_1 \\ x_2 \end{bmatrix}$ . If  $\mathbf{A}$  is symmetric and positive definite, then figure 6.2a illustrates  $f(\mathbf{x})$ . Figure 6.2b shows the contour plot of figure 6.2a. This will be used to explain the workings of the algorithms to be followed to reach the minimum solution point.

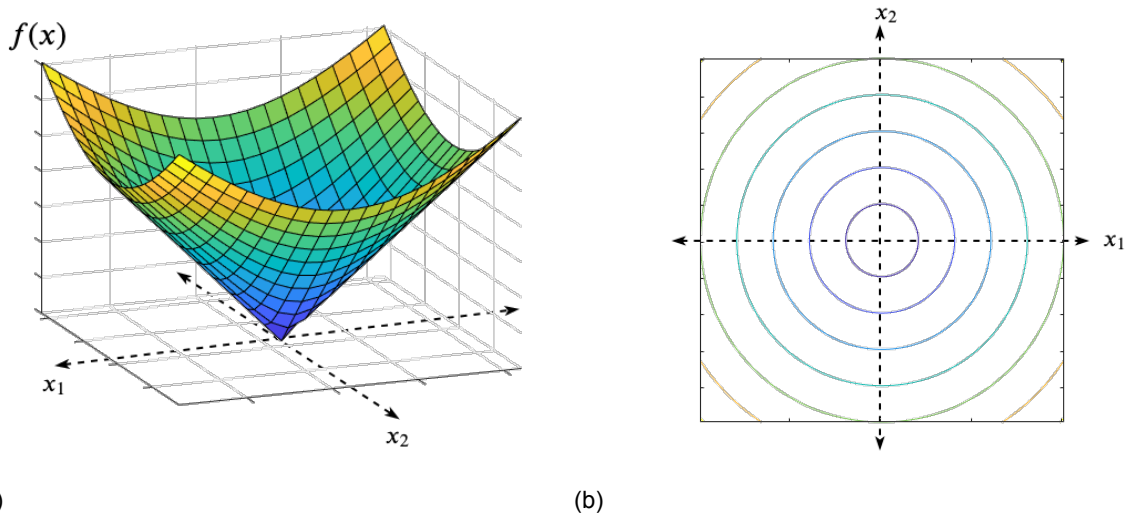


Figure 6.2: a) Illustration of  $f(\mathbf{x})$  for 2D case b) Coutour lines of  $f(\mathbf{x})$

In this section, the goal is to present some geometrical intuition behind the workings of Krylov subspace methods rather than going too much into the mathematical details. If one wishes to go through the mathematical equations, appropriate materials will be cited throughout this section. Here, we will start with a simple idea, and progressively build upon it to arrive at the intuition behind Krylov subspace methods.

### 6.2.1. Steepest Descent

Steepest descent is an iterative algorithm which tries to arrive at the solution  $\mathbf{x}_{min}$  by taking steps that are proportional to the direction of the negative gradient of  $f(\mathbf{x})$  at each iterations[20]. In other words,  $\mathbf{d}^{(k)} = -f'(\mathbf{x}^{(k)})$ -

$$\mathbf{x}^{(k+1)} = \mathbf{x}^{(k)} - \alpha^{(k)} f'(\mathbf{x}^{(k)}) \tag{6.6}$$

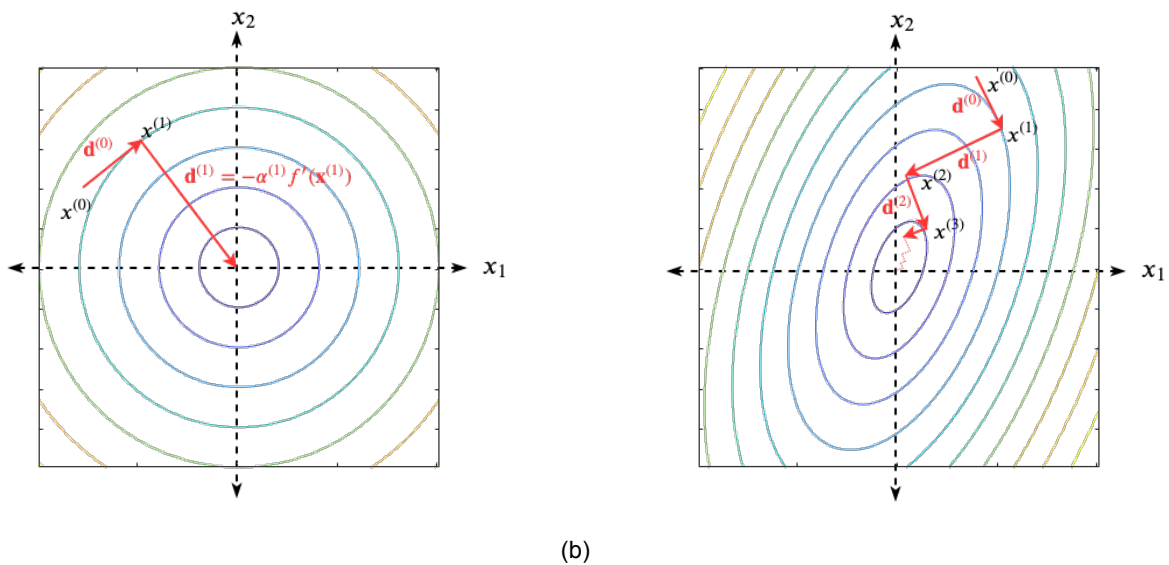


Figure 6.3: Steepest descent when contour lines are a) circular b) ellipsoids

Steepest descent is initialized with some initial guess  $\mathbf{x}^{(0)}$ , and search vector  $\mathbf{d}^{(0)}$ . When the contour lines are concentric circles, the negative gradient of  $f(\mathbf{x}^{(k)})$  at any point points directly towards the solution. Therefore the solution is obtained within the next iteration itself

(figure 6.3a). However, if the contour lines are ellipsoids, and the initial guess vector does not lie along one of the eigenvectors of  $\mathbf{A}$ , then the number of iterations needed to converge increases[20] (figure 6.3b).

### 6.2.2. Conjugate Direction

The Conjugate direction method attempts to find the the directions  $\mathbf{d}^{(k)}$  such that the directions are A-conjugate. This is equivalent to saying-

$$\mathbf{d}^{(j)} \mathbf{A} \mathbf{d}^{(k)} = 0, \quad j \neq k \quad (6.7)$$

Geometrically speaking, it turns out that this algorithm finds  $\mathbf{d}^{(k)}$ s in such a way that the  $\mathbf{d}^{(k)}$ s on ellipsoid contour lines (figure 6.4a ) become orthogonal to each other when this ellipsoid contour lines are stretched or transformed to circular contour lines (figure 6.4b).

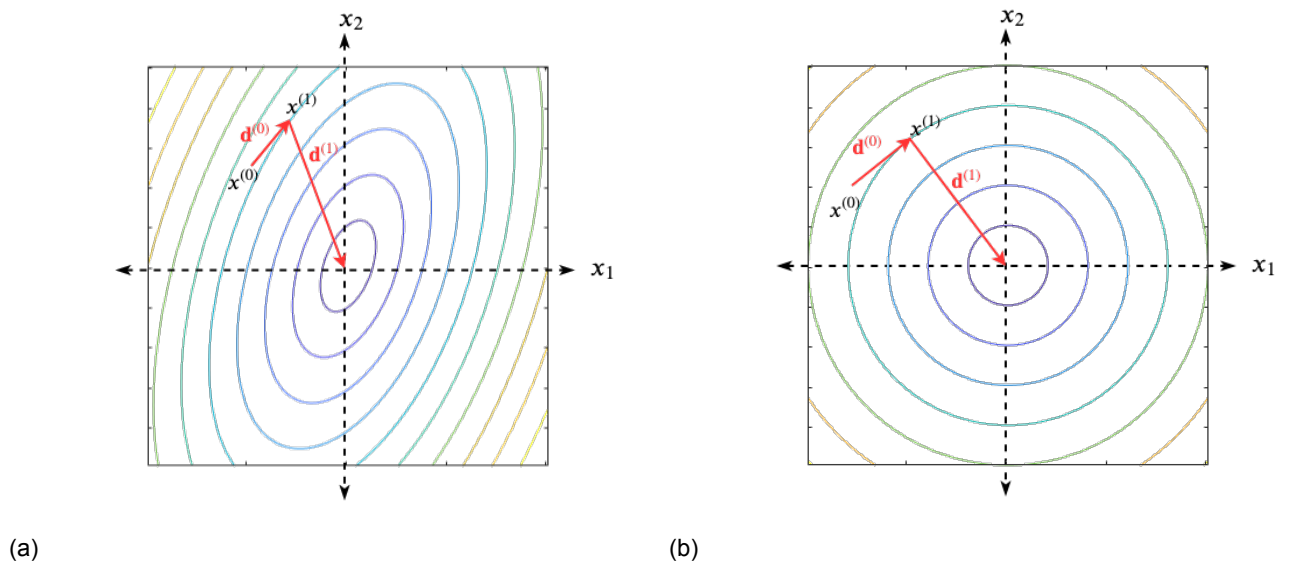


Figure 6.4: Conjugate direction a) contours are ellipsoids b) the same contours in a "transformed" space

When the search vectors are the natural coordinates vector set in  $\mathbb{R}^n$ , this method becomes equivalent to Gaussian elimination[23]. When the search vector,  $\mathbf{d}^{(k)}$ , is found out by the conjugation of the residual vector,  $\mathbf{r}^{(k)} = \mathbf{b} - \mathbf{A}\mathbf{x}^{(k)}$ , then the method is known as conjugate gradient. There are different methods to find these A-orthogonal search vectors. To name some, they are Householder transformation, Givens Transformation, Fast Givens Transformation, and Gram-Schmidt algorithm.

### 6.2.3. Krylov Subspace Connection

A desired property of such algorithms is that they start off searching along the most important directions so that the convergence to the real solution happens faster. Figure 6.5 roughly illustrates this idea. Suppose we are allowed to search the solution along only two orthogonal directions- the horizontal and the vertical. It is clear that in this case after one iteration,  $\mathbf{x}_{hv}^{(1)}$  (figure 6.5a) is closer to the solution,  $\mathbf{x}_{sol}$ , in the euclidean sense than  $\mathbf{x}_{vh}^{(1)}$  (figure 6.5a and b). This means that the horizontal direction, in this sense, is more important than the vertical direction. In case of matrix  $\mathbf{A}$ , the eigenvector corresponding to  $\mathbf{A}$ 's largest eigenvalue,  $\lambda_1(\mathbf{A})$ , is the most important direction.

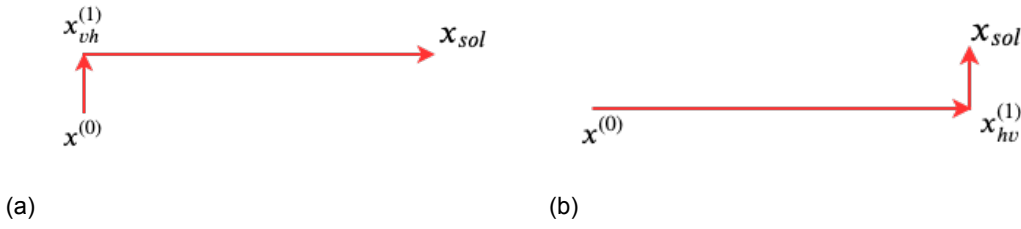


Figure 6.5: a) Search vertically then horizontally b) Search horizontally then vertically

We consider the orthogonal decomposition of matrix  $\mathbf{A}$ -

$$\mathbf{D}_k = \mathbf{Q}_k^T \mathbf{A} \mathbf{Q}_k \quad (6.8)$$

where  $\mathbf{Q} = [\mathbf{q}_1 | \mathbf{q}_2 | \dots | \mathbf{q}_k]$  is an orthogonal matrix, and  $\mathbf{q}_k$ s can be regarded as search vectors.  $k$  is the iteration number of the orthogonalization process. It can be shown that the problem of generating  $\mathbf{A}$ -orthogonal  $\mathbf{q}_k$ s such that  $\lambda_1(\mathbf{D}_k)$  and  $\lambda_n(\mathbf{D}_k)$ <sup>1</sup> are progressively better estimates of  $\lambda_1(\mathbf{A})$  and  $\lambda_n(\mathbf{A})$ , respectively, leads to the problem of finding the orthonormal basis for the Krylov subspaces[10]-

$$\mathcal{K}(\mathbf{A}, \mathbf{q}_1, k) = \text{span}\{\mathbf{q}_1, \mathbf{q}_2, \dots, \mathbf{q}_k\} = \text{span}\{\mathbf{q}_1, \mathbf{A}\mathbf{q}_1, \dots, \mathbf{A}^{k-1}\mathbf{q}_1\} \quad (6.9)$$

### 6.3. Lanczos Tridiagonalization

If  $\mathbf{A}$  is square symmetric, it can be decomposed into a tridiagonal form[10],  $\mathbf{T}$ , as-

$$\mathbf{Q}^T \mathbf{A} \mathbf{Q} = \mathbf{T} \quad (6.10)$$

where  $\mathbf{Q} = [\mathbf{q}_1 | \mathbf{q}_2 | \dots | \mathbf{q}_n]$  is an orthogonal matrix where,

$$\text{span}\{\mathbf{q}_1, \mathbf{q}_2, \dots, \mathbf{q}_n\} = \text{span}\{\mathbf{q}_1, \mathbf{A}\mathbf{q}_1, \dots, \mathbf{A}^{n-1}\mathbf{q}_1\} = \mathcal{K}(\mathbf{A}, \mathbf{q}_1, n) \quad (6.11)$$

Methods like Householder transformation or Givens transformation can be used for the computation of this tridiagonal matrix,  $\mathbf{T}$ . But these methods are not suited if  $\mathbf{A}$  is large and sparse as they destroy sparsity during calculations or are computationally expensive[10]. Lanczos method is useful in this situation which tries to compute the elements of  $\mathbf{T} = \mathbf{Q}^T \mathbf{A} \mathbf{Q}$  directly. We have-

$$\mathbf{T} = \begin{bmatrix} \alpha_1 & \beta_1 & 0 & \dots & 0 \\ \beta_1 & \alpha_2 & \beta_2 & \dots & \cdot \\ 0 & \beta_2 & \dots & \dots & \cdot \\ \cdot & \cdot & \dots & \cdot & \beta_{n-1} \\ 0 & \cdot & \cdot & \beta_{n-1} & \alpha_n \end{bmatrix} \quad (6.12)$$

Comparing the columns of  $\mathbf{A} \mathbf{Q} = \mathbf{Q} \mathbf{T}$ , we get the recursive expression to compute the columns of  $\mathbf{Q}$ -

$$\mathbf{A} \mathbf{q}_k = \beta_{k-1} \mathbf{q}_{k-1} + \alpha_k \mathbf{q}_k + \beta_k \mathbf{q}_{k+1} \quad (6.13)$$

We start the recursion by taking  $\beta_0 = 1$  and  $\mathbf{q}_0 = 0$ . At  $k^{\text{th}}$  iteration, we have-

$$\mathbf{A} \mathbf{Q}_k = \mathbf{Q}_k \mathbf{T}_k + \mathbf{r}_k \mathbf{e}_k^T \quad (\text{where } \mathbf{r}_k = \beta_k \mathbf{q}_{k+1} \text{ and } \mathbf{e}_k = \mathbf{I}_n(\cdot, k)) \quad (6.14)$$

In practice,  $\mathbf{T}_k$  tends to converge to  $\mathbf{A}$ 's eigenvalues at a much smaller  $k$  compared to the dimension of  $\mathbf{A}$ . In other words,  $\mathbf{T}_k$  is a kind of an approximation to  $\mathbf{A}$  whose dimensions are much smaller. Kaniel-Paige Convergence Theory guarantees the convergence of the extremal eigenvalues of  $\mathbf{T}_k$  to that of  $\mathbf{A}$  (There is no such strong theory for the interior eigenvalues though) [10]. If we can use  $\mathbf{T}_k$  instead of  $\mathbf{A}$ , it would greatly reduce our computations.

<sup>1</sup> $\lambda_1(\cdot)$  is the notation for the largest eigenvalue and  $\lambda_n(\cdot)$  is the notation for the smallest eigenvalue

So far we have seen the case when  $\mathbf{A}$  was square and symmetric. But in our application our  $\mathbf{A}$  is tall and non-symmetric. Following two methods describe the approaches taken in this case which will be discussed in the subsequent sections-

1. **Arnoldi's method**
2. **Golub-Kahan Bidiagonalization**

## 6.4. Arnoldi's method

In this method, although  $\mathbf{A}$  can be non-symmetric it has to be square. Now, because  $\mathbf{A}$  is non-symmetric, the decomposition  $\mathbf{Q}^T \mathbf{A} \mathbf{Q} = \mathbf{H}$  is a Hessenberg matrix and not a tridiagonal matrix.

$$\mathbf{H} = \begin{bmatrix} h_{11} & h_{12} & h_{13} & \dots & h_{1,n} \\ h_{21} & h_{22} & h_{23} & \dots & h_{2,n} \\ 0 & h_{32} & \dots & \dots & \cdot \\ \cdot & \dots & \dots & h_{n-1,n-1} & h_{n-1,n} \\ 0 & \cdot & 0 & h_{n,n-1} & h_{n,n} \end{bmatrix} \quad (6.15)$$

If we compute the columns of  $\mathbf{Q}$ , in Lanczos style, by comparing  $\mathbf{A} \mathbf{Q} = \mathbf{Q} \mathbf{H}$ , we no longer get short recursive formulas for computing  $\mathbf{q}_{k+1}$ . As the iteration proceeds, the expression becomes longer and longer. It is due to this reason that such method is stopped early on and restarted with a new and better initial guess  $\mathbf{q}_0$ . Moreover, this method does not converge in the style of Kaniel-Paige Convergence Theory, and initial guess plays a big role in converging [10].

## 6.5. Golub-Kahan Bidiagonalization

In this method,  $\mathbf{A}$  can be non-symmetric as well as rectangular. Instead of a QR type of decomposition, this method relies on a SVD style of decomposition. Here we have  $\mathbf{U}^T \mathbf{A} \mathbf{V} = \mathbf{B}$ , where  $\mathbf{B}$  is a lower bidiagonal matrix, and  $\mathbf{U}$  and  $\mathbf{V}$  are orthogonal matrices.

$$\mathbf{B} = \begin{bmatrix} \alpha_1 & 0 & 0 & \dots & 0 \\ \beta_1 & \alpha_2 & 0 & \dots & \cdot \\ 0 & \beta_2 & \dots & \dots & \cdot \\ \cdot & 0 & \dots & \alpha_{n-1} & 0 \\ 0 & \cdot & \cdot & \beta_{n-1} & \alpha_n \\ 0 & \cdot & \cdot & 0 & \beta_n \end{bmatrix} \quad (6.16)$$

To get the the columns of  $\mathbf{U}$  and  $\mathbf{V}$  in Lanczos style, comparing the columns of  $\mathbf{A} \mathbf{V} = \mathbf{U} \mathbf{B}$  and  $\mathbf{U}^T \mathbf{A} = \mathbf{B} \mathbf{V}^T$  we get-

$$\mathbf{A}^T \mathbf{u}_k = \beta_{k-1} \mathbf{v}_{k-1} + \alpha_k \mathbf{v}_k \quad , \text{and} \quad \mathbf{A} \mathbf{v}_k = \alpha_k \mathbf{u}_k + \beta_k \mathbf{v}_{k+1} \quad (6.17)$$

The recursion is started with  $\beta_0 = 1$  and  $\mathbf{v}_0 = 0$ . This algorithm converges in the style similar to Kaniel-Paige Convergence Theory[10]. The downside of this algorithm is that two matrix multiplication (with  $\mathbf{A}^T$  and  $\mathbf{A}$ ) is needed in every iteration which is a computational overhead.

At this point, the author believes that sufficient background has been provided to get some idea about the algorithms that are being used in this work. Next, a short description of the IRTools package is provided, followed by brief descriptions of the algorithms chosen from it, to reconstruct the image.

## 6.6. IR Tools

IR Tools is a MATLAB software package that contains a range of iterative solvers suited for large-scale linear inverse problems[9]. Additionally, it contains several test problem examples to demonstrate the use of the algorithms. These examples are useful in testing the algorithms. It also serves as a reference to be of help during the debugging of one's own implementation

of the algorithms. It includes iterative regularization methods and automatic regularization parameter selection methods. To get more information about this toolbox [9] can be referred.

Out of the many algorithms in the toolbox, two algorithms were chosen. They are 1) **IRhybrid\_Isqr**, and 2) **IRhtv**. They were chosen on the following basis-

1. They can handle rectangular matrices.
2. Iterative regularization parameter selecting algorithms were implemented in these algorithms.
3. The regularization matrix in IRhybrid\_Isqr is chosen to be Laplacian, and the regularization term in IRhtv is the total variance operator (will be discussed later). Both are useful in image reconstruction purposes.

Next we discuss the algorithms themselves.

## 6.7. IRhybrid\_Isqr

IRhybrid\_Isqr [3] solves the Tikhonov's regularization problem (equation 5.5)-

$$\underset{\mathbf{x}}{\text{minimize}} \quad \left\| \begin{pmatrix} \mathbf{A} \\ \sqrt{\lambda} \mathbf{L} \end{pmatrix} \mathbf{x} - \begin{pmatrix} \mathbf{b} \\ 0 \end{pmatrix} \right\|_2^2$$

For convenience, let us consider  $\begin{pmatrix} \mathbf{A} \\ \sqrt{\lambda} \mathbf{L} \end{pmatrix}$  as  $\tilde{\mathbf{A}}$  and  $\begin{pmatrix} \mathbf{b} \\ 0 \end{pmatrix}$  as  $\tilde{\mathbf{b}}$  in this section.

IRhybrid\_Isqr uses Golub-Kahan bidiagonalization to decompose  $\tilde{\mathbf{A}}$  into a lower bidiagonal matrix  $\mathbf{B}$  i.e.  $\mathbf{U}^T \tilde{\mathbf{A}} \mathbf{V} = \mathbf{B}$  (section 6.5) such that in the  $k^{\text{th}}$  iteration we have-

$$\begin{aligned} \tilde{\mathbf{A}}^T \mathbf{U}_k &= \mathbf{V}_k \mathbf{B}_k^T + \alpha_k \mathbf{v}_{k+1} \mathbf{e}_k^T \quad (\text{where } \mathbf{e}_k = \mathbf{I}_n(:, k)) \\ \tilde{\mathbf{A}} \mathbf{V}_k &= \mathbf{U}_k \mathbf{B}_k \end{aligned} \quad (6.18)$$

It then approximates the following least squares problem

$$\underset{\mathbf{x}}{\text{minimize}} \quad \|\tilde{\mathbf{A}} \mathbf{x} - \tilde{\mathbf{b}}\|_2^2 \quad (6.19)$$

by the following projected least squares problem-

$$\underset{\mathbf{x} \in \mathcal{R}(\mathbf{V}_k)}{\text{minimize}} \quad \|\tilde{\mathbf{A}} \mathbf{x} - \tilde{\mathbf{b}}\|_2^2 = \underset{\mathbf{f}}{\text{minimize}} \quad \|\mathbf{U}_k^T \tilde{\mathbf{b}} - \mathbf{B}_k \mathbf{f}\|_2^2 \quad (6.20)$$

where,  $\mathbf{x}^{(k)} = \mathbf{V}_k \mathbf{f}$ .

### 6.7.1. Discrepancy Principle in IRhybrid\_Isqr

This description is taken from [7] where the authors have explained the case for Arnoldi's method. Nevertheless, this method can be used for Golub-Kahan bidiagonalization also. Therefore, the reader should remember that although this explanation is given for Arnoldi's method, it can be extended for Golub-Kahan bidiagonalization also by substituting the appropriate expression.

To recap, discrepancy principle can be described as-

$$\text{Choose } \lambda \text{ such that } \|\mathbf{A} \mathbf{x}_\lambda^{(k)} - \mathbf{b}\| \geq \eta \epsilon \quad (6.21)$$

As soon as  $\|\mathbf{A} \mathbf{x}_\lambda^{(k)} - \mathbf{b}\|$  becomes smaller than  $\eta \epsilon$ , the iteration is stopped. At every iteration, we define the discrepancy function as-

$$\phi^{(k)}(\lambda) = \|\mathbf{A} \mathbf{x}_\lambda^{(k)} - \mathbf{b}\| \quad (6.22)$$

We can expand the expression of the discrepancy function by using  $\mathbf{Q}^T \mathbf{A} \mathbf{Q} = \mathbf{H}$  (in case of Golub-Kahan bidiagonalization it will be  $\mathbf{U}^T \tilde{\mathbf{A}} \mathbf{V} = \mathbf{B}$ ). We make use of the Taylor approximation-

$$\phi^{(k)}(\lambda) \approx \hat{\alpha}^{(k)} + \lambda \hat{\beta}^{(k)} \quad (6.23)$$

where  $\hat{\alpha}^{(k)} = \phi^{(k)}(0)$  and  $\hat{\beta}^{(k)} \approx \frac{\phi^{(k)}(\lambda^{(k-1)}) - \hat{\alpha}^{(k)}}{\lambda^{(k-1)}}$ . It can be shown that by rearranging the above equation, we can obtain an iterative algorithm for  $\lambda$ . This rule is also called the Secant rule.

$$\lambda^{(k)} = \left| \frac{\eta \epsilon - \hat{\alpha}^{(k)}}{\phi^{(k)}(\lambda^{(k-1)}) - \hat{\alpha}^{(k)}} \right| \lambda^{(k-1)} \quad (6.24)$$

where modulus is added to make the regularization parameter positive. GCV can also be used in place of discrepancy principle which is described in section 5.3.2.

### 6.7.2. IRhybrid\_Isqr Algorithm

The IRhybrid\_Isqr algorithm can be summarized as

---

#### Algorithm 1 IRhybrid\_Isqr

---

- 1: Input:  $\mathbf{A}$ ,  $\mathbf{b}$ ,  $\mathbf{L}$ ,  $\epsilon$ , and  $\eta$
  - 2: Initialize:  $\lambda^{(0)} = 1$  and  $\mathbf{x}^{(0)} = \mathbf{0}$
  - 3: **for**  $k = 1, 2, \dots, N$  **do**
  - 4:   Decompose  $\mathbf{A}$  using Golub-Kahan bidiagonalization
  - 5:   Solve the regularized projected least square problem
  - 6:   Use discrepancy or GCV to select  $\lambda$  at each step
- 

## 6.8. IRhtv

The information given here is taken from [8]. More insight can be obtained by referring to the same.

Moving forward, we consider the Tikhonov problem (equation 5.4) again-

$$\underset{\mathbf{x}}{\text{minimize}} \quad \|\mathbf{Ax} - \mathbf{b}\|_2^2 + \lambda \|\mathbf{Lx}\|_2^2$$

There are algorithms that recompute  $\mathbf{L}$  at each iteration such that  $\|\mathbf{Lx}\|_2^2 \approx G(\mathbf{x})$ , so that the problem becomes-

$$\underset{\mathbf{x}}{\text{minimize}} \quad \|\mathbf{Ax} - \mathbf{b}\|_2^2 + \lambda \|\mathbf{Lx}\|_2^2 \approx \underset{\mathbf{x}}{\text{minimize}} \quad \|\mathbf{Ax} - \mathbf{b}\|_2^2 + \lambda G(\mathbf{x}) \quad (6.25)$$

IRhtv is one such algorithm where  $G(\mathbf{x}) = TV(\mathbf{x})$ , where  $TV(\mathbf{x})$  is the total variance operator. TV operator is defined as-

$$\begin{aligned} TV(\mathbf{x}) &= \sum_{i=1}^N \sqrt{[\mathbf{D}_h \mathbf{x}]_i^2 + [\mathbf{D}_v \mathbf{x}]_i^2} \\ &= \|\sqrt{[\mathbf{D}_h \mathbf{x}]_i^2 + [\mathbf{D}_v \mathbf{x}]_i^2}\|_1 \\ &= \|\sqrt{d}\|_1 \end{aligned} \quad (6.26)$$

where  $\mathbf{D}_h$  and  $\mathbf{D}_v$  denotes the finite difference approximations of the horizontal and vertical first derivative operators respectively.  $[\cdot]_i$  denotes the  $i^{th}$  element of the vector. Thus, IRhtv can be thought of solving a sort of 1-norm regularized problem. To do this we do the following substitutions-

$$\begin{aligned} \mathbf{L} &= \mathbf{W} \mathbf{D}_{hv} \\ &= TV(\mathbf{x}) \end{aligned} \quad (6.27)$$

, where

$$\mathbf{D}_{hv} = \begin{bmatrix} \mathbf{D}_h \\ \mathbf{D}_v \end{bmatrix}, \quad \mathbf{W} = \begin{bmatrix} \tilde{\mathbf{W}} & 0 \\ 0 & \tilde{\mathbf{W}} \end{bmatrix}, \quad \text{and} \quad \tilde{\mathbf{W}} = \begin{bmatrix} \frac{1}{\sqrt[4]{[\mathbf{D}_h \mathbf{x}]_1^2 + [\mathbf{D}_v \mathbf{x}]_1^2}} & 0 & \dots & 0 \\ 0 & \frac{1}{\sqrt[4]{[\mathbf{D}_h \mathbf{x}]_2^2 + [\mathbf{D}_v \mathbf{x}]_2^2}} & \dots & 0 \\ \vdots & \vdots & \ddots & \vdots \\ 0 & 0 & \dots & \frac{1}{\sqrt[4]{[\mathbf{D}_h \mathbf{x}]_N^2 + [\mathbf{D}_v \mathbf{x}]_N^2}} \end{bmatrix}$$

In the algorithm of IRhtv there are two loops involved- the outer loop and inner loop. The inner loop aims to solve the projected regularized least square problem using the  $\mathbf{L}$  matrix obtained from the outer loop. At each iteration of the inner loop, it employs the discrepancy principle or GCV to arrive at the appropriate  $\lambda$ . The outer loop recomputes the  $\mathbf{L}$  matrix to obtain  $TV(\mathbf{x}^{(k)})$ . It also sets new quantities for the next restart of the inner loop. In IR Tools there is also an option to find  $\mathbf{x}^{(k)}$  such that it is always positive, something which is desirable for image reconstruction applications.

---

**Algorithm 2** IRhtv

---

- 1: Input:  $\mathbf{A}$ ,  $\mathbf{b}$ ,  $\epsilon$ , and  $\eta$
  - 2: Initialize:  $\lambda^{(0)} = 1$ ,  $\mathbf{L} = \mathbf{I}$ , and  $\mathbf{x}^{(0)} = \mathbf{0}$
  - 3: **for**  $k = 1, 2, \dots, N_R$  **do**
  - 4:     **for**  $k = 1, 2, \dots, N_D$  **do**
  - 5:         Input:  $\mathbf{L}$ ,  $\lambda^{(0)}$ ,  $\mathbf{x}^{(0)}$
  - 6:         Decompose  $\mathbf{A}$  using Arnoldi's method or Golub-Kahan bidiagonalization
  - 7:         Solve the regularized projected least square problem
  - 8:         Use discrepancy or GCV to select  $\lambda$  at each step
  - 9:     Project  $\mathbf{x}^{(N_D)}$  into the positive space by taking  $\mathbf{x}^{(N_D)}(\mathbf{x}^{(N_D)} < \mathbf{0}) = \mathbf{0}$  (Optional)
  - 10:     Initialize:  $\lambda^{(0)} = \lambda_{N_D}$  and  $\mathbf{x}^{(0)} = \mathbf{x}^{(N_D)}$
  - 11:     Define  $\mathbf{L} = \mathbf{W}\mathbf{D}_{hv}$  as in equation 6.27
- 

## 6.9. Regularization matrix handling

### 6.9.1. IRhybrid\_lsqr

In IRTools package, in order to bring the Tikhonov problem to a standard form, it is possible to apply preconditioning to the  $\mathbf{A}$  matrix.

$$\underset{\mathbf{x}}{\text{minimize}} \quad \|\mathbf{Ax} - \mathbf{b}\|_2^2 + \lambda \|\mathbf{Lx}\|_2^2 \quad (\text{Non-standard form}) \quad (6.28)$$

$$\underset{\mathbf{x}}{\text{minimize}} \quad \|\mathbf{Ax} - \mathbf{b}\|_2^2 + \lambda \|\mathbf{x}\|_2^2 \quad (\text{Standard form}) \quad (6.29)$$

To do this, a new variable  $\xi$  is introduced such that  $\mathbf{x} = \mathbf{L}^{-1}\xi$ . Equation 6.30 shows the non-standard problem that has been modified. Notice that it is now in a standard form.

$$\underset{\xi}{\text{minimize}} \quad \|\mathbf{AL}^{-1}\xi - \mathbf{b}\|_2^2 + \lambda \|\xi\|_2^2 \quad (6.30)$$

This is done so that the expression for parameter selection methods become simpler to compute. Without this substitution, the  $\mathbf{L}$  matrix appears in the formulae of the aforementioned methods, and this requires multiple multiplications involving  $\mathbf{L}$ . This makes the whole reconstruction process slow.

IRhybrid\_lsqr uses this kind of preconditioning whenever a regularization matrix is used, and tries to solve the non-standard problem shown in equation 6.30.

### 6.9.2. IRhtv

IRhtv, on the other hand, uses another approach to solve the general Tikhonov problem of the form-

$$\underset{\mathbf{x}}{\text{minimize}} \quad \|\mathbf{Ax} - \mathbf{b}\|_2^2 + \lambda \|\mathbf{L}(\mathbf{x} - \mathbf{x}_0)\|_2^2 \quad (6.31)$$

where,  $\mathbf{x}_0$  is the initial guess vector. When  $\mathbf{A}$  is square ( $n = m$ ), Arnoldi's algorithm (section 6.4) can be used. Here  $\mathbf{A}$  is decomposed as  $\mathbf{AQ}_k = \mathbf{Q}_{k+1}\mathbf{H}_k$ , where  $\mathbf{Q}_{k+1} = [\mathbf{q}_1|\mathbf{q}_2|\dots|\mathbf{q}_{k+1}] \in \mathbb{C}^{n \times (k+1)}$  is an orthogonal matrix. IRhtv searches for the solution in the Krylov subspace given by-

$$\mathcal{K}(\mathbf{A}, \mathbf{r}_0, k) = \text{span}\{\mathbf{r}_0, \mathbf{Ar}_0, \dots, \mathbf{A}^{k-1}\mathbf{r}_0\} \quad (6.32)$$

where,  $\mathbf{r}_0 = \mathbf{b} - \mathbf{Ax}_0$ , and  $k$  is much smaller than the dimension of  $\mathbf{A}$ . The approximate solution,  $\mathbf{x}^{(k)}$ , of this problem belongs to  $\mathbf{x}_k = \mathbf{x}_0 + \mathcal{K}(\mathbf{A}, \mathbf{r}_0, k)$ . Using Arnoldi's method, we substitute  $\mathbf{x} = \mathbf{x}_0 + \mathbf{Q}_k\mathbf{y}$ , where  $\mathbf{y} \in \mathbb{C}^{k \times 1}$ . Thus, problem 6.31 can be reduced as follows-

$$\begin{aligned} & \underset{\mathbf{x} \in \mathbb{C}^n}{\text{minimize}} \quad \|\mathbf{Ax} - \mathbf{b}\|_2^2 + \lambda \|\mathbf{L}(\mathbf{x} - \mathbf{x}_0)\|_2^2 \\ &= \underset{\mathbf{x} = \mathbf{x}_0 + \mathbf{Q}_k\mathbf{y} \in \mathbb{C}^{n \times 1}}{\text{minimize}} \quad \|\mathbf{Ax}_0 + \mathbf{AQ}_k\mathbf{y} - \mathbf{b}\|_2^2 + \lambda \|\mathbf{L}(\mathbf{x}_0 + \mathbf{Q}_k\mathbf{y} - \mathbf{x}_0)\|_2^2 \quad (\text{substituting } \mathbf{x} = \mathbf{x}_0 + \mathbf{Q}_k\mathbf{y}) \\ &= \underset{\mathbf{y} \in \mathbb{C}^k}{\text{minimize}} \quad \|\mathbf{AQ}_k\mathbf{y} + \mathbf{Ax}_0 - \mathbf{b}\|_2^2 + \lambda \|\mathbf{LQ}_k\mathbf{y}\|_2^2 \\ &= \underset{\mathbf{y} \in \mathbb{C}^k}{\text{minimize}} \quad \|\mathbf{Q}_{k+1}\mathbf{H}_k\mathbf{y} - \mathbf{r}_0\|_2^2 + \lambda \|\mathbf{LQ}_k\mathbf{y}\|_2^2 \quad (\text{from Arnoldi's method, and } \mathbf{r}_0 = \mathbf{b} - \mathbf{Ax}_0) \\ &= \underset{\mathbf{y} \in \mathbb{C}^k}{\text{minimize}} \quad \|\mathbf{Q}_{k+1}\mathbf{H}_k\mathbf{y} - \mathbf{q}_1\|\mathbf{r}_0\|_2\|_2^2 + \lambda \|\mathbf{LQ}_k\mathbf{y}\|_2^2 \quad (\text{where } \mathbf{q}_1 \text{ is defined as } \mathbf{q}_1 = \frac{\mathbf{r}_0}{\|\mathbf{r}_0\|_2}) \\ & \hspace{15em} (\text{since } \mathbf{q}_1 \text{ is the first column} \\ & \hspace{15em} \text{of } \mathbf{Q}_k \text{ and } \mathbf{e}_1 = [1 \ 0 \ \dots \ 0]^T) \\ &= \underset{\mathbf{y} \in \mathbb{C}^k}{\text{minimize}} \quad \|\mathbf{Q}_{k+1}\mathbf{H}_k\mathbf{y} - \mathbf{Q}_{k+1}\mathbf{e}_1\|\mathbf{r}_0\|_2\|_2^2 + \lambda \|\mathbf{LQ}_k\mathbf{y}\|_2^2 \quad (\text{since } \mathbf{Q}_{k+1} \text{ is orthogonal, and orthogonal} \\ & \hspace{15em} \text{transformations are invariant} \\ & \hspace{15em} \text{under 2-norm}) \\ &= \underset{\mathbf{y} \in \mathbb{C}^k}{\text{minimize}} \quad \|\mathbf{H}_k\mathbf{y} - \mathbf{e}_1\|\mathbf{r}_0\|_2\|_2^2 + \lambda \|\mathbf{LQ}_k\mathbf{y}\|_2^2 \end{aligned} \quad (6.33)$$

Now, the  $\mathbf{L}$  matrix in equation 6.33 can be reduced further as  $\mathbf{LQ}_k = \mathbf{V}_k\mathbf{R}_k$  is another orthogonal decomposition.  $\mathbf{V}_k \in \mathbb{C}^{v \times k}$  is an orthogonal matrix, and  $\mathbf{R}_k \in \mathbb{C}^{k \times k}$  is an upper triangular matrix. Therefore, equation 6.33 becomes-

$$\underset{\mathbf{y} \in \mathbb{C}^k}{\text{minimize}} \quad \|\mathbf{H}_k\mathbf{y} - \mathbf{e}_1\|\mathbf{r}_0\|_2\|_2^2 + \lambda \|\mathbf{R}_k\mathbf{y}\|_2^2 \quad (6.34)$$

When the initial guess vector,  $\mathbf{x}_0 = 0$  then  $\mathbf{r}_0 = \mathbf{b}$  and the equation 6.34 becomes-

$$\underset{\mathbf{y} \in \mathbb{C}^k}{\text{minimize}} \quad \|\mathbf{H}_k\mathbf{y} - \mathbf{e}_1\|\mathbf{b}_0\|_2\|_2^2 + \lambda \|\mathbf{R}_k\mathbf{y}\|_2^2 \quad (6.35)$$

This concept can also be extended to cases where  $\mathbf{A}$  is rectangular[8]. The problem in equation 6.35 is of much smaller dimension at the earlier part of the iterations compared to equation 6.31. IRhtv, being a Krylov subspace method, looks for the most important direction in the beginning. This leads to a faster convergence to the solution.

## Part 3: Results and Analysis





## Simulations

The background information needed to follow the work done in this thesis was provided in Part 1 and Part 2. For this part, we recall the matrix version of the signal model that was derived in chapter 4 as shown below-

$$\begin{bmatrix} d(k_1, \theta_1) \\ d(k_2, \theta_1) \\ \vdots \\ d(k_M, \theta_1) \\ d(k_1, \theta_2) \\ \vdots \\ d(k_M, \theta_2) \\ \vdots \\ d(k_M, \theta_R) \end{bmatrix} = \begin{bmatrix} \mathcal{K}(r_1; \theta_1)e^{-p(r_2; \theta_1)k_1} & \mathcal{K}(r_2; \theta_1)e^{-p(r_2; \theta_1)k_1} & \dots & \mathcal{K}(r_N; \theta_1)e^{-p(r_N; \theta_1)k_1} \\ \mathcal{K}(r_1; \theta_1)e^{-p(r_2; \theta_1)k_2} & \mathcal{K}(r_2; \theta_1)e^{-p(r_2; \theta_1)k_2} & \dots & \mathcal{K}(r_N; \theta_1)e^{-p(r_N; \theta_1)k_2} \\ \vdots & \vdots & \dots & \vdots \\ \mathcal{K}(r_1; \theta_1)e^{-p(r_2; \theta_1)k_M} & \mathcal{K}(r_2; \theta_1)e^{-p(r_2; \theta_1)k_M} & \dots & \mathcal{K}(r_N; \theta_1)e^{-p(r_N; \theta_1)k_M} \\ \mathcal{K}(r_1; \theta_2)e^{-p(r_2; \theta_2)k_1} & \mathcal{K}(r_2; \theta_2)e^{-p(r_2; \theta_2)k_1} & \dots & \mathcal{K}(r_N; \theta_2)e^{-p(r_N; \theta_2)k_1} \\ \vdots & \vdots & \dots & \vdots \\ \mathcal{K}(r_1; \theta_2)e^{-p(r_2; \theta_2)k_M} & \mathcal{K}(r_2; \theta_2)e^{-p(r_2; \theta_2)k_M} & \dots & \mathcal{K}(r_N; \theta_2)e^{-p(r_N; \theta_2)k_M} \\ \vdots & \vdots & \dots & \vdots \\ \mathcal{K}(r_1; \theta_R)e^{-p(r_2; \theta_R)k_M} & \mathcal{K}(r_2; \theta_R)e^{-p(r_2; \theta_R)k_M} & \dots & \mathcal{K}(r_N; \theta_R)e^{-p(r_N; \theta_R)k_M} \end{bmatrix} \begin{bmatrix} \rho(r_1) \\ \rho(r_2) \\ \vdots \\ \rho(r_N) \end{bmatrix}$$

The image reconstructed by using this model will depend on many factors. To get the best out of this model, we should focus our attention on those factors which we have control over. We can manipulate parameters like the chosen time samples, the rotated angle of the MRI machine, the regularization parameter of the reconstruction algorithms, and so on. This chapter examines the link between these parameters and the reconstructed image. The following investigations are done in the following order-

1. Time Domain Data Size and Dwell Time Investigation.
2. Parameter Selection Strategy Investigation.
3. Signal Model for Rotating MRI Investigation.
4. Angle Combination Investigation.

For each of the investigations, a brief description on how they were studied is provided before the results of the simulations. The B0 field used in all the simulations of this chapter is shown below (figure 7.1).

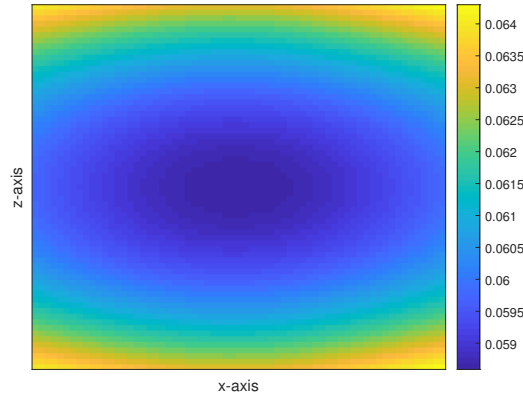


Figure 7.1: Interpolated z component of B0 map used in the simulations.

## 7.1. Time Domain Data Size and Dwell Time Investigation

In this investigation, we are going to ignore the  $\mathcal{K}(r_n; \theta_r)$  term in the signal model to make the analysis easier. We will investigate its influence in section 7.3. Also, we can ignore  $\frac{1}{T_2}$  in  $p(\vec{r}; \theta)$  because its contribution is small when inhomogeneities in the main magnetic field cannot be ignored. Then we have-

$$\begin{bmatrix} d(k_1, \theta_1) \\ d(k_2, \theta_1) \\ \vdots \\ d(k_M, \theta_1) \\ d(k_1, \theta_2) \\ \vdots \\ d(k_M, \theta_2) \\ \vdots \\ d(k_M, \theta_R) \end{bmatrix} = \begin{bmatrix} e^{-i\omega_0(r_2; \theta_1)k_1} & e^{-i\omega_0(r_2; \theta_1)k_1} & \dots & e^{-i\omega_0(r_N; \theta_1)k_1} \\ e^{-i\omega_0(r_2; \theta_1)k_2} & e^{-i\omega_0(r_2; \theta_1)k_2} & \dots & e^{-i\omega_0(r_N; \theta_1)k_2} \\ \vdots & \vdots & \dots & \vdots \\ e^{-i\omega_0(r_2; \theta_1)k_M} & e^{-i\omega_0(r_2; \theta_1)k_M} & \dots & e^{-i\omega_0(r_N; \theta_1)k_M} \\ e^{-i\omega_0(r_2; \theta_2)k_1} & e^{-i\omega_0(r_2; \theta_2)k_1} & \dots & e^{-i\omega_0(r_N; \theta_2)k_1} \\ \vdots & \vdots & \dots & \vdots \\ e^{-i\omega_0(r_2; \theta_2)k_M} & e^{-i\omega_0(r_2; \theta_2)k_M} & \dots & e^{-i\omega_0(r_N; \theta_2)k_M} \\ \vdots & \vdots & \dots & \vdots \\ e^{-i\omega_0(r_2; \theta_R)k_M} & e^{-i\omega_0(r_2; \theta_R)k_M} & \dots & e^{-i\omega_0(r_N; \theta_R)k_M} \end{bmatrix} \begin{bmatrix} \rho(r_1) \\ \rho(r_2) \\ \vdots \\ \rho(r_N) \end{bmatrix} \quad (7.1)$$

In this part, we examine the choice of  $k_1$ ,  $k_2$  and  $k_M$  such that the reconstruction of the original image improves. The number of time samples taken,  $M$ , is called Time Domain Data Size (TD). The time step between two adjacent time samples is called Dwell Time<sup>1</sup> (DW). The choices of both TD and DW affects the reconstructed image.

In section 4.8, we have discussed the k-space consideration of the rotating MRI machine. We will now take a small diversion and see how k-space relates to the field-of-view and pixel width (for conventional MRI). Field-of-view (FOV) is the region over which the image is observed, and it is composed of fundamental elements called pixels. The k-space and the spatial domain are inversely related to each other[16][14]. That is, k-space sampling interval,  $\Delta k' = \frac{1}{FOV}$  and pixel width,  $\Delta w = \frac{1}{k_{FOV}}$ . The definitions are illustrated in figure 7.2. So, we can expect the following to be true-

1. If the pixel width,  $\Delta w$ , decreases, which implies the increase of image resolution, the  $k'_{FOV}$  will increase. That means higher frequencies have to be sampled. Since  $\Delta\omega_0 t = k'_x x + k'_z z$  (section 4.8), therefore, this implies that longer acquisition time,  $t$ , is needed. So the maximum duration,  $t = t_{max}$ , will dictate the highest frequencies that have to be sampled in the k-space.
2. The k-space sampling interval,  $\Delta k'$  (therefore DW because  $\Delta t \propto \Delta k'$ ), and FOV are inversely related. If the k-space is under-sampled, and  $\Delta k'$  increases beyond  $\frac{1}{FOV}$ , it will result in an aliasing effect[14]. This is a result of Nyquist's criteria.

<sup>1</sup>In signal processing literature, sampling time means the same thing as Dwell Time. But in MRI literature, the sampling time is reserved to mean something else. It refers to the time window within which the signal is collected.

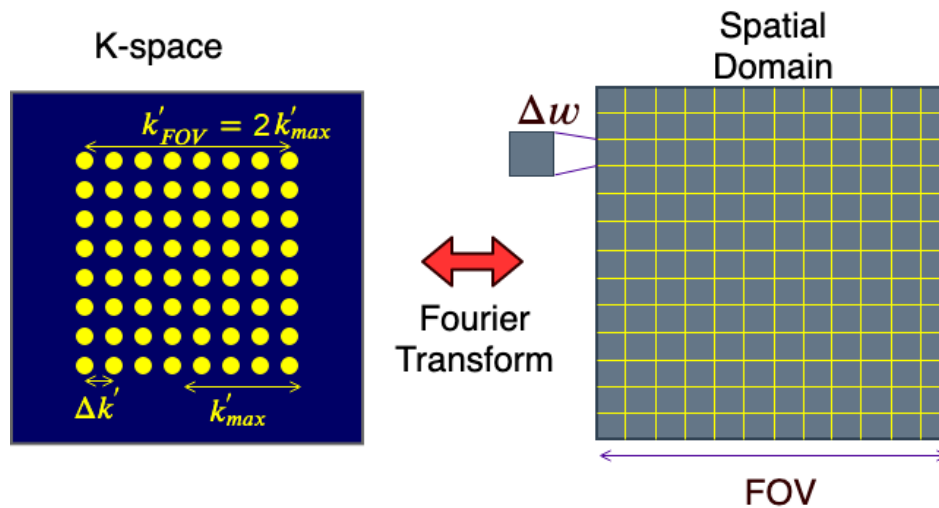


Figure 7.2: Relationship between k-space and spatial domain

The illustration of figure 7.2 is shown here for cartesian sampling, where the k-space data is acquired rectilinearly. Whereas, as can be referred from section 4.8, the data acquisition in the rotating MRI machine happens radially. In radial sampling, the aliasing artifacts have a different form than those in Cartesian scanning. These effects in radial sampling are seen as curvilinear bands that are diffusely distributed across the image. Simulation in figure 7.3 shows this (all parameters that were used for this simulation, except TD, DW, algorithm and SNR, are the same as that in table 7.1. Here, no noise is added, and only results for IRhybrid\_lsqr is shown). Figure 7.3a is the ground truth image that we are trying to reconstruct using a maximum time duration of  $k_M = (DW)(TD) = 5.12ms$ . Figure 7.3b-f shows the reconstructed image, obtained by successively decreasing the DW from 1.28ms to 40μs. The curvilinear aliasing artifact is quite noticeable in 7.3b and 7.3c, which means that the k-space is undersampled in this case. As we decrease the DW, this aliasing artifact is reduced.

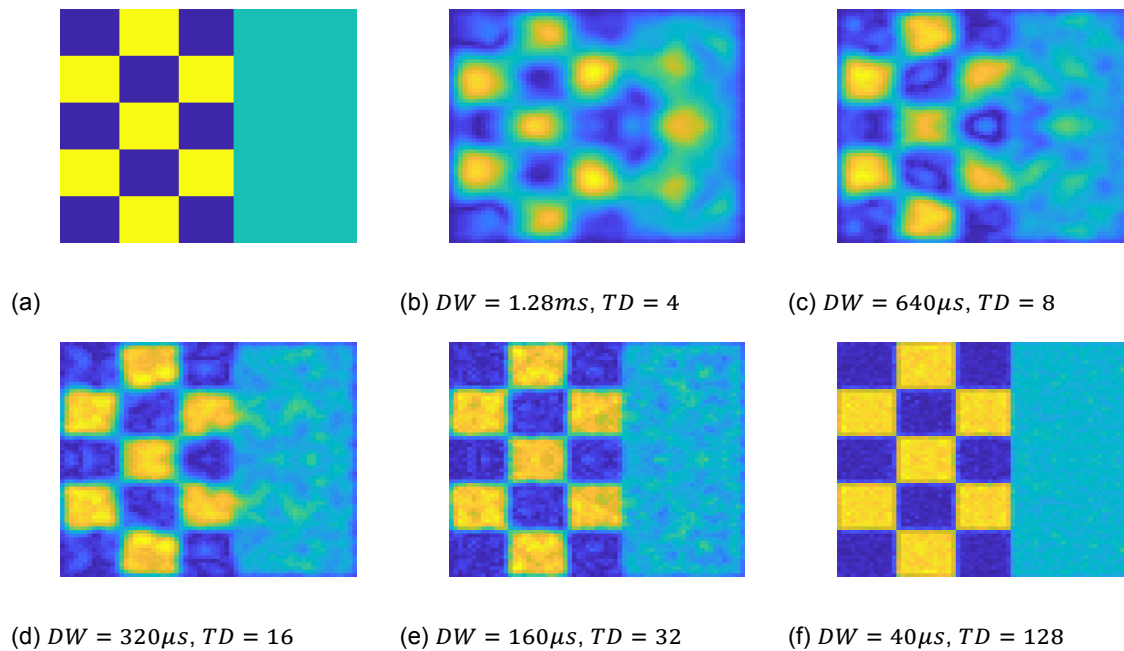


Figure 7.3: Figure illustrating the aliasing artifact due to undersampling of k-space. a) Ground truth b)-f) Reconstructed image. Maximum duration is taken as  $k_M = (DW)(TD) = 5.12ms$ .

It is to be kept in mind that for the rotating MRI machine, the non-linearities in the  $B_0$  profile cannot be easily ignored. Equation 7.2b shows the signal model when a more appropriate and general  $B_0$  profile is considered, with both linear and non-linear terms.

$$\begin{aligned}
 d(t; \theta) &= \int_{\mathbf{r} \in \mathbb{D}_{smp}} \rho(\vec{\mathbf{r}}) \mathcal{K}(\vec{\mathbf{r}}; \theta) e^{-\left(\frac{1}{T_2} + i\gamma(G_x x + G_z z)\right)t} d\mathbf{r} && \text{a) Signal model with linear } B_0 \text{ profile} \\
 d(t; \theta) &= \int_{\mathbf{r} \in \mathbb{D}_{smp}} \rho(\vec{\mathbf{r}}) \mathcal{K}(\vec{\mathbf{r}}; \theta) e^{-\left(\frac{1}{T_2} + i\gamma(G_x x + G_z z + g_x x^2 + g_z z^2)\right)t} d\mathbf{r} && \text{b) Signal model with non-linear } B_0 \text{ profile}
 \end{aligned} \tag{7.2}$$

Where  $G_x$ ,  $G_z$ ,  $g_x$  and  $g_z$  are constants, and it is assumed that there are no gradients along the  $y$ -direction. Due to this, this signal is not in the form of a Fourier transform expression. That means that the mapping between the  $k$ -space and spatial domain, for this case, is not the same as that in conventional MRI machines. The field map was assumed to be linear in this work to make the analysis simpler. Parameters (like Nyquist frequency) for the aforementioned  $k$ -space mapping can be investigated in future work by approximating the field by a more appropriate quadratic  $B_0$  field map. Also, in our case, aliasing is more likely to happen in the middle of the field map because the gradient magnitude of the field map is less there.

Next, the results of two simulations are provided where 1) we vary the TD by keeping the DW fixed, 2) we vary the DW by keeping the TD fixed. For both of these simulations, the parameters that are selected are summarized in table 7.1.

Table 7.1: TD and DW investigation parameters

Parameters	Choices Used for Simulation
(TD,DW)	Can be referred from the simulations of this section
Reconstruction Algorithm	1) IRhybrid_lsqr, 2) IRhtv
Maximum Iteration	1) IRhybrid_lsqr: 200, 2) IRhtv: Max inner iteration $\times$ Max outer iteration = $30 \times 30 = 900$
Parameter Selection Strategy	Discrepancy principle with exact noise estimate. This exact noise estimate is computed as $\epsilon_{exact} = \frac{\ \mathbf{b} - \mathbf{A}\mathbf{x}_{true}\ _2}{\ \mathbf{b}\ _2}$ . The notational conventions follow from chapter 5. $\mathbf{x}_{true}$ (figure 7.4) corresponds to the ground truth image. It is assumed that the measured signal $\mathbf{b}$ is noisy and we have to reconstruct back $\mathbf{x}$ from $\mathbf{b} = \mathbf{A}\mathbf{x}$ .
Signal Model	The term $\mathcal{K}$ in equation 4.25 is ignored here and its influence on the signal will be studied separately in section 7.3. $T_2$ effect is ignored.
SNR	10dB white gaussian complex noise is added to the signal
Image Matrix Size	$65 \times 65$
Angle range and angle step size	$0^\circ - 360^\circ$ with $10^\circ$ step size
No of instances	For each graph, 20 different instances were averaged. This is because reconstructed image is dependent on the noise added for a particular instant, which is statistical in nature.

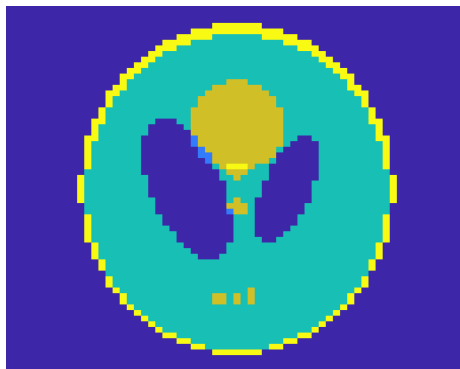


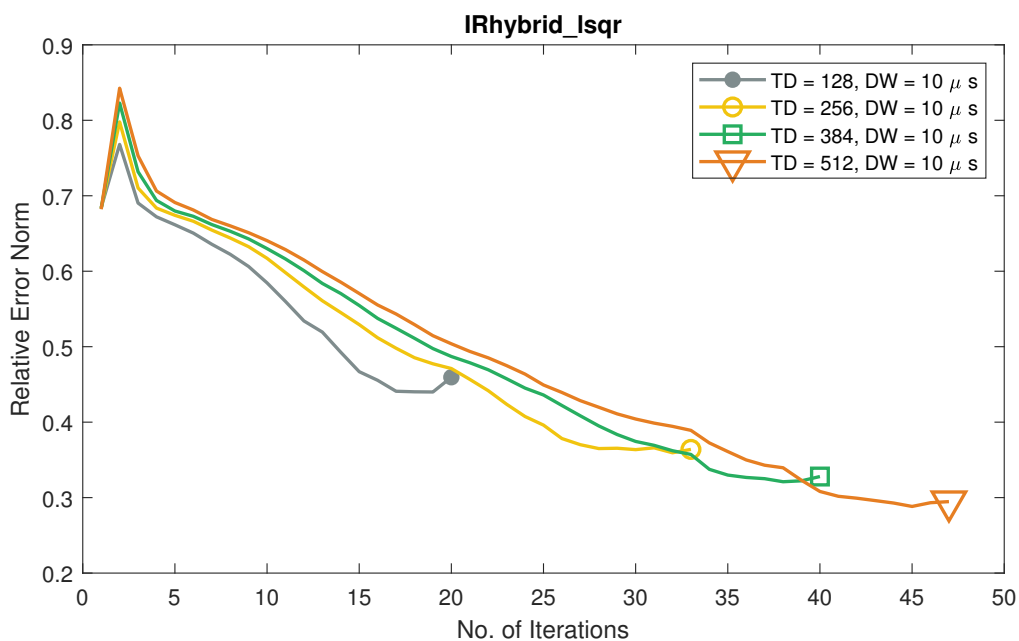
Figure 7.4: Ground truth for the simulations used henceforth in the chapter.

### 7.1.1. Varying TD with Fixed DW

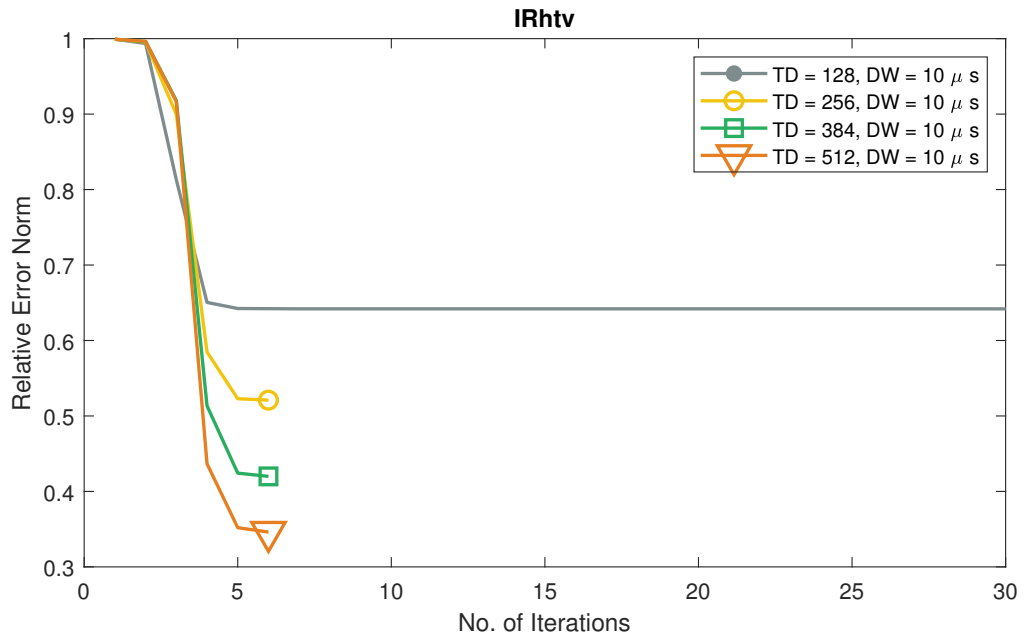
Four graphs of relative error norm versus the number of iterations are plotted by varying TD as 128, 256, 384 and 512 sample points while keeping DW fixed at 10  $\mu$ s. Relative error norm is defined as-

$$\frac{\|\mathbf{x}^{(k)} - \mathbf{x}_{true}\|_2}{\|\mathbf{x}_{true}\|_2}, \quad \text{where, k is the iteration number} \quad (7.3)$$

The results are shown below-



(a)



(b)

Figure 7.5: Relative error norm for fixed DW computed using a) IRhybrid\_lsqr b) IRhtv

For both the algorithms (figure 7.5), IRhybrid\_lsqr and IRhtv, the error norm is seen to decrease as the TD increases. This is because, when the number of sample points increases, higher frequencies in the k-space are considered. This leads to a better resolution of the reconstructed image. In the figure, 7.5, the reconstructed images using IRhybrid\_lsqr look more smooth than the images obtained using IRhtv. This is because the former is based on a 2-norm regularization problem, which tends to smoothen out of the pixels. IRhtv, on the other hand, is based on a 1-norm regularization problem, and it poses less penalty in the jumps of the pixel values. The images that are reconstructed by using it looks more grainy at small TD values. But when the TD is increased, more information is added to the system matrix, and the images look sharper than that of IRhybrid\_lsqr. Table 7.2 summarizes the value of the relative norms of the respective graphs, at the iteration, when the discrepancy principle is satisfied.

Table 7.2: Relative error norm for fixed DW

TD	DW	IRhybrid_lsqr	IRhtv
		Relative Error Norm	Relative Error Norm
128	10 $\mu$ s	0.4595	0.6419
256	10 $\mu$ s	0.3639	0.5209
384	10 $\mu$ s	0.3279	0.4199
512	10 $\mu$ s	0.2947	0.3461

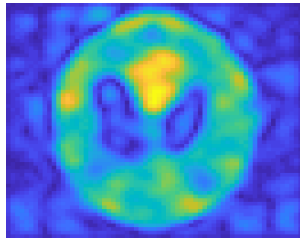
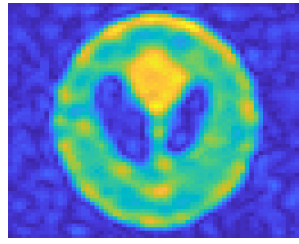
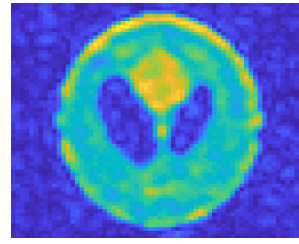
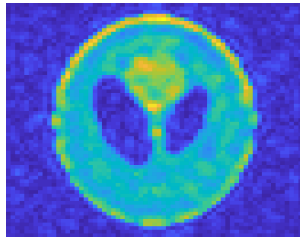
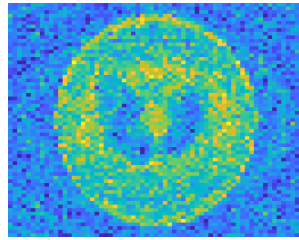
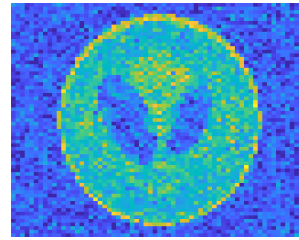
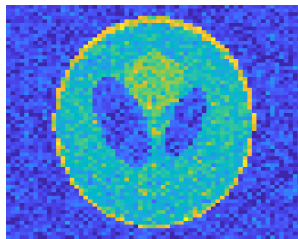
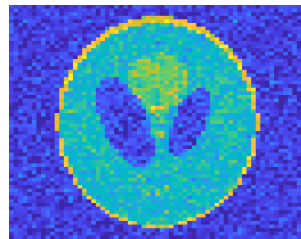
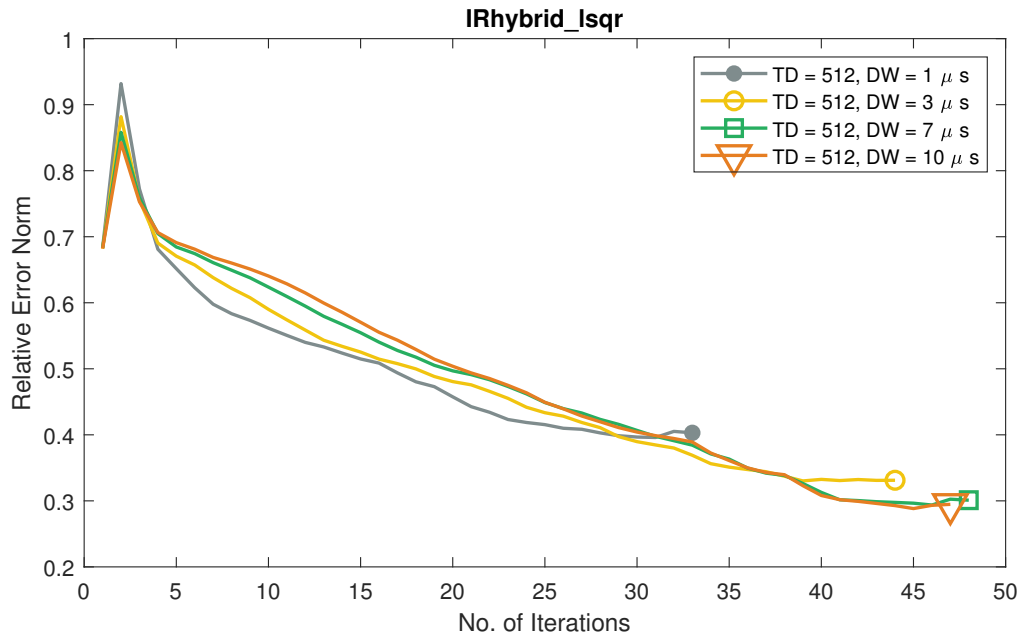
(a)  $TD = 128, DW = 10\mu s$ (b)  $TD = 256, DW = 10\mu s$ (c)  $TD = 384, DW = 10\mu s$ (d)  $TD = 512, DW = 10\mu s$ (e)  $TD = 128, DW = 10\mu s$ (f)  $TD = 256, DW = 10\mu s$ (g)  $TD = 384, DW = 10\mu s$ (h)  $TD = 512, DW = 10\mu s$ 

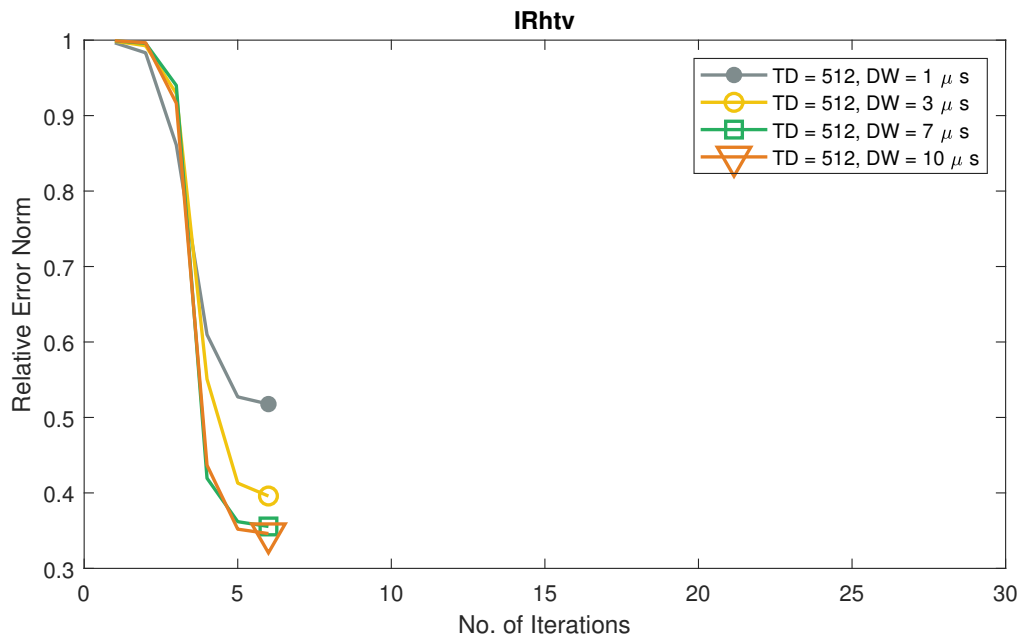
Figure 7.6: Reconstructed image for fixed DW using a)-d) IRhybrid\_lsqr e)-h) IRhtv

### 7.1.2. Varying DW with Fixed TD

Four graphs of relative error norm versus the number of iterations were plotted by varying the DW as  $1\mu s$ ,  $3\mu s$ ,  $7\mu s$  and  $10\mu s$ , while keeping the TD fixed at 512 sample points.



(a)



(b)

Figure 7.7: Relative Error Norm for Fixed TD computed using a) IRhybrid\_Isqr b) IRhtv

In figure 7.7, the value of the error norm decreases with the increase in DW, at the iteration when the discrepancy principle is satisfied. By increasing the dwell time, while keeping the TD fixed, higher frequencies in the k-space are included. Which should increase the resolution. But because of the fixed number of sample points, it also makes the frequencies, sampled at the lower end of k-space, sparser. Depending on the image to be reconstructed, if most of its dominant frequencies lie around the lower end, this will actually lead to a degradation of the reconstruction. In our case, the rate of decrease in error norm became lesser and lesser with the increase in DW. Table 7.3 summarizes the value of the relative

norms of the respective graphs, at the iteration when the discrepancy principle is satisfied.

Table 7.3: Relative Error Norm for Fixed TD

TD	DW	IRhybrid_Isqr	IRhtv
		Relative Error Norm	Relative Error Norm
512	1 $\mu$ s	0.4030	0.5177
512	3 $\mu$ s	0.3312	0.3959
512	7 $\mu$ s	0.3010	0.3555
512	10 $\mu$ s	0.2947	0.3461

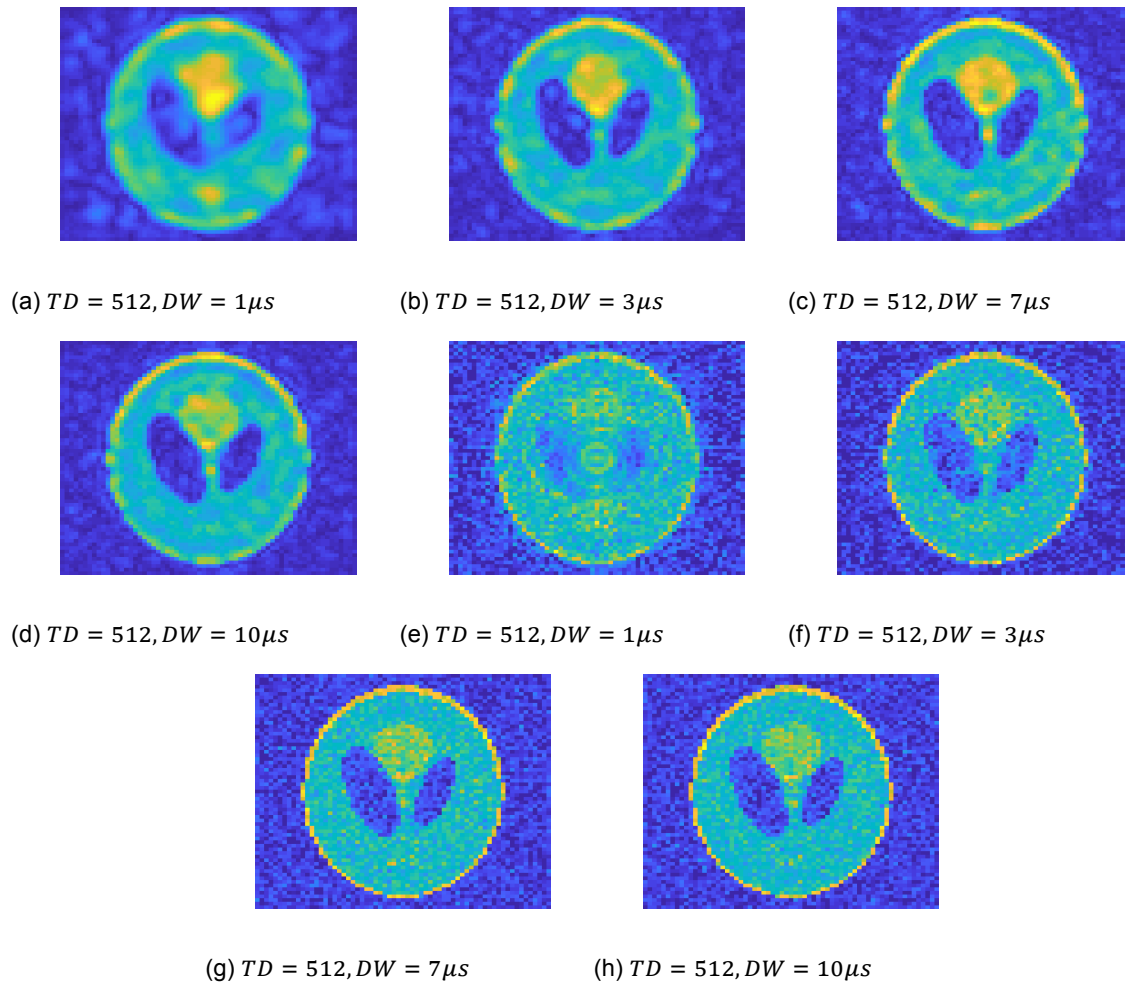


Figure 7.8: Reconstructed image for fixed TD using a)-d) IRhybrid\_Isqr e)-h) IRhtv

It was speculated before that including more time-domain samples under noisy conditions will not be useful. The reasoning for this was that the signals due to the field inhomogeneities die down quickly ( figure 7.9). Thus, the latter part of the signal will be dominated by noise. But it was observed in the simulations that adding time-samples improved the quality of the image. However, a large TD means a large encoding matrix size. This increases the reconstruction computation time and creates memory issues on the computer. Both large TD and DW means longer acquisition time of the patient. It is preferable to minimize the

acquisition time to avoid motion artifacts[14]. For the rest of the simulations, a TD of 516 samples, and a DW of  $10\mu s$  is used. From the visual inspection of this section, it was felt that these values performed satisfactorily, and smaller values resulted in a poorer quality of the image. The values of TD and DW beyond these are not investigated.

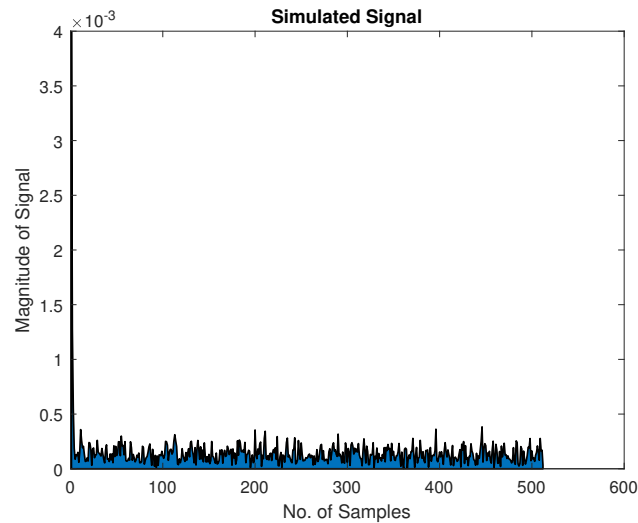


Figure 7.9: Simulated measured signal for  $\theta = 0^\circ$  and  $TD = 512$  time samples. Rest of the parameters used are the same as in table 7.1

## 7.2. Parameter Selection Strategy Investigation

In section 5.3, we had seen two different approaches to select the regularization parameter—the Discrepancy principle and Generalized cross-validation. In this section, we are going to investigate how these methods perform.

### 7.2.1. Discrepancy Principle

We will investigate the discrepancy principle which was discussed in section 5.3.1. This section aims to find out how the reconstruction algorithms using the discrepancy principle perform in a scenario when we do not have a precise knowledge of the noise estimate,  $\epsilon$ . The algorithm using the discrepancy principle requires the user to supply the noise estimates. To investigate the influence of this estimate, it is varied, and the performance of the algorithms is studied using the parameters given in table 7.4.

Table 7.4: Discrepancy principle investigation parameters

Parameters	Choices Used for Simulation
(TD,DW)	(512, 10 $\mu s$ )
Reconstruction Algorithm	1) IRhybrid_lsqr, 2) IRhtv
Maximum Iteration	1) IRhybrid_lsqr: 200, 2) IRhtv: Max inner iteration $\times$ Max outer iteration = 30 $\times$ 30= 900
Parameter Selection Strategy	Discrepancy principle with varying noise estimates
Signal Model	The term $\mathcal{K}$ in equation 4.25 is ignored here and its influence on the signal will be studied separately in section 7.3. $T_2$ effect is ignored.
SNR	10dB white gaussian complex noise is added to the signal
Image Matrix Size	65 $\times$ 65
Angle range and angle step size	0 $^\circ$ – 360 $^\circ$ with 10 $^\circ$ step size
No of instances	20

\*\*For more information about the parameters see table 7.1

### 7.2.1. Visual Inspection

Just by eyeballing the reconstructed images in figure 7.23 and figure 7.11, it is clear that IRhtv is more robust than IRhybrid\_lsqr for the used TD and DW i.e. 512 sample points and 10  $\mu s$  respectively. However, for a lower TD and DW, images reconstructed by IRhtv can be more grainy than IRhybrid\_lsqr (figure 7.6e and figure 7.8e). Moving on, it can be seen that IRhybrid\_lsqr fails to generate meaningful images at around and outside  $\epsilon = 0.1\epsilon_{exact}$  and  $\epsilon = 1.5\epsilon_{exact}$ . Whereas, IRhtv is still able to produce some result at more extremal noise estimates i.e at around  $\epsilon = 0.01\epsilon_{exact}$  and  $\epsilon = 10\epsilon_{exact}$ .

From these visual inspections, surprisingly, the images corresponding to  $\epsilon = 0.901\epsilon_{exact}$ , for both the algorithms, look better than the images corresponding to  $\epsilon = \epsilon_{exact}$ . This is explained as follows. We recollect the discrepancy principle from section 5.3.1 which states-

$$\text{Choose } \lambda \text{ such that } \|\mathbf{Ax}_\lambda^{(k)} - \mathbf{b}\| \geq \eta\epsilon$$

where  $\eta$  is called the safety factor and is there to ensure that the solution norm does not blow up. The default value for it, set by the IRTools package, is  $\eta = 1.01$ . So what we supply as  $\epsilon_{exact}$  to the algorithm gets multiplied by  $\eta$ . In other words, the noise estimate accounted for by the package is slightly greater than what we supply.

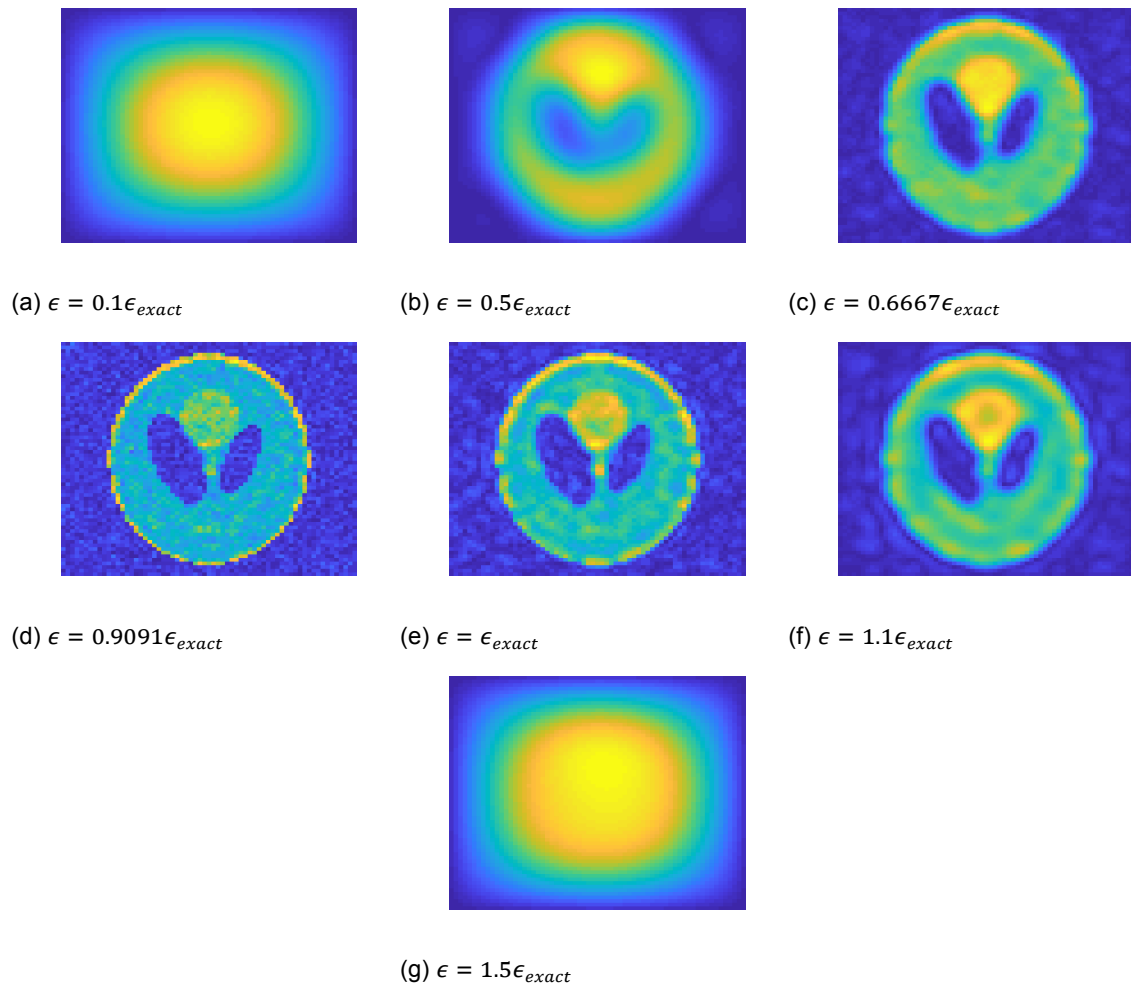
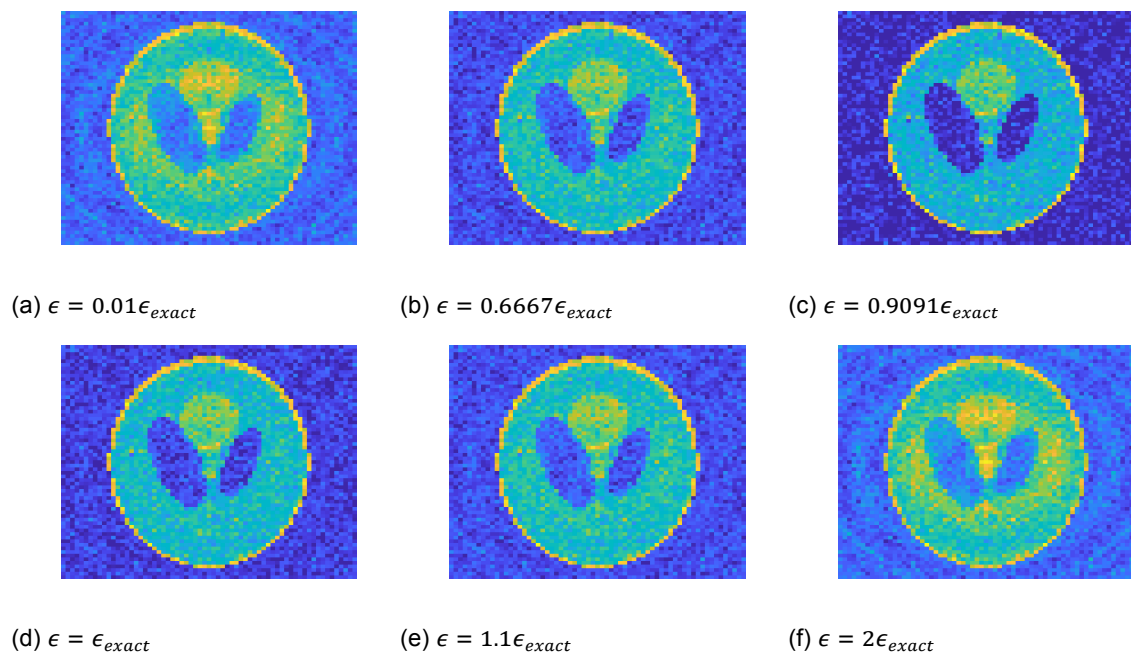


Figure 7.10: Reconstructed image using IRhybrid\_Isqr for different supplied noise estimate



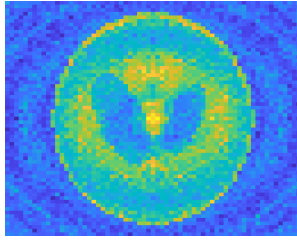
(g)  $\epsilon = 10\epsilon_{exact}$ 

Figure 7.11: Reconstructed image using IRhtv for different supplied noise estimate

### 7.2.1. Computation Time

Table 7.5: Total Computation Time using Discrepancy Principle

Noise Estimate	IRhybrid_lsqr			IRhtv		
	Converging Iteration Number	Total Computation Time (sec)	Computation Time Per Iteration (sec)	Converging Iteration Number	Total Computation Time (sec)	Computation Time Per Iteration (sec)
$0.01\epsilon_{exact}$	—	—	—	60	13.9937	0.2332
$0.1\epsilon_{exact}$	200	465.0186	2.3251	—	—	—
$0.5\epsilon_{exact}$	200	463.7617	2.3188	—	—	—
$0.6667\epsilon_{exact}$	200	463.0410	2.3152	60	12.2770	0.2046
$0.9091\epsilon_{exact}$	91	210.3984	2.3121	900	182.6314	0.2029
$\epsilon_{exact}$	48	111.4957	2.3228	6	1.7751	0.2959
$1.1\epsilon_{exact}$	24	56.2226	2.3426	6	1.7521	0.2920
$1.5\epsilon_{exact}$	200	464.7755	2.3239	—	—	—
$2\epsilon_{exact}$	—	—	—	31	6.4800	0.2090
$10\epsilon_{exact}$	—	—	—	900	346.0417	0.3845

\*\*For IRhybrid\_lsqr, the extremal noise estimates of this table are not investigated. The reason for this is that at around those noise estimates, the reconstructions were not meaningful (Figure 7.23). For IRhtv, certain intermediate cells are left out as the extremal noise estimates corresponding to them were still giving some result (figure 7.11).

Overall, in table 7.5, it is observed that IRhtv takes a much shorter time to converge than IRhybrid\_lsqr. This has to do with the differences between the ways how these algorithms handle the regularization matrix,  $\mathbf{L}$ . This was discussed in section 6.9. IRhtv reduces the  $\mathbf{L}$  matrix and considers  $\mathbf{R}_k$ , whose dimension is much less than  $\mathbf{L}$ . This way, this algorithm becomes faster than IRhybrid\_lsqr which does not reduce  $\mathbf{L}$ .

#### 7.2.1. Relative Residual Norm Versus Number of Iterations

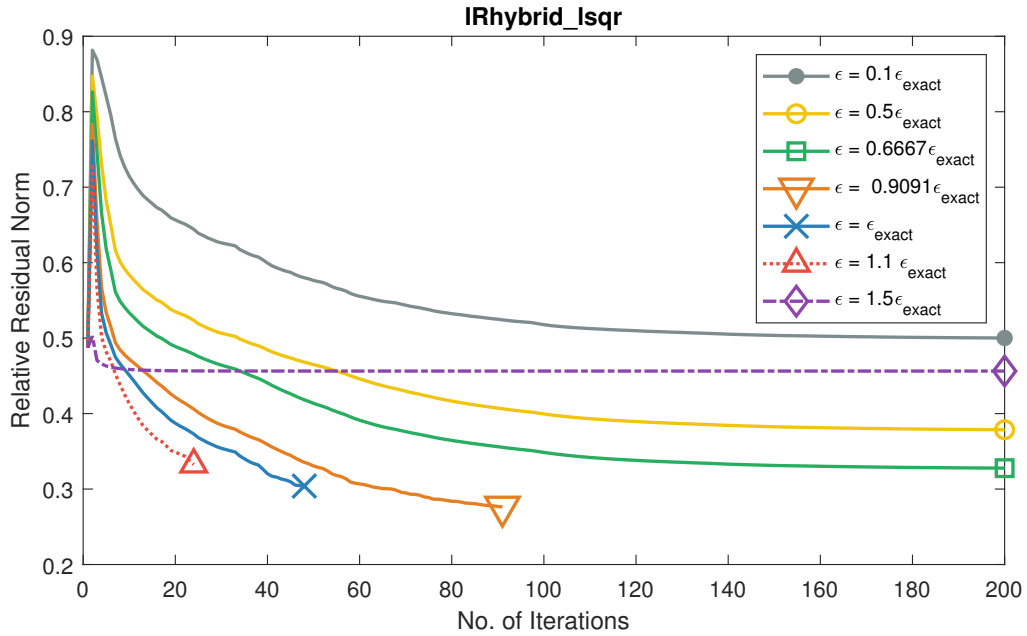
Relative residual error is defined as-

$$\frac{\|\mathbf{b} - \mathbf{Ax}^{(k)}\|_2}{\|\mathbf{b}\|_2}, \quad \text{where, } k \text{ is the iteration number} \quad (7.4)$$

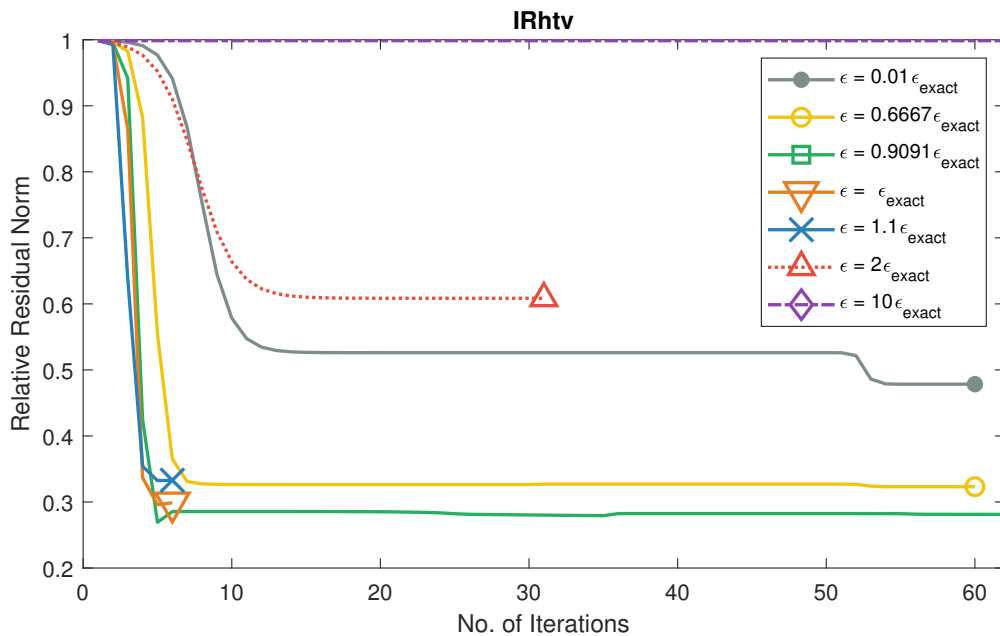
This term is closely related to the discrepancy principle, as we can see from the expression it involves. So the discrepancy principle implies that the algorithm is stopped when a desired residual error is achieved. From figure 7.12, it can be seen that the graph of the relative residual gets higher and higher as we deviate away from the correct noise estimate. This can be explained as follows. The Secant rule (equation 6.24) suggests the regularization parameter for the next iteration as an attempt to match the noise estimate to the residual error. If

the noise estimate is not correct, it cannot match the residual error, and therefore, it keeps on suggesting wrong regularization parameters. These wrong regularization parameters, in turn, lead to a higher residual error.

We also notice that the residual error for IRhtv and IRhybrind\_lsqr cannot be directly compared. For example, for IRhtv, in case of  $\epsilon = 10\epsilon_{exact}$ , even though the residual error is worse than the worst result of IRhybrid\_lsqr shown here, its solution is visually still meaningful (figure 7.23 and figure 7.11).



(a)



(b)

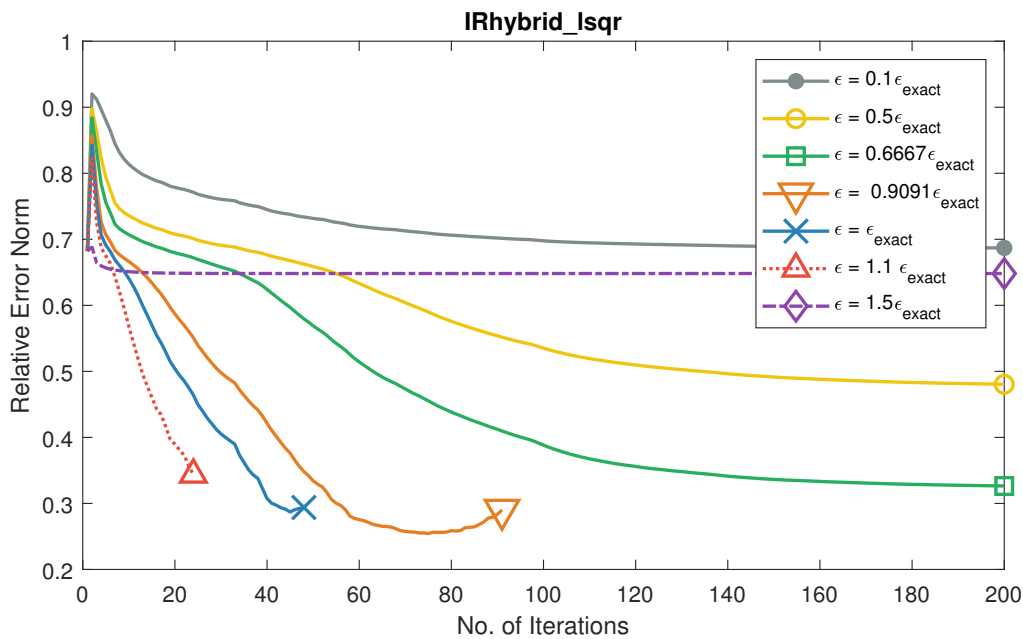
Figure 7.12: Relative Residual Norm for investigation of discrepancy principle computed using a) IRhybrid\_lsqr b) IRhtv

Table 7.6: Relative Residual Norm for investigation of Discrepancy Principle

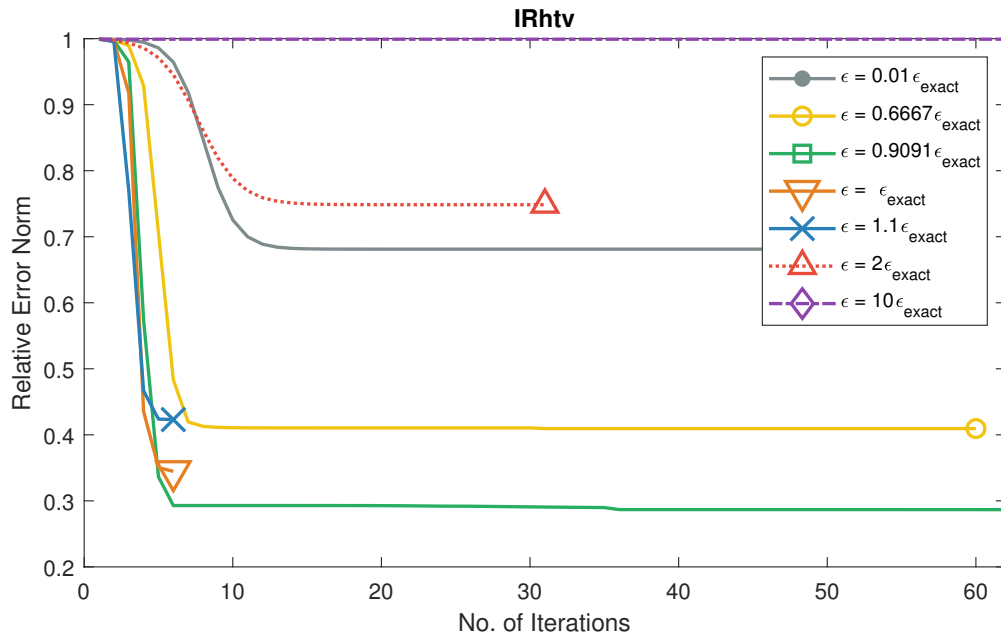
Noise Estimate	IRhybrid_Isqr	IRhtv
	Relative Residual Norm	Relative Residual Norm
$0.01\epsilon_{exact}$	—	0.4784
$0.1\epsilon_{exact}$	0.5001	—
$0.5\epsilon_{exact}$	0.3786	—
$0.6667\epsilon_{exact}$	0.3277	0.3231
$0.9091\epsilon_{exact}$	0.2764	0.2814
$\epsilon_{exact}$	0.3040	0.2988
$1.1\epsilon_{exact}$	0.3325	0.3329
$1.5\epsilon_{exact}$	0.4564	—
$2\epsilon_{exact}$	—	0.6085
$10\epsilon_{exact}$	—	0.9984

### 7.2.1. Relative Error Norm Versus Number of Iterations

The error norm plot (figure 7.13) shown for the graphs follows from the residual norm plot. As seen here, lower residual norm implied lower error norm in our case. This, in turn, shines a light on the quality of the signal model ( or system matrix) used here. If the signal model describes the physical process well, such that it leads to a solution in the vicinity of the real solution, the reduction of residual norm leads to the reduction of error norm.



(a)



(b)

Figure 7.13: Relative Error Norm for investigation of discrepancy principle computed using a) IRhybrid\_lsqr b) IRhtv

Table 7.7: Relative Error Norm for investigation of Discrepancy Principle

Noise Estimate	IRhybrid_lsqr	IRhtv
	Relative Error Norm	Relative Error Norm
$0.01\epsilon_{exact}$	—	0.6812
$0.1\epsilon_{exact}$	0.6870	—
$0.5\epsilon_{exact}$	0.4804	—
$0.6667\epsilon_{exact}$	0.3264	0.4094
$0.9091\epsilon_{exact}$	0.2901	0.2836
$\epsilon_{exact}$	0.2939	0.3447
$1.1\epsilon_{exact}$	0.3435	0.4231
$1.5\epsilon_{exact}$	0.6482	—
$2\epsilon_{exact}$	—	0.7485
$10\epsilon_{exact}$	—	0.9990

### 7.2.1. Regularization Parameter Versus Number of Iterations

The IRtools package outputs the evolution of the regularization parameter with iterations only for IRhybrid\_lsqr and not IRhtv. As a result, the plot for only IRhybrid\_lsqr is shown here (figure 7.14). We can refer from the plot 7.14 that when the noise estimates are not correct, the discrepancy principle keeps on suggesting the regularization parameter as an attempt to match the noise estimate and residual error. For the noise estimates that are nearer to correct estimate, after certain iterations, no or little regularization is required.

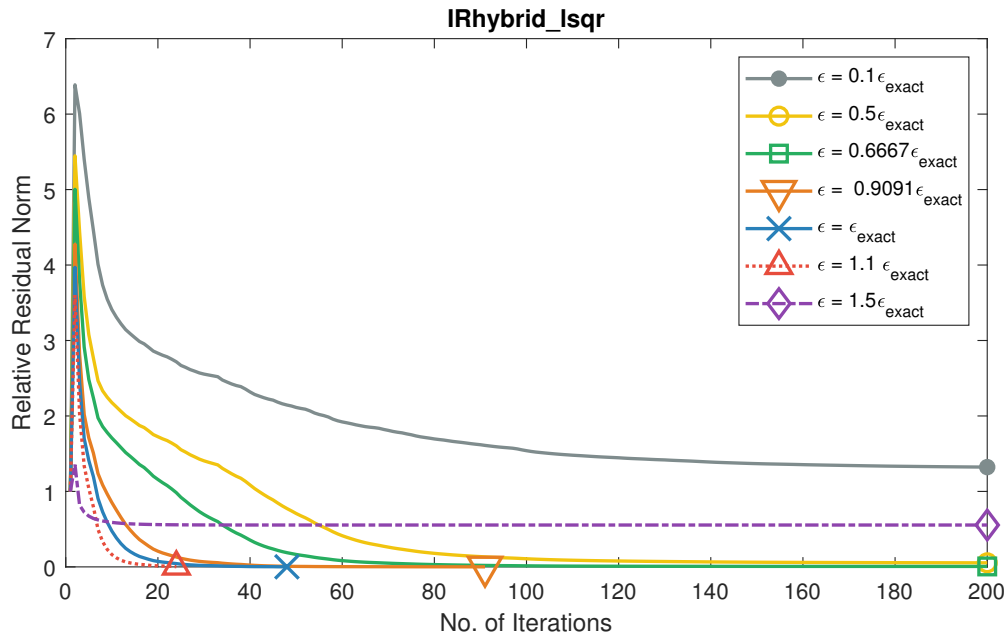


Figure 7.14: Regularization parameter vs No of Iterations for IRhybrid\_Isqr

### 7.2.2. General Cross Validation

The general cross-validation parameter selection strategy from section 5.3.2 is investigated here using the parameter given in table 7.8. It was mentioned that in order to speed up the computations, the bi-diagonal matrix  $\mathbf{B}_k$  of much smaller dimension is used rather than  $\mathbf{A}$ . One downside of this is that if  $\mathbf{A}$  is ill-conditioned, or there are rounding errors in computing  $\mathbf{B}_k$ , GCV performs poorly. [4] discusses that GCV often tend to overestimate the regularization parameters. Reorthogonalization can be done to reduce the error but it increases the computation time. As an attempt to improve the estimation process, the authors of [4] proposed the weighted-GCV or WGCV. It is clear from the WGCV function (equation 5.10) that GCV is WGCV with  $w = 1$ . Smaller  $w$  tends to find smaller regularization parameters, while larger  $w$  finds larger regularization parameters. Simulation parameters for this examination is provided in table 7.8.

Table 7.8: GCV investigation parameters

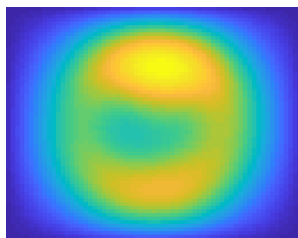
Parameters	Choices Used for Simulation
(TD,DW)	(512, 10 $\mu$ s)
Reconstruction Algorithm	1) IRhybrid_lsqr, 2) IRhtv
Maximum Iteration	1) IRhybrid_lsqr: 200, 2) IRhtv: Max inner iteration $\times$ Max outer iteration = 30 $\times$ 30= 900
Parameter Selection Strategy	General Cross Validation (Weighted)
Signal Model	The term $\mathcal{K}$ in equation 4.25 is ignored here and its influence on the signal will be studied separately in section 7.3. $T_2$ effect is ignored.
SNR	10dB white gaussian complex noise is added to the signal
Image Matrix Size	65 $\times$ 65
Angle range and angle step size	0 $^\circ$ – 360 $^\circ$ with 10 $^\circ$ step size
No of instances	20

\*\*For more information about the parameters see table 7.1.

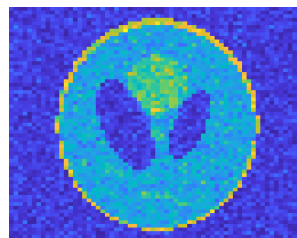
### 7.2.2. Visual Inspection

[4] proposes an adaptive way to compute  $w$ , where  $0 \leq w \leq 1$ . Visual inspection of figure 7.15 reveals that, in our case, only  $w = 0$  is giving results. The rest of them are oversmoothed (indicating high  $\lambda$  parameter selection).

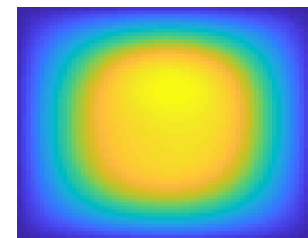
For IRhtv, in figure 7.16,  $w = 1$  seems to give some result while  $w = 'adapt'$  appears to give very good reconstruction. This difference can be mainly attributed to the 1-norm regularization of IRhtv. As a side note, in the IRTools package, any other weight value for IRhtv is not supported when using WGCV.



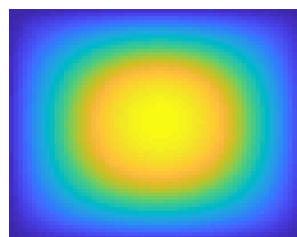
(a) WGCV with  $w = 'adapt'$



(b) WGCV with  $w = 0$

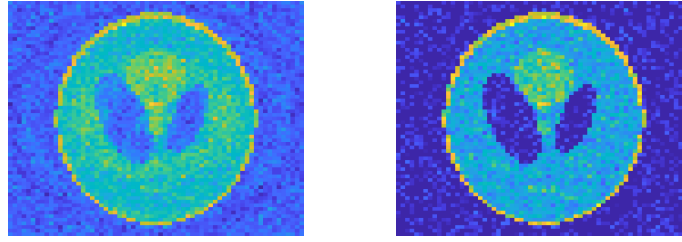


(c) WGCV with  $w = 0.5$



(d) WGCV with  $w = 1$

Figure 7.15: Reconstructed image using WGCV with different weights,  $w$ , using IRhybrid\_lsqr.



(a) GCV or WGCV with  $w = 1$       (b) WGCV with  $w = \text{'adapt'}$

Figure 7.16: Reconstructed image using WGCV with different weights,  $w$ , using IRhtv.

### 7.2.2. Computation Time

Comparing table 7.5 and table 7.9, it can be seen that the computation time using GCV is in general larger than using discrepancy principle when the supplied noise estimates are around the correct noise estimate. This is because when the encoding matrix becomes large, the computation of SVD in GCV becomes expensive. Thus, for larger matrices, the discrepancy principle is desirable. GCV is useful when we do not have knowledge of an appropriate noise estimate to supply to algorithms using the discrepancy principle.

In a scenario where the noise level does not change, the author proposes to use WGCV/GCV to obtain the reconstructed image. This reconstructed image can then be used to get a rough estimate of noise level, which can then be used with the discrepancy principle to get a shorter computation time. This approach can be summarized below-

1. **Step 1:** Use WGCV/GCV to obtain a reconstructed image,  $\mathbf{x}_{GCV}$ .
2. **Step 2:** Use  $\mathbf{x}_{GCV}$  to get a rough estimate of noise,  $\epsilon_{rough}$ , by using  $\epsilon_{rough} = \|\mathbf{Ax}_{GCV} - \mathbf{b}\|_2$
3. **Step 3:** Use this rough noise estimate,  $\epsilon_{rough}$ , in discrepancy principle, in the case when no knowledge about the estimate is available. Then the noise estimate can be fine tuned from there to improve the result.

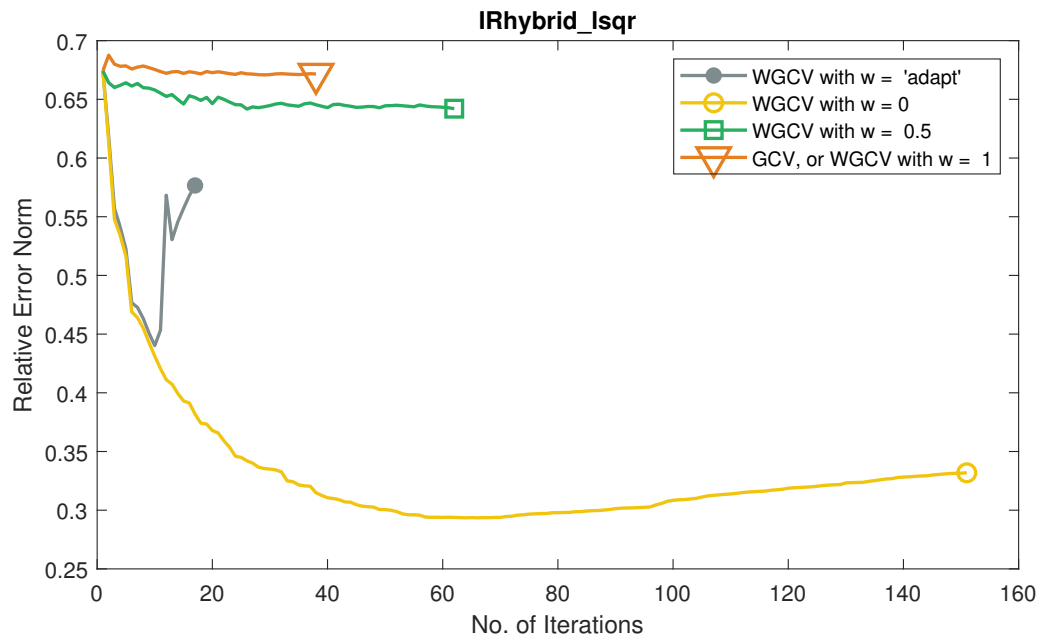
Table 7.9: Total Computation Time using Discrepancy Principle

WGCV Weights ( $w$ )	IRhybrid_lsqr			IRhtv		
	Converging Iteration Number	Total Computation Time (sec)	Computation Time Per Iteration (sec)	Converging Iteration Number	Total Computation Time (sec)	Computation Time Per Iteration (sec)
'adapt'	17	101.6606	5.9800	60	16.3498	0.2725
1	151	806.2257	5.3392	795	255.1532	0.3209
0.5	62	323.6767	5.2206	—	—	—
0	38	221.7118	5.8345	—	—	—

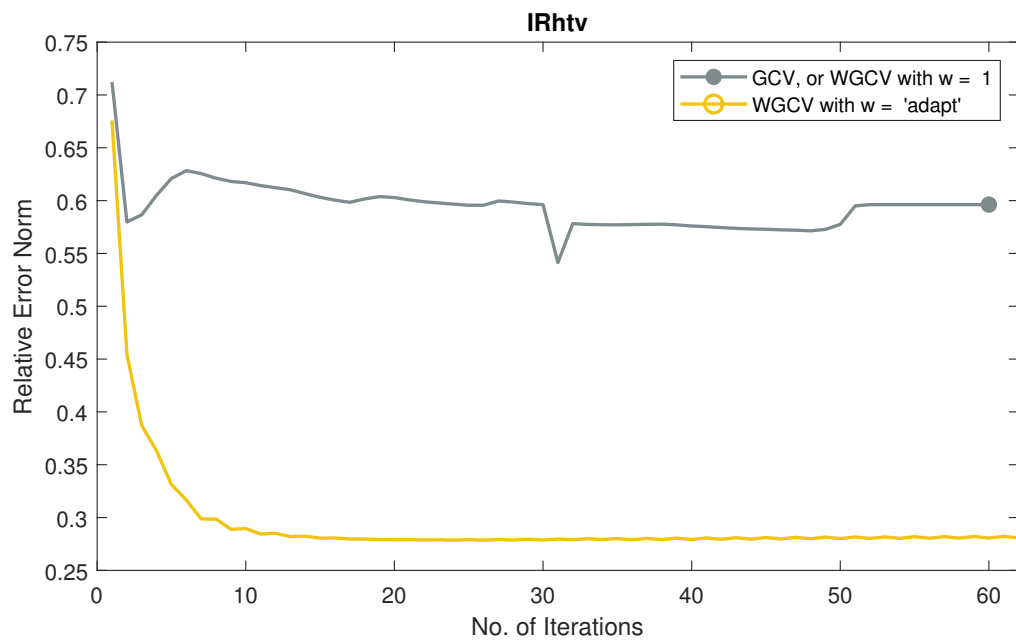
\*\*For IRhtv, the cells that are left blank corresponds to WGCV weights that are not supported by IRTools package.

### 7.2.2. Relative Error Norm Versus Number of Iterations

As expected, in figure 7.17, graph corresponding to the oversmoothed images have high errors.



(a)



(b)

Figure 7.17: Relative Error Norm for investigation of discrepancy principle computed using a) IRhybrid\_Isqr b) IRhtv

Table 7.10: Relative Error Norm for the investigation of Dcrepancy Principle

WGCV Weights (w)	IRhybrid_lsqr	IRhtv
	Relative Error Norm	Relative Error Norm
'adapt'	0.5766	0.5962
1	0.3319	0.2839
0.5	0.6420	—
0	0.6716	—

### 7.2.2. GCV Values Versus Number of Iterations

IRhtv in IRTools does not support outputting the GCV values. So only the plot corresponding to IRhybrid\_lsqr is shown in figure 7.18. The stopping criteria of GCV is when GCV values change very little[4]. There is one second stopping criteria for GCV to counter the scenario when it is not possible to completely stabilize the GCV values. Here, the algorithm is stopped at that iteration when GCV is the least[4].

From the expression of GCV function (or WGCV) minimization problem, it can be implied that lower GCV values mean better regularization parameter estimation. The graph of GCV values for WGCV with  $w = 0$  is seen to decrease with iterations. It is not the case for the other graphs.

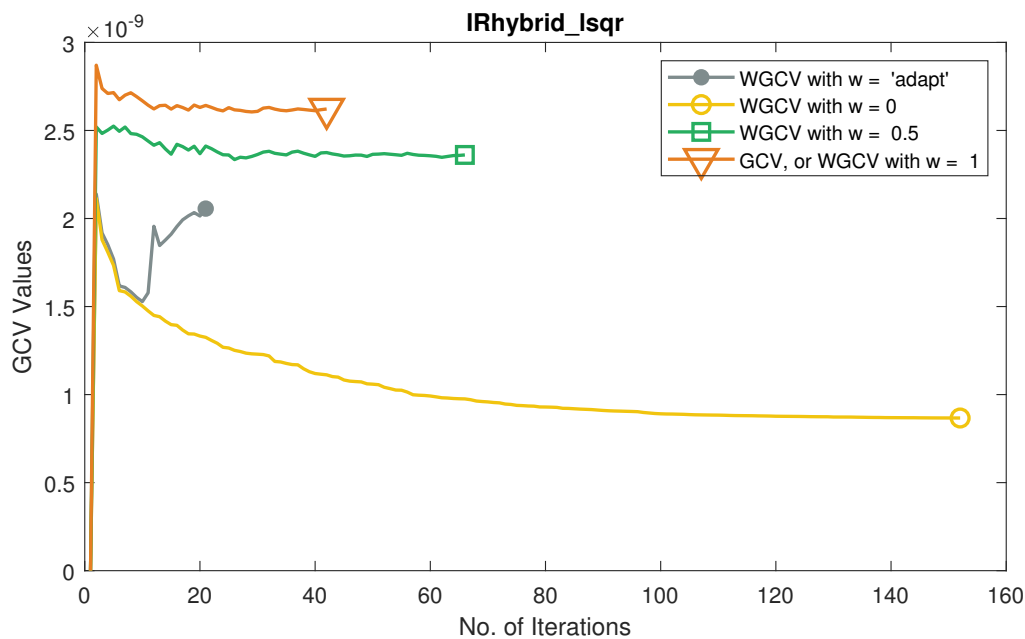


Figure 7.18: GCV values vs No of Iterations for IRhybrid\_lsqr

### 7.2.2. Regularization Parameter Versus Number of Iterations

Like in the previous investigation, IRhtv in IRTools does not support outputting the regularization parameters. So only the plot corresponding to IRhybrid\_lsqr is shown in figure 7.19. It is seen that for WGCV with  $w = 0$ , the regularization parameter quickly decays towards 0. This implies no or little regularization is needed.

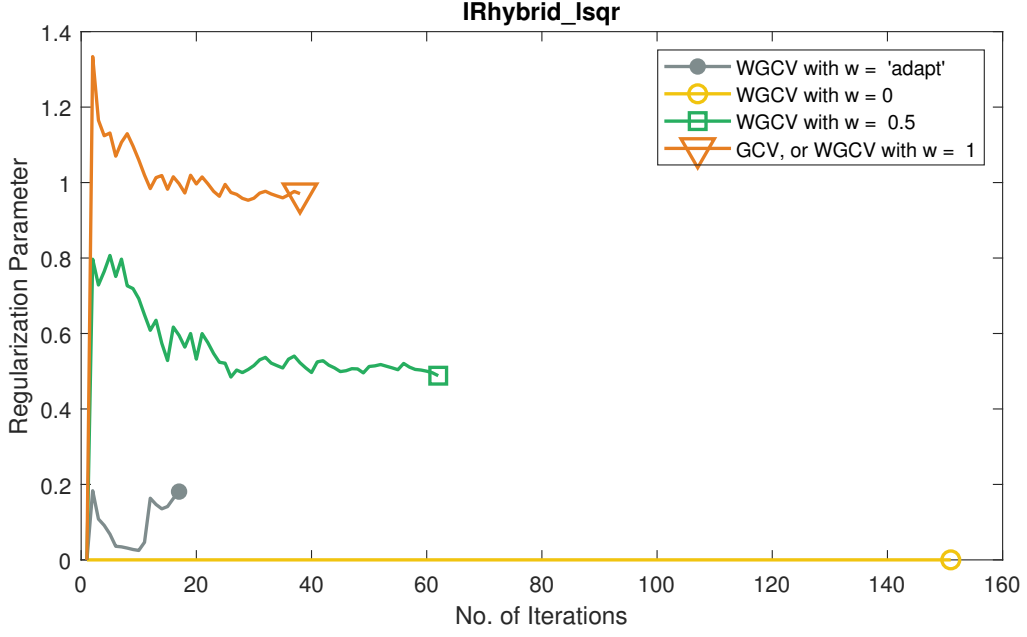


Figure 7.19: Regularization parameter vs No of Iterations for IRhybrid\_Isqr

### 7.3. Signal Model for Rotating MRI Investigation

So far, we had been ignoring the  $\mathcal{K}$  term in our signal model in the previous investigations. This section uses the complete signal model as given in equation 4.25 (written again in equation 7.5 below) and aspires to study the influence of  $\mathcal{K}$ . How this study is done is described next. In the signal model below

$$d(t; \theta) = \int_{\mathbf{r} \in \mathbb{D}_{\text{samp}}} \rho(\mathbf{r}) \mathcal{K}(\mathbf{r}; \theta) e^{-p(\mathbf{r}; \theta)t} d\mathbf{r} \quad (7.5)$$

$\mathcal{K}$  is given by

$$\mathcal{K}(\mathbf{r}; \theta) = -i \frac{\gamma \hbar^2}{4KT_S} \mathcal{M}_+^{0+}(\mathbf{r}; \theta) \mathcal{B}_-(\mathbf{r}; \theta) \omega_0^2$$

where,

$$\begin{aligned} \mathcal{B}_-(\mathbf{r}; \theta) &= B_{r,\theta-} = [B_{r,\theta,x\theta}] - i[B_{r,\theta,y\theta}] \\ &= [\cos(\theta)B_{r,x}(\mathbf{r}) - \sin(\theta)B_{r,z}(\mathbf{r})] - i[B_{r,y}(\mathbf{r})] \end{aligned} \quad (7.6)$$

and,

$$\begin{aligned} \mathcal{M}_+^{0+}(\mathbf{r}; \theta) &= M_{\theta+}^{0+} = [M_{\theta,x\theta}^{0+}] + i[M_{\theta,y\theta}^{0+}] \\ &= [M_x^{0+}(\mathbf{r})\cos(\theta) - M_z^{0+}(\mathbf{r})\sin(\theta)] + i[M_y^{0+}(\mathbf{r})] \\ &= [M_{eq}\mathcal{M}_x^{0+}(\mathbf{r})\cos(\theta) - M_{eq}\mathcal{M}_z^{0+}(\mathbf{r})\sin(\theta)] + i[M_{eq}\mathcal{M}_y^{0+}(\mathbf{r})] \end{aligned} \quad (7.7)$$

To make a connection between these equations, and that of chapter 2, we recall section 2.6. The magnetization components, for on-resonance excitations, after an RF pulse of duration  $t = \tau_p$ , can be described as-

$$\begin{aligned} M_{\hat{x}}(\tau_p) &= 0 \\ M_{\hat{y}}(\tau_p) &= M_z^0 \sin(\omega_1 \tau_p) \\ M_{\hat{z}}(\tau_p) &= M_z^0 \cos(\omega_1 \tau_p) \end{aligned} \quad (7.8)$$

Note that the equation 7.8 is the solution of the Bloch's equation when the equilibrium magnetization points directly towards  $\vec{\mathbf{k}}$  direction and the magnetizations are flipped about  $\vec{\mathbf{i}}$  axis. Comparing equation 7.8 to equation 7.7, we find-

$$\begin{aligned} M_x^{0+}(\vec{\mathbf{r}}) &= M_{eq} \mathcal{M}_x^{0+}(\vec{\mathbf{r}}) = M_x(\tau_p) = 0 \\ \Rightarrow \mathcal{M}_x^{0+}(\vec{\mathbf{r}}) &= 0 \end{aligned} \quad (7.9)$$

and similarly,

$$\mathcal{M}_y^{0+}(\vec{\mathbf{r}}) = \sin(\omega_1 \tau_p; \vec{\mathbf{r}}) \quad \text{and} \quad \mathcal{M}_z^{0+}(\vec{\mathbf{r}}) = \cos(\omega_1 \tau_p; \vec{\mathbf{r}}) \quad (7.10)$$

If we assume that an RF pulse, having a band of frequencies, is applied such that the magnetization throughout the object is flipped with a flip angle  $\alpha = \omega_1 \tau_p$ , the expression of  $\mathcal{M}_+^{0+}$  becomes-

$$\mathcal{M}_+^{0+}(\vec{\mathbf{r}}; \theta) = -M_z^0 \cos(\alpha) \sin(\theta) + i M_z^0 \sin(\alpha) \quad (7.11)$$

For  $B_-$ , we assume that it is uniform everywhere and is pointing directly along  $\vec{\mathbf{j}} = \vec{\mathbf{j}} = \vec{\mathbf{j}}_\theta$  axis. Then we have-

$$\begin{aligned} B_-(\vec{\mathbf{r}}; \theta) &= \cos(\theta) B_{r,x}(\vec{\mathbf{r}}) - \sin(\theta) B_{r,z}(\vec{\mathbf{r}}) - i B_{r,y}(\vec{\mathbf{r}}) \\ &= \quad 0 \quad - \quad 0 \quad - \quad i s \quad (\text{s is some scalar}) \\ &= -i \quad (\text{We can ignore the scalar, s, as} \\ &\quad \text{it will just scales the reconstructed image}) \end{aligned} \quad (7.12)$$

Our signal model thus becomes-

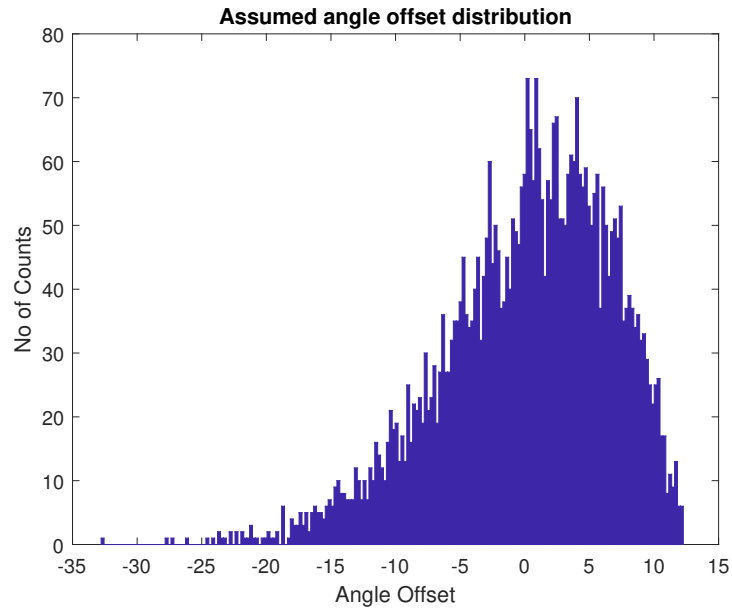
$$\begin{aligned} d(t; \theta) &= \int_{\mathbf{r} \in \mathbb{D}_{samp}} \rho(\vec{\mathbf{r}}) \mathcal{K}(\vec{\mathbf{r}}; \theta) e^{-p(\vec{\mathbf{r}}; \theta)t} d\mathbf{r} \\ &= \int_{\mathbf{r} \in \mathbb{D}_{samp}} \rho(\vec{\mathbf{r}}) (-\cos(\alpha) \sin(\theta) + i \sin(\alpha)) (-i) e^{-p(\vec{\mathbf{r}}; \theta)t} d\mathbf{r} \quad (\text{Ignoring the scalar constants} \\ &\quad \text{after plugging in equation 2.9}) \end{aligned} \quad (7.13)$$

We can observe that for a 90° degree pulse this model becomes-

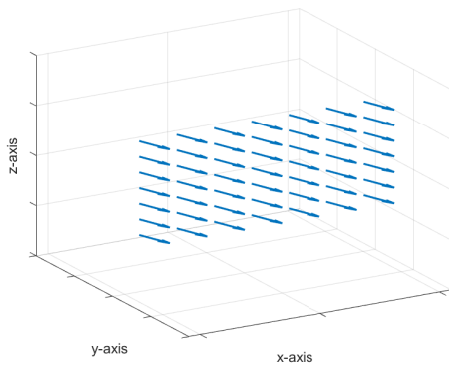
$$d(t; \theta) = \int_{\mathbf{r} \in \mathbb{D}_{samp}} \rho(\vec{\mathbf{r}}) e^{-p(\vec{\mathbf{r}}; \theta)t} d\mathbf{r} \quad (7.14)$$

Which is the same model that we used in previous investigations when  $\mathcal{K}$  was ignored. For any other flip angle, the signal model of equation 7.13 will be different than the aforementioned model.

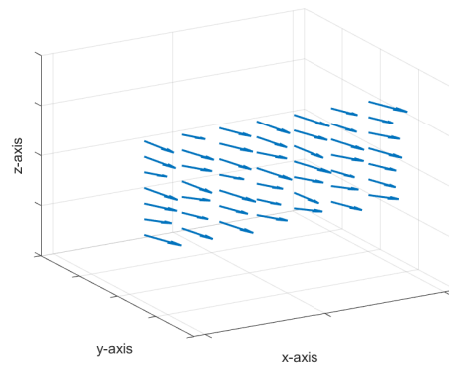
In the introduction of chapter 6, it was discussed that we use the rotating MRI machine to encode the object to be imaged into measured signals. Once we have this signal, we swap an equivalent mathematical model with the actual system and use it to reconstruct the image. In practice, during the encoding process, the exact flip angles of the magnetization throughout the object are not known. We try to reconstruct the image assuming that the RF pulse applied to the object has resulted in an intended flip angle (nominal flip angle). To simulate these unknown magnetization flip angles that arise due to the off-resonance effects of the field inhomogeneities, we further rotate the flipped magnetizations about x, y, and z-axis by some angle offset (figure 7.20c). These offsets are chosen from a Rayleigh distribution and are based purely on the assumption that most of the flip angles will be centered around the nominal flip angle. The spread of flip angles, that are less than the nominal flip angle, is assumed to be more than those that are more than the nominal one (figure 7.20a). Investigation of more appropriate offset distribution can be done in future work. Moving on, we will refer to this as 'angle noise' to differentiate it from the white gaussian complex noise that is added to the signal to simulate noise from unknown factors. We then tried to reconstruct back the image using a model without angle noise but with a known nominal flip angle.



(a)



(b)



(c)

Figure 7.20: a) Assumed Rayleigh distribution of the angle offset. b)-c) shows the flipped magnetizations where b) no angle noise is added c) angle noise is added. Magnetizations are flipped by  $45^\circ$  when  $\theta = 0^\circ$ , in this figure.

The results of this investigation is discussed next.

### 7.3.1. Influence of Angle noise and Flip Angles

In this section, we assume that applying RF pulses to the magnetizations has resulted in a flip angle distribution with a mean of around the intended flip angle. For example, suppose, if we have transmitted a  $60^\circ$  pulse to the object, it has actually resulted in a flip angle distribution with a mean of around  $60^\circ$ . The objective of this section is two folds-

1. **Angle Noise Distribution Spread:** It investigates the reconstructed signal when the angle noise spread is increased by choosing a higher shape parameter,  $\sigma$ . The angle noise distributions that is tested here is visualized in figure 7.21.

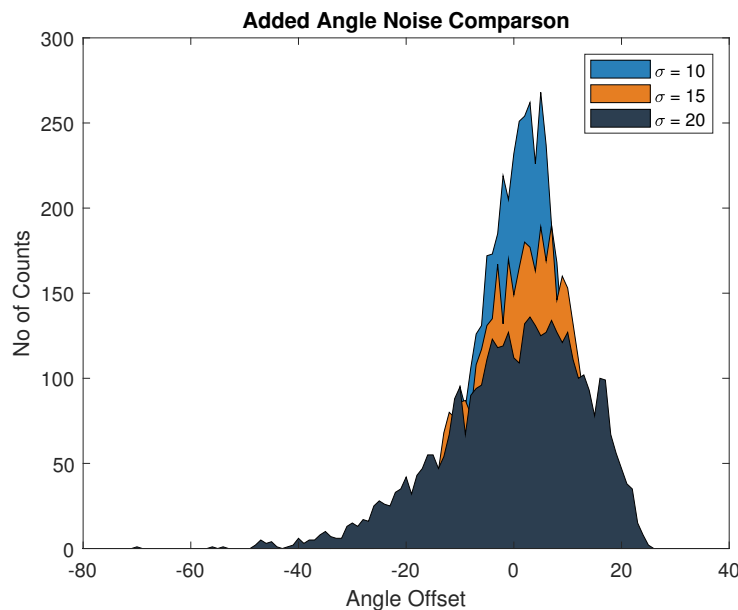


Figure 7.21: Histogram of added angle noise comparison

2. **Flip Angles:** It investigates the reconstructed signal for different flip angles. The simulation parameters are provided in table 7.11.

Table 7.11: Signal model investigation parameters

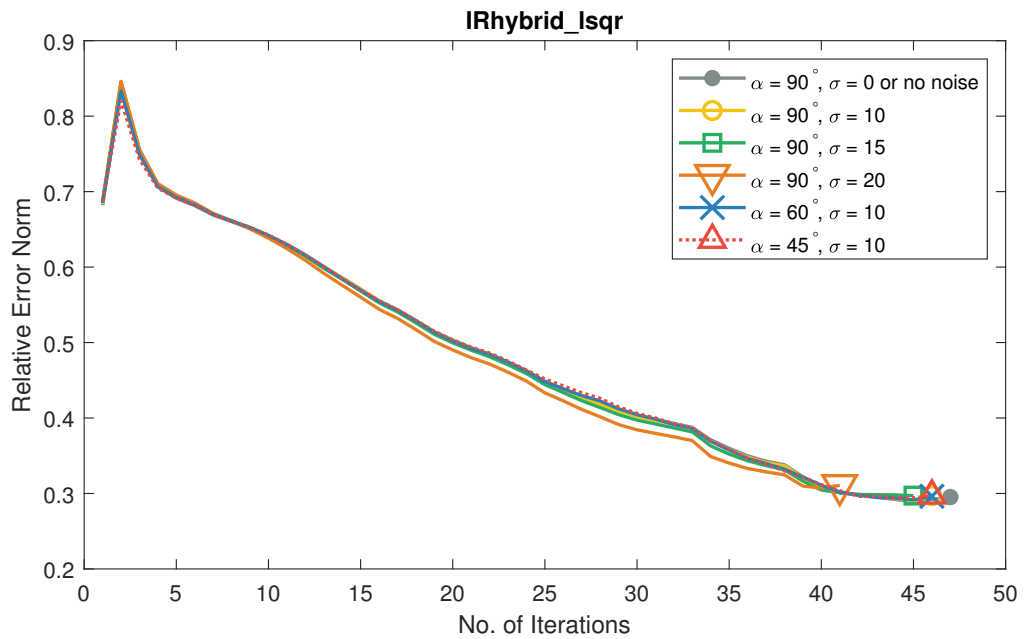
Parameters	Choices Used for Simulation
(TD,DW)	(512, 10 $\mu$ s)
Reconstruction Algorithm	1)IRhybrid_lsqr, 2)IRhtv
Maximum Iteration	1) IRhybrid_lsqr: 200, 2) IRhtv: Max inner iteration $\times$ Max outer iteration = 30 $\times$ 30= 900
Parameter Selection Strategy	Discrepancy principle with exact noise estimate.
Signal Model	The complete model, as in equation 4.25, is investigated. More information will be apparent from this section. $T_2$ effect is ignored.
SNR	10dB white gaussian complex noise is added to the signal.
Angle Noise	1) No angle noise, 2)Magnetizations that were flipped by $\alpha$ angle were rotated by some angle offset about x-axis, y-axis and z-axis. These offsets were chosen from a Rayleigh's distribution with probability distribution function- $\frac{x}{\sigma^2} e^{-\frac{x^2}{2\sigma^2}}$ , where $x$ is a random variable and $\sigma$ is called the shape parameter.
Image Matrix Size	65 $\times$ 65
Angle range and angle step size	0 $^\circ$ – 360 $^\circ$ with 10 $^\circ$ step size
No of instances	20

\*\*For more information about the parameters see table 7.1.

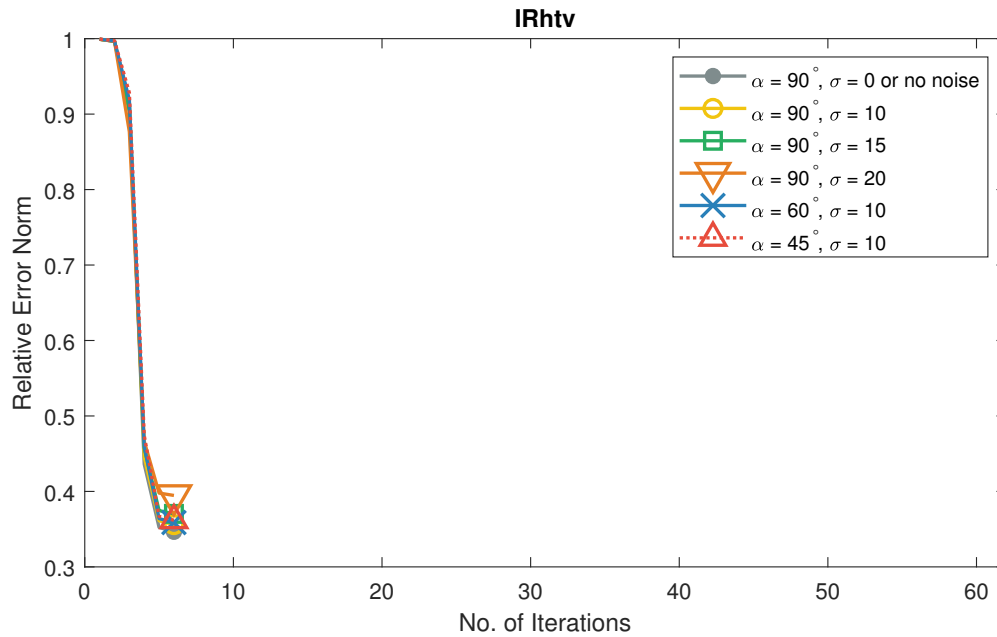
### 7.3.1. Relative Error Norm Versus Number of Iterations

The visual inspection was skipped here because they all look quite similar, and it was difficult to conclude anything just by eyeballing. From the relative error norm plot in figure 7.22, we consider the first four graphs in the legend. Here, we observe that with the increase in the angle noise spread the error increases. This spread depends upon the off-resonance effects due to the field inhomogeneities of the field map, and the selected RF pulse frequencies. We need the inhomogeneities to encode the spatial information, and thus, the angle noise spread will always be there.

Next, if we consider the 2<sup>nd</sup>, 5<sup>th</sup> and 6<sup>th</sup> graph in the legend of the plot in figure 7.22, we see that they all perform similarly. Thus if the spread is not too much, then the addition of angle noise does not cause serious degradation as long as the nominal flip angle is around the mean of the distribution of the actual flip angles.



(a)



(b)

Figure 7.22: Relative Error Norm for investigation of signal model using a) IRhybrid\_Isqr b) IRhtv

Table 7.12: Relative Error Norm for investigation of signal model

Signal Model Parameter	IRhybrid_Isqr	IRhtv
	Relative Error Norm	Relative Error Norm
$\alpha = 90^\circ, \sigma = 0$ or no noise	0.2953	0.3465
$\alpha = 90^\circ, \sigma = 10$	0.2970	0.3560
$\alpha = 90^\circ, \sigma = 15$	0.2972	0.3702
$\alpha = 90^\circ, \sigma = 20$	0.3108	0.3947
$\alpha = 60^\circ, \sigma = 10$	0.2963	0.3588
$\alpha = 45^\circ, \sigma = 10$	0.2971	0.3618

### 7.3.2. Influence of Wrong Flip Angles

Unlike the last investigation, now we assume that applying RF pulses to the magnetizations has not resulted in a desired flip angle. However, we do not know this, and we proceed to reconstruct the signal using the flip angle we think it is. For example, we try to reconstruct a signal using  $90^\circ$  in our signal model, which was actually encoded due to magnetizations with flip angle distribution of mean around  $60^\circ$ . For this simulation, we used  $90^\circ$  as the flip angle to reconstruct signals encoded with a model using  $\alpha_{Encode}$  flip angle (Plus some angle noise of with shape parameter  $\sigma = 10$ ). All the other parameters are the same as that in table 7.11.

### 7.3.2. Visual Inspection

By looking at the visuals, for both the solving algorithms, it is seen that as the flip angle, which we used in the reconstructing model, deviates away from the actual flip angle that was used during encoding, the image is degraded. In our case, using  $90^\circ$  to reconstruct a  $45^\circ$  flip angle could not bear result for IRhybrid\_Isqr (figure 7.23e). For IRhtv because the algorithm is inherently robust to noise, is able to reconstruct something although degraded.

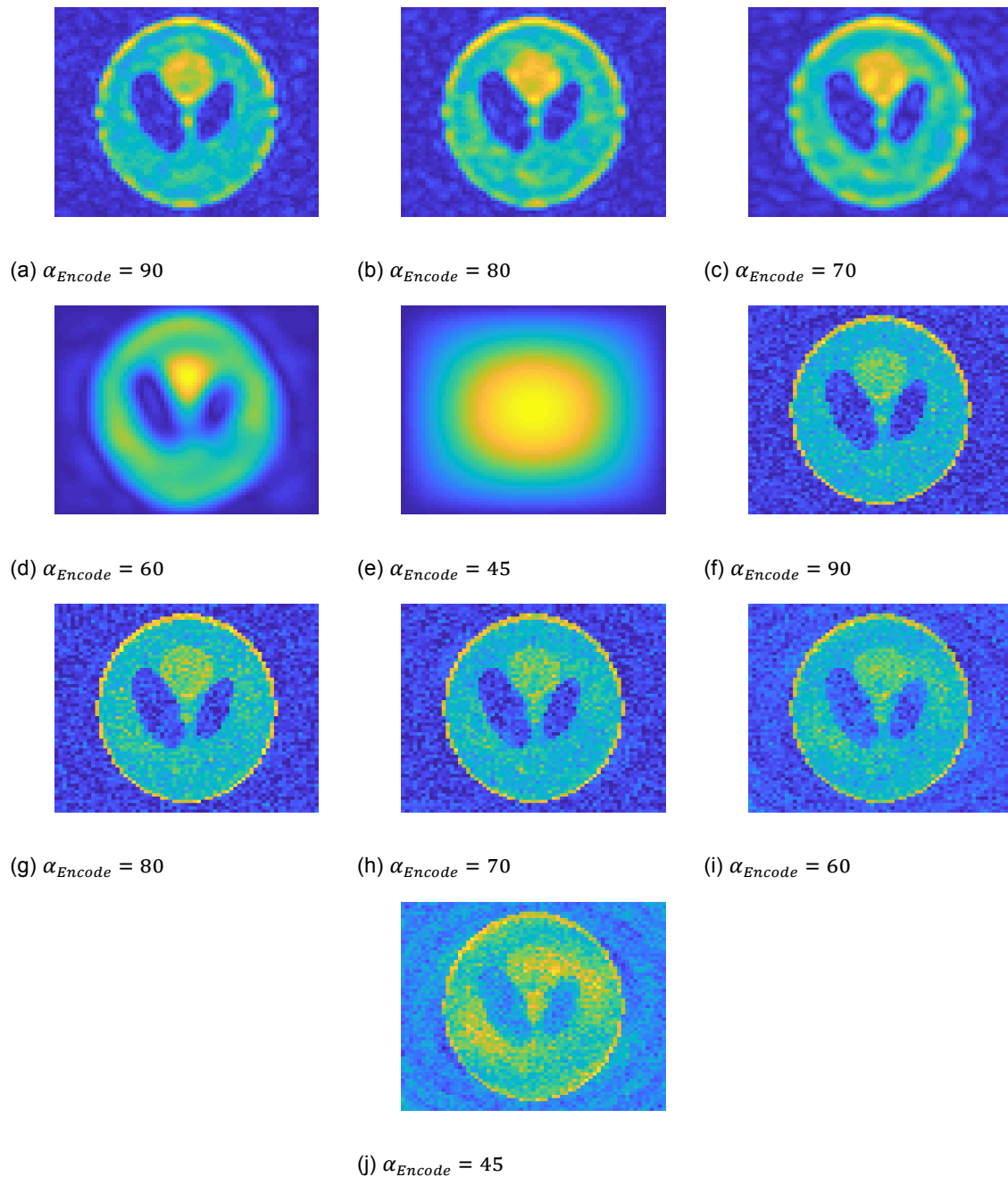
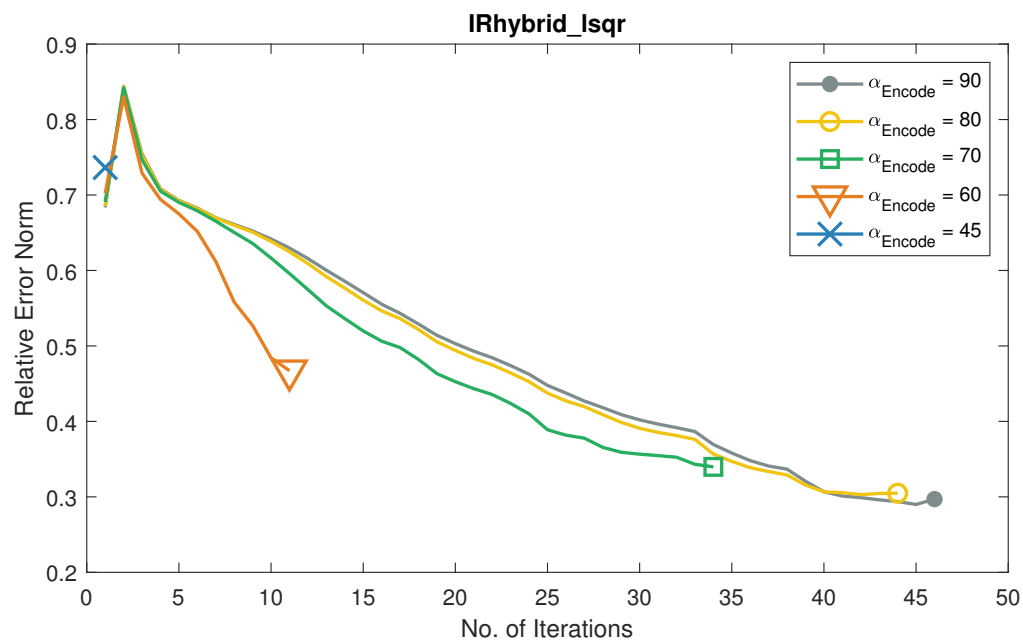


Figure 7.23: Investigation of wrong flip angle assumption using IRhybrid\_lsqr a)-e) and IRhtv f)-j)

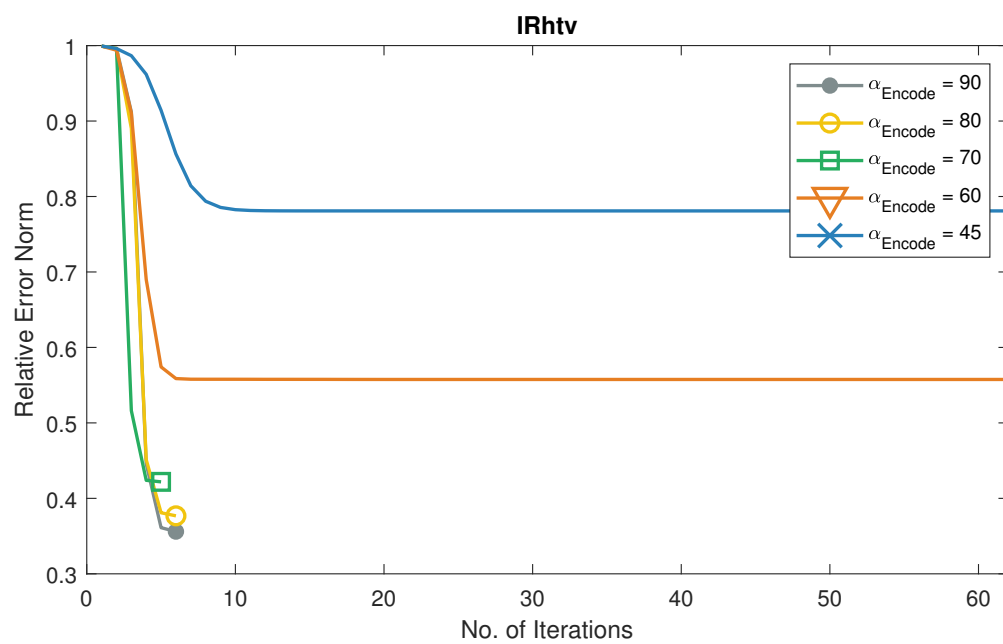
### 7.3.2. Relative Error Norm Versus Number of Iterations

The trend of error norm plot in figure 7.23 is in line with the visual inspection. Further, we remind ourselves that the signal model considered in this investigation assumes that the magnetizations are flipped about the  $\hat{\mathbf{i}}$  axis. If the magnetizations are flipped about the  $\hat{\mathbf{k}}$  axis, for example, the expression of equation 7.8 will be different, and we would obtain a different signal model. So unlike conventional MRI, the orientation along which the magnetizations are flipped plays a role. But luckily, although we cannot know the resulting flip angle of the magnetizations after the RF pulse has been applied, we can determine the axis about which the magnetizations are flipped (because this depends on the coil design). To encapsulate this investigation, we conclude that we have to consider both the nominal flip angle and the axis about which the magnetizations are flipped, into our signal model to get a superior

reconstruction.



(a)



(b)

Figure 7.24: Relative Error Norm for investigation of Investigation of wrong flip angle assumption using a) IRhybrid\_Isqr b) IRhtv

Table 7.13: Relative Error Norm for investigation wrong Flip Angle

Signal Model Parameter	IRhybrid_Isqr	IRhvtv
	Relative Error Norm	Relative Error Norm
$\alpha_{Encode} = 90$	0.2970	0.3560
$\alpha_{Encode} = 80$	0.3048	0.3768
$\alpha_{Encode} = 70$	0.3397	0.4219
$\alpha_{Encode} = 60$	0.4672	0.5575
$\alpha_{Encode} = 45$	0.7364	0.7809

## 7.4. Angle Combination Investigation

The inhomogeneities in the B0 field makes the field unsymmetrical. Therefore, rotating an unsymmetrical field will lead to different field maps being generated, which has its corresponding encoding matrix (figure 7.25). This unsymmetries help in reducing the non-bijective mappings between the field and locations, and help in reconstructing the image. Figure 7.26 illustrates the effects of using a symmetrical field. As can be seen, due to non-bijective mappings, we would end up reconstructing an image which is also symmetrical, although the original image is unsymmetrical.

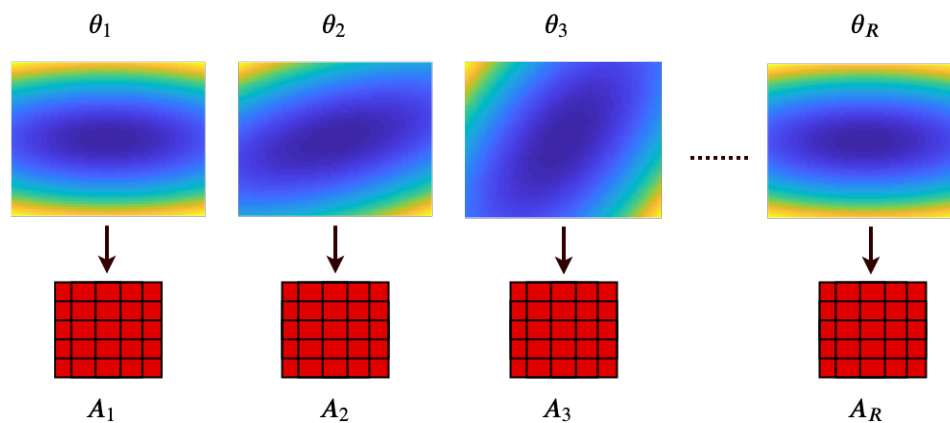
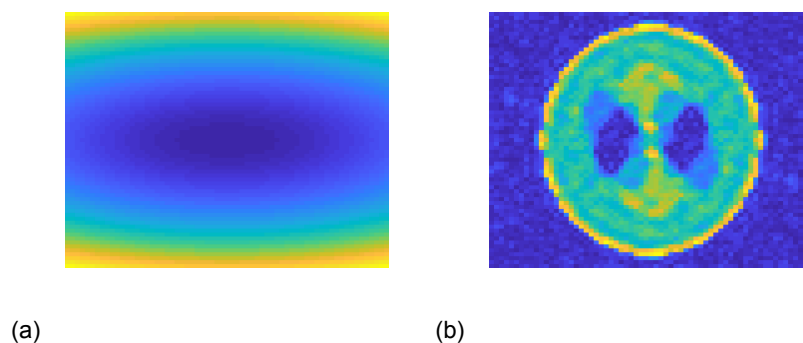
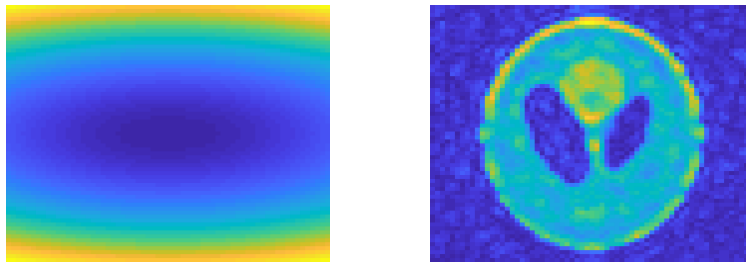


Figure 7.25: Corresponding encoding matrix of different orientations of B0 map





(c) (d)

Figure 7.26: Influence of field inhomogeneities in reconstruction in 10dB SNR. a) B0 profile after quadratic fitting the measured B0 field map. This field is perfectly symmetrical about the horizontal and vertical axis. b) Reconstructed image using field map in a). c) Measured B0 profile that has inhomogeneities in it (although it looks the same as a) there are inhomogeneities in this map and it is difficult to see it). d) Reconstructed image using field map in c.)

Now, a question arises that which and how many of these  $\theta_r, 2 < r < R$ , angles should we choose such that we get the best possible reconstruction. For our case, we will consider 72 angles:  $0^\circ, 5^\circ, 10^\circ, \dots, 355^\circ$  from where we want to choose 36 of these. How to do these? Although this problem was unable to be solved here, the approaches taken are documented as a reference for future work in this direction if any.

It seems like a natural assumption would be to choose  $n$  matrices,  $A_1, A_2, \dots, A_n$ , such that they convey different information about the image. That, in some sense, means that the encoding matrices are independent of each other (figure 7.27a).

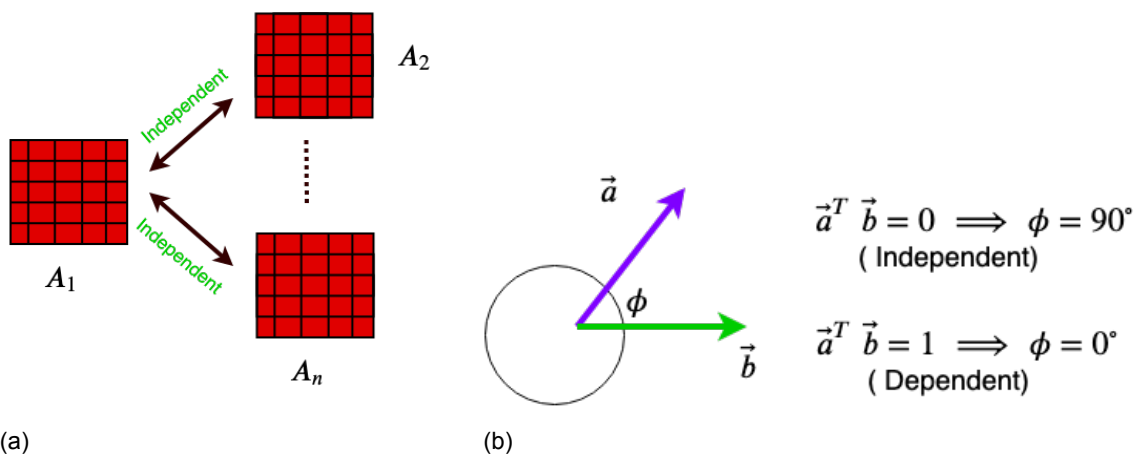
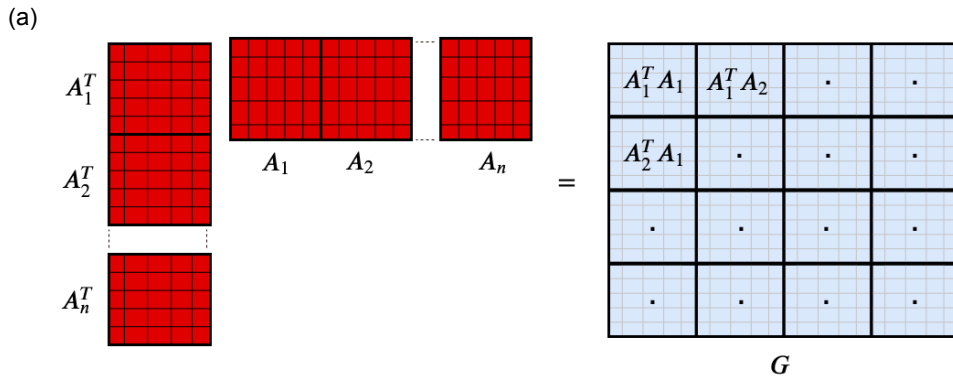
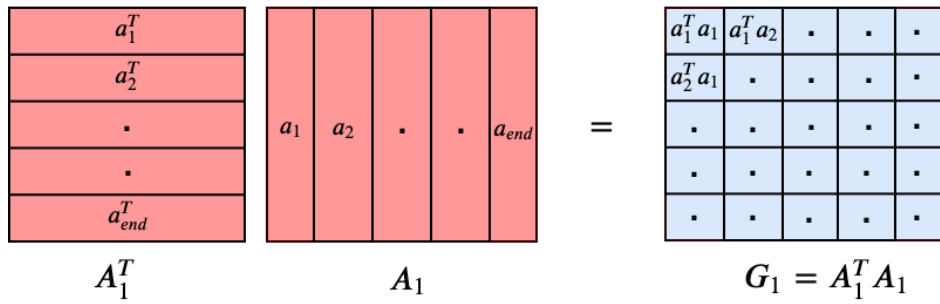


Figure 7.27: a) Assumption is that the encoding matrices are independent to each other in some sense such they encode different information. b) Angles between two normalized vectors.

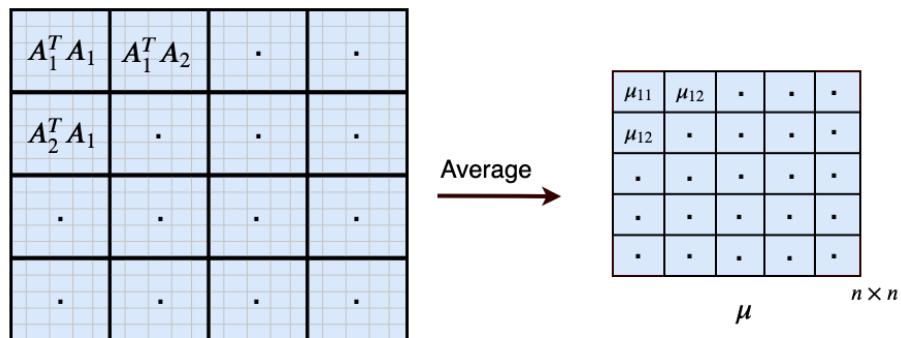
If we talk about two vector  $\vec{a}$  and  $\vec{b}$  (figure 7.27), they will be dependent if the angle,  $\phi$ , between them is  $0^\circ$ . If each column of a matrix is considered as a vector, the mutual angles between them is given by a normalized gram matrix (figure 7.28a) where each entry tells the angle between any two columns. Now, if we concatenate the encoding matrices horizontally and obtain the gram matrix, each sub-block, as shown in figure 7.28b, gives us the angles between the columns of one encoding matrix to another one.



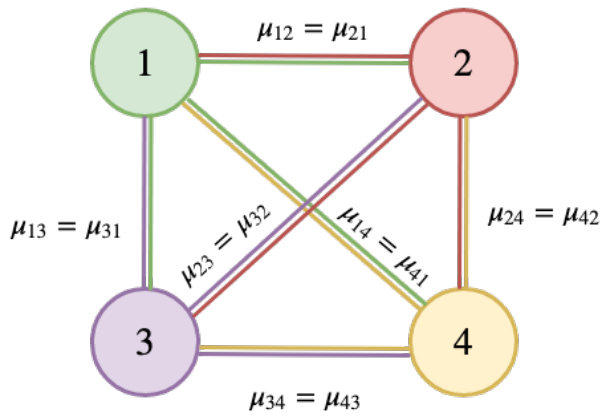
(b)

Figure 7.28: a) Gram matrix b) Computing gram matrix by concatenating the encoding matrices horizontally.

In practice, this gram matrix has a very large dimension. To reduce it, an average of all the entries of each sub-block was taken as shown in figure 7.29a. This was assumed to give a rough angle between the columns of any two matrices. Then we are left with a  $n \times n$  matrix,  $\mu$ , whose entries tell about the 'average angle' between any two matrices. Suppose, we have 4 angles and we want to select 3 angles from it such that the combination is the 'most independent'. This is denoted as a graph in figure 7.29b where each node denotes an encoding matrix corresponding to a rotated angle of the field map, and the edges denote the 'average angle' between the nodes. According to the logic, those three nodes will be selected whose  $\sum_{ij} \mu_{ij}$  is minimum, i.e. the angles between them are more. We have considered  $i$  and  $j$  to be the angle indices.



(a)

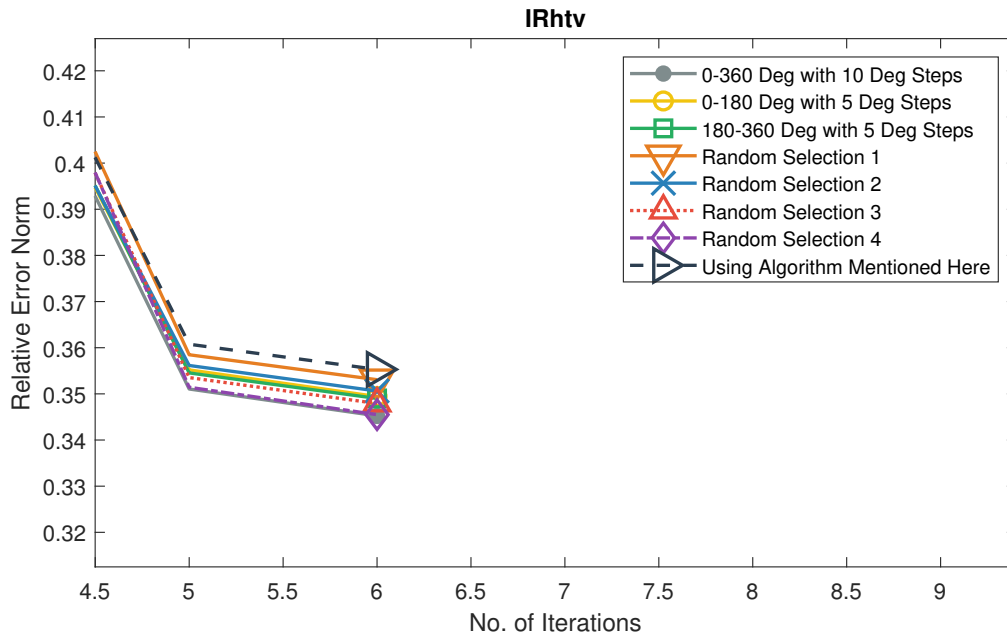


(b)

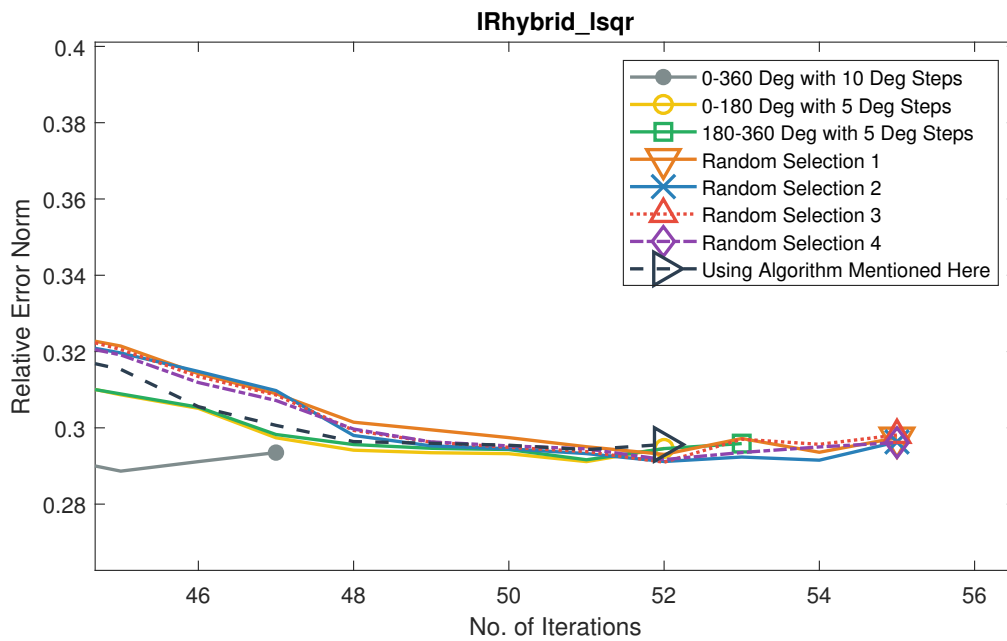
Figure 7.29: a) Gram matrix b) Computing gram matrix by concatenating the encoding matrices horizontally.

In our case, if we have 72 angles, and we want to select 36 out of it, we would have to try out  ${}^{72}C_{36}$  combinations to find the solution exhaustively. This is not feasible. Thus, the approach taken here was to randomly select 36 angles out of 72 angles in each iteration, and then compute  $\Sigma_{ij}\mu_{ij}$  for it. We run this step for millions of iterations, and in each step, we keep track of the minimum  $\Sigma\mu$ , and the angle combination corresponding to it. This combination, though not guaranteed to be optimal, should give us a good reconstruction. This was done and it was unsuccessful to bear a superior result compared to other angle combinations used in this examination (figure 7.30). The combinations of angles that were chosen here were such that they covered at least the smallest angle between any two axes of symmetries ( $90^\circ$  in our case) of the B0 field map<sup>2</sup> sufficiently. The 'Random Selection 1,2,3 and 4' graphs in the legend of figure 7.30 denote the combinations where 36 angles were randomly selected between  $0^\circ$  to  $360^\circ$ . Except the angle range and angle step size, all the parameters used for the simulations in this section are the same as that in table 7.4. Only the discrepancy principle as the parameter selection strategy, with exact noise estimate, is used here.

<sup>2</sup>In our case, the B0 map was roughly elliptical and thus could be considered as a symmetric figure.



(a)



(b)

Figure 7.30: Relative Error Norm for investigation of angle choices computed using a) IRhybrid\_Isqr b) IRhtv

The sequence of  $0^\circ - 360^\circ$  with  $10^\circ$  step size was performing better than the others. Further, the  $\Sigma\mu$  of this angle combination was found to be larger than that of the angle combination found by the algorithm suggested here. This suggested that this algorithm is not the right one to search for the best angle combination.

Under closer inspection, we can see that because we are vertically stacking the encoding matrices, good reconstruction did not only matter on how independent information each encoding matrix gave. Condition number of the resulting matrix also played a role, which tells how robust the matrix is against noise, and how fast the algorithm converges to some

solution (although we cannot say that this is the correct solution). For example, we consider the following-

We have three matrices-  $A_1$ ,  $A_2$  and  $A_3$  as given below-

$$A_1 = \begin{bmatrix} 1 & 5 & 8 \\ 7 & 3 & 4 \end{bmatrix}, \quad A_2 = \begin{bmatrix} 1 & 1 & 1 \\ 1 & 1 & 1 \end{bmatrix} \text{ and } A_3 = \begin{bmatrix} 3 & 3 & 3 \\ 3 & 3 & 3 \end{bmatrix}$$

We notice that all the columns of  $A_2$  and  $A_3$  are dependent. Now we aspire to vertically stack the best 2 matrices out of these 3 such that the condition number,  $\rho(A)$ , is the least to give us a faster convergence to the solution. The condition numbers computed are as follows when the following combinations are used-

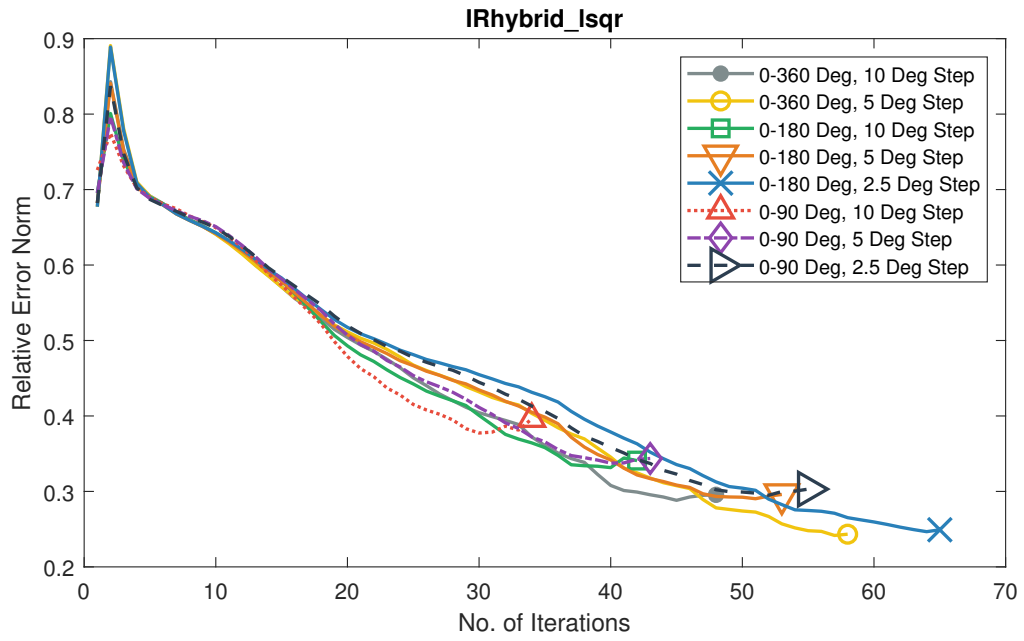
$$A = \begin{bmatrix} A_1 \\ A_2 \end{bmatrix} = \begin{bmatrix} 1 & 5 & 8 \\ 7 & 3 & 4 \\ 1 & 1 & 1 \\ 1 & 1 & 1 \end{bmatrix}; \quad \rho(A) = 33.0163$$

$$A = \begin{bmatrix} A_2 \\ A_3 \end{bmatrix} = \begin{bmatrix} 1 & 1 & 1 \\ 1 & 1 & 1 \\ 3 & 3 & 3 \\ 3 & 3 & 3 \end{bmatrix}; \quad \rho(A) = 5.5894 \times 10^{31}$$

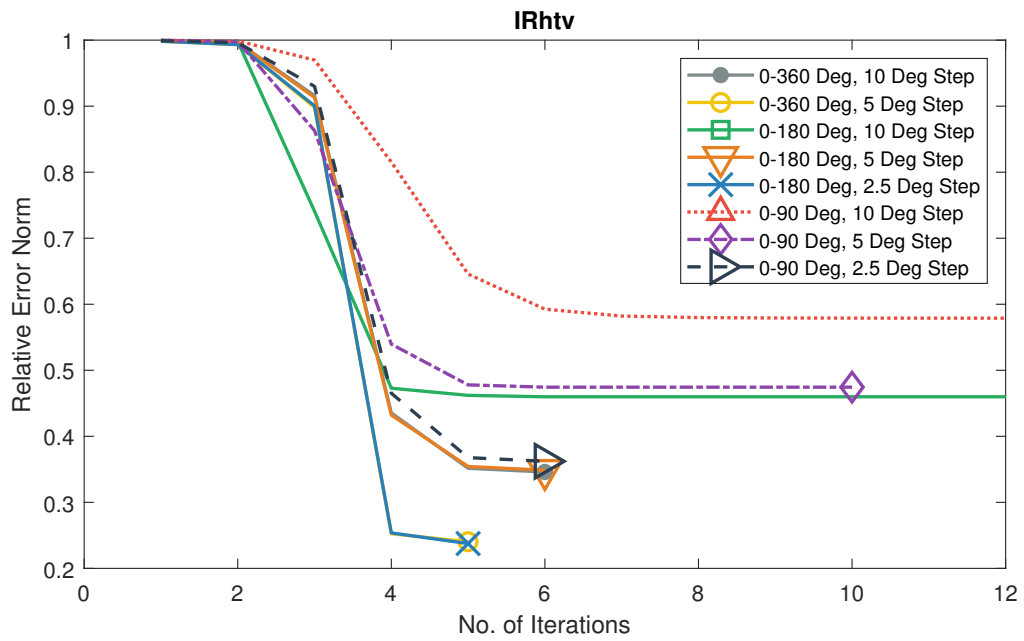
$$A = \begin{bmatrix} A_1 \\ A_3 \end{bmatrix} = \begin{bmatrix} 1 & 5 & 8 \\ 7 & 3 & 4 \\ 3 & 3 & 3 \\ 3 & 3 & 3 \end{bmatrix}; \quad \rho(A) = 14.8138$$

So one would go for the third combination in this case. But the algorithm suggested here would fail in this case because there would be no difference in angle between  $A_1$  and  $A_2$ , and  $A_1$  and  $A_3$ . Plus, the condition number of vertically stacked encoding matrix does not depend on how independent the columns of each encoding matrices are. Thus, if one wishes to find the optimal angles, it is sensible to take into account how these encoding matrices behave as a whole when they are stacked together rather than only looking at their individual properties.

To summarize this section, for a fixed number of angles, it was seen that the chosen combination of angle sequences (as shown in figure 7.30) did not provide any stark differences in performance as long as they covered at least the smallest angle between any two axes of symmetries of the B0 field map sufficiently. This can also be seen in figure 7.31. From the legends, the 1<sup>st</sup>, 4<sup>th</sup> and 8<sup>th</sup> graph considers a total of 36 angles, and they all perform similarly. The 2<sup>nd</sup> and 5<sup>th</sup> graph considers 72 angles, and they also perform similarly. And so does the 3<sup>rd</sup> and 7<sup>th</sup> graph which consider 18 angles. The 6<sup>th</sup> graph considers the lowest number of angles and perform the worst out of all. More number of angles improves the image quality. But however they make the system matrix large as we have to stack more encoding matrices.

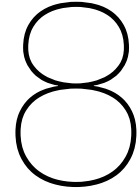


(a)



(b)

Figure 7.31: Relative Error Norm for investigation of the number of angle choicen computed using a) IRhybrid\_Isqr b) IRhtv



# Conclusions and Future Work

## 8.1. Conclusion

In part 1 of this report, we have seen the motivation of constructing a portable low-field MRI machine. Such devices would provide major benefits as it will cut down the cost of expensive conventional MRI scanners. This would make it more accessible to a larger part of the population. This thesis studied the signal processing aspects of a rotating MRI machine that works in a low inhomogeneous magnetic field setting. Background theory was provided, and the signal model for the aforementioned machine was derived.

Part 2 focused on listing the employed algorithms that are available in the IRTools package. But before introducing them, an adequate mathematical background on Krylov Subspace methods was given. Two automated regularization parameter searching strategies-Discrepancy principle and GCV, were discussed. IRhybrid\_lsqr and IRhtv were described, which are solvers based on 2-norm and 1-norm regularization, respectively.

In Part 3, we inspected various parameters of the signal model and the reconstruction algorithms that influenced the image quality. It was seen that the resolution of the image increased by including more time samples. For a fixed acquisition time, it was found to be beneficial to have a small DW to avoid aliasing effects. But the downside of having a small DW while keeping the acquisition time fixed is that it increases the TD, which in turn made the system matrix larger. An increase in the system matrix dimension increases the computation time and creates memory issues on the computer. Next, the automatic parameter selection strategies, namely the discrepancy principle and GCV were examined. We have to supply a noise estimate to the solvers employing the discrepancy principle. If the supplied noise estimate is around the correct estimate, the quality of the predicted regularization parameter is enhanced. In contrast, the algorithms employing GCV requires no noise level input. However, if the dimension of the system matrix is large, their performance is slow as they have to compute the matrix's SVD. Now regarding the solving algorithms, IRhtv was found to be more robust than IRhybrid\_lsqr in computing solutions under noisy conditions. Moreover, it was seen that the former algorithm was considerably fast in converging than the latter one. Moving on, the angle dependencies between the signal model and the rotating field was studied. Here, the main conclusion was that we should account for both the flipped angle and the axis about which the magnetizations are flipped in our signal model. Better determination of these parameters leads to a superior result. The last investigation of the thesis was regarding the choice of the rotation angles of the MRI machine. It was seen that for a fixed number of angles, such that they sufficiently covered at least the smallest angle between any two axes of symmetries of the B0 field map, the reconstruction algorithms performed similarly.

## 8.2. Future Work

### 8.2.1. K-space and Spatial Domain Link

As mentioned in section 4.8 and section 7.1, the non-linearities in the B0 profile was ignored to make the analysis easier. When we have a linear B0 profile, each point in the k-space is mapped to all the points in the FOV of the spatial domain, where all the points in the latter are given equal weights. The other way round is also true, that is, each point in the FOV of the spatial domain is mapped to all the points in the k-space, where all the points in the k-space are given equal weights. Now, when the B0 profile is not linear, the aforementioned weights are not constant throughout the points. It will, in fact, vary locally in the domain. [18] talks about local k-space, in contrast to the standard k-space, where each of the pixel positions in the spatial domain has its own local distribution of encoded k-space frequencies. The local k-space frequencies characterize the spatial information that is available about the measured object, at each location. It is believed that investigating this relationship between the k-space and spatial domain, in the case of non-linear gradients, may reveal more information about the sampling of the MRI signal, and as well as about the design considerations of the inhomogeneous B0 map. This will help us get more reliable approaches to choose TD and DW.

### 8.2.2. Receive Field Profile Investigation

The investigations which are done here assume that the receive field profiles are homogenous throughout the bore of the MRI machine. In the future, the measured receive field map can be used in the investigation to study the signal model. Moreover, we can also inspect the case when we use more than one receiver, as was done in [5]. If the field maps of the receivers are different, it provides additional spatial encoding that can be used to disambiguate the non-bijective field mappings.

### 8.2.3. Optimal Angle Combination Selection

In section 7.4, it was felt that it is sensible to take into account how the encoding matrices behaved as a whole when they were stacked together, rather than only looking at them individually. Although the author believes that investigating this will not be as helpful as the other future work mentioned here, a brief incomplete idea in this direction is presented here.

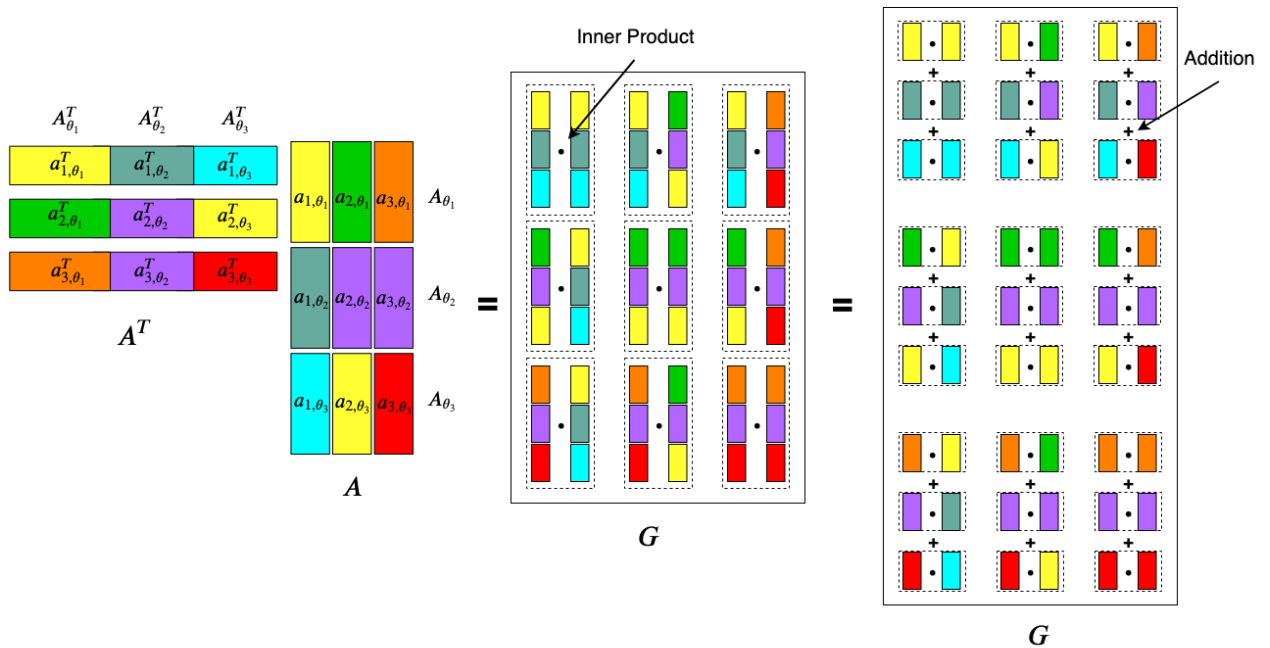


Figure 8.1: Elements of the gram matrix of the stacked encoding matrices can be expressed as sum of smaller inner product

In figure 8.1, we can see that the elements of the gram matrix can be expressed as the inner product (the middle figure) of the columns of the stacked encoding matrices,  $\mathbf{A}$ . These inner products can further be broken down into additions of individual inner products (the rightmost diagram). The involvement of these inner products in the computation of the gram matrix elements depends upon the corresponding encoding matrices. For example, if we do not use the  $\mathbf{A}_{\theta_2}$ , the middle row of inner products will not be involved in the computation of the gram matrix elements (figure 8.2).

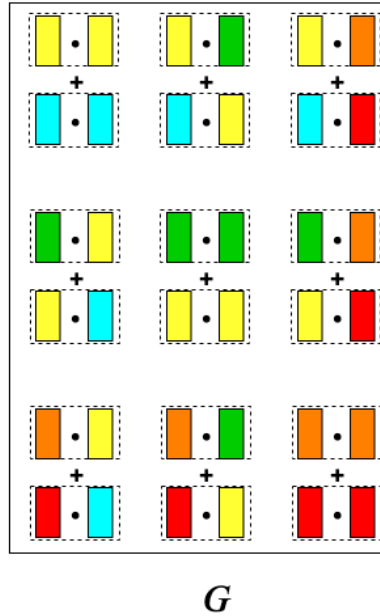


Figure 8.2: Gram matrix of the stacked matrices when  $\mathbf{A}_{\theta_2}$  is not used.

This influence can be investigated further to see if the elements of the gram matrix can be manipulated in an intended manner. Provided that we know this influence, if we can optimize the condition number of the gram matrix, it will lead us indirectly to the desired angle combination (a related material in this direction is given in [2]).

#### 8.2.4. Experimental Work

Perhaps the most important future work that has to be done is to carry out the experimental analysis of the algorithms mentioned here. The drawback of the simulations done here is that we assumed a lot of parameters, for example, the knowledge of flip angle distribution used, the axis about which the magnetization was flipped, and so on. Moreover, the investigations were done provided that we knew the rotated orientation of the B0 map exactly with respect to the measured signal. To elaborate it, we assumed that we knew that the measured signal was  $\mathbf{b}_{\theta_1}$  when the B0 was rotated by  $\theta_1$  (with some reference axis), and not when the field was rotated by  $\theta_2$ . In principle, this should not matter as this would only rotate the obtained image by a certain angle. But with all the interpolations of the B0 map involved, this cannot be guaranteed as it depended on the system matrix properties. This was actually tried out in simulations. The signal was encoded using an angle sequence of  $0^\circ - 360^\circ$  with  $10^\circ$  step size, using the B0 field shown in figure 7.1. While decoding, the starting reference of the former angle sequence was changed from  $0^\circ$  to  $10^\circ$  such that we had the angle sequence  $10^\circ, 20^\circ, \dots, 350^\circ, 0^\circ$ . The solving algorithms gave a very degraded image in this case. This implied that we should keep track of the orientation of the field map with respect to the measured signal. To sum up, there are a lot of practical issues left to be explored which can only be discovered through actual implementations of the algorithms in the rotating MRI machine.



# Bibliography

- [1] Peter Blümler and Federico Casanova. Hardware developments: Halbach magnet arrays. *Mobile NMR and MRI: Developments and Applications*, 133, 2015.
- [2] Xiaojun Chen, Robert S Womersley, and Jane J Ye. Minimizing the condition number of a gram matrix. *SIAM Journal on optimization*, 21(1):127–148, 2011.
- [3] Julianne Chung, James G Nagy, and DIANNE P O’Leary. A weighted gcv method for lanczos hybrid regularization. *Electronic Transactions on Numerical Analysis*, 28(Electronic Transactions on Numerical Analysis), 2008.
- [4] Julianne Chung, James G Nagy, and DIANNE P O’Leary. A weighted gcv method for lanczos hybrid regularization. *Electronic Transactions on Numerical Analysis*, 28(Electronic Transactions on Numerical Analysis), 2008.
- [5] Clarissa Zimmerman Cooley, Jason P Stockmann, Brandon D Armstrong, Mathieu Saracanie, Michael H Lev, Matthew S Rosen, and Lawrence L Wald. Two-dimensional imaging in a lightweight portable mri scanner without gradient coils. *Magnetic resonance in medicine*, 73(2):872–883, 2015.
- [6] Gigi Galiana, Jason P Stockmann, Leo Tam, Dana Peters, Hemant Tagare, and R Todd Constable. The role of nonlinear gradients in parallel imaging: A k-space based analysis. *Concepts in Magnetic Resonance Part A*, 40(5):253–267, 2012.
- [7] Silvia Gazzola and Paolo Novati. Automatic parameter setting for arnoldi–tikhonov methods. *Journal of Computational and Applied Mathematics*, 256:180–195, 2014.
- [8] Silvia Gazzola, James Nagy, and Paolo Novati. Arnoldi-tikhonov methods for sparse reconstruction. In *Householder Symposium XIX June 8-13, Spa Belgium*, page 82, 2014.
- [9] Silvia Gazzola, Per Christian Hansen, and James G Nagy. Ir tools: a matlab package of iterative regularization methods and large-scale test problems. *Numerical Algorithms*, 81(3):773–811, 2019.
- [10] Gene H. Golub and Charles F. Van Loan. *Matrix Computations*. The Johns Hopkins University Press, third edition, 1996.
- [11] Per Christian Hansen. *Discrete inverse problems: insight and algorithms*, volume 7. Siam, 2010.
- [12] David I Hoult and RE Richards. The signal-to-noise ratio of the nuclear magnetic resonance experiment. *Journal of Magnetic Resonance (1969)*, 24(1):71–85, 1976.
- [13] DI Hoult. The principle of reciprocity in signal strength calculations—a mathematical guide. *Concepts in Magnetic Resonance: An Educational Journal*, 12(4):173–187, 2000.
- [14] Zhi-Pei Liang and Paul C Lauterbur. *Principles of magnetic resonance imaging: a signal processing perspective*. SPIE Optical Engineering Press, 2000.
- [15] J Mallinson. One-sided fluxes—a magnetic curiosity? *IEEE Transactions on magnetics*, 9(4):678–682, 1973.
- [16] Karla Miller. Mri image formation. *Powerpoint presentation, FMRIB Physics Group*.
- [17] T O’Reilly, WM Teeuwisse, and AG Webb. Three-dimensional mri in a homogenous 27 cm diameter bore halbach array magnet. *Journal of Magnetic Resonance*, page 106578, 2019.

- 
- [18] Gerrit Schultz. *Magnetic resonance imaging with nonlinear gradient fields: signal encoding and image reconstruction*. Springer Science & Business Media, 2013.
- [19] Jonathan Richard Shewchuk et al. An introduction to the conjugate gradient method without the agonizing pain, 1994.
- [20] Jonathan Richard Shewchuk et al. An introduction to the conjugate gradient method without the agonizing pain, 1994.
- [21] Hazel A Shute, John C Mallinson, David T Wilton, and Desmond J Mapps. One-sided fluxes in planar, cylindrical, and spherical magnetized structures. *IEEE Transactions on Magnetics*, 36(2):440–451, 2000.
- [22] Thomas Strohmer and Roman Vershynin. A randomized kaczmarz algorithm with exponential convergence. *Journal of Fourier Analysis and Applications*, 15(2):262, 2009.
- [23] J Tenne and SW Armfield. A note on the relation of gaussian elimination to the conjugate directions algorithm. *ANZIAM Journal*, 46:971–986, 2004.
- [24] C. Vuik and D.J.P. Lahaye. Scientific computing. *Lecture notes for the course Scientific Computing, TU Delft*, 2015.